NASA Contractor Report 172601

Data Analysis for Lidar and Quartz Crystal Microbalance Systems

Geoffrey S. Kent and Adarsh Deepak

Institute for Atmospheric Optics and Remote Sensing
Hampton, VA 23666

Contract NAS1-16253

June 1985

National Aeronautics and Space Administration

Langley Research Center
Hampton, Virginia 23665

FOREWORD

The Institute for Atmospheric Optics and Remote Sensing (IFAORS) is pleased to submit the final report on tasks a through d of NASA Contract NAS1-16253. We have pleasure in acknowledging the assistance of M. P. McCormick and L. R. McMaster of NASA, Langley Research Center, who provided many useful discussions on the various aspects of this work.

ABSTRACT

This report presents results of the analysis of data taken on the stratospheric aerosol, using lidar, Quartz Crystal Microbalance (QCM), and the SAGE and SAM II satellite systems. The main objective of the work reported has been to use the data, taken with the NASA-LaRC instruments, to study the stratospheric effects of volcanic eruptions during the period between the launch of the SAGE and SAM II satellite systems and October 1980. Four significant volcanic eruptions, for which data are available, occurred during this period--Soufriére, Sierra Negra, St. Helens, and Ulawun. Data on these have been analyzed to determine the changes in stratospheric mass loading produced by the eruptions, and to study the dispersion of the newly injected material.

The main conclusions drawn from the study are:

1. Data, obtained by using more than one of the listed sensor systems to study the atmospheric aerosol, enables a composite picture of the aerosol to be constructed, that is not possible using data from a single sensor alone.

2. Quantitative use of the QCM data, obtained after recent volcanic eruptions, has to await the completion of ongoing calibration studies.

3. The prevolcanic, background, stratospheric aerosol mass in 1979 was approximately 5×10^5 metric tons.

4. There is a tendency for both the nonvolcanic and volcanic aerosol to divide itself into three zones between latitudes 90° S to 25° S, 25° S to 25° N, and 25° N to 90° N, with altitude and concentration changes occurring near the boundaries of these zones.

5. The most significant stratospheric effect produced by any of the eruptions studied was for St. Helens, which injected approximately 3×10^5 metric tons of aerosol.

6. Stratospheric aerosol mass loading, after an eruption, rises to a maximum after an interval of 3 to 4 months, followed by a rather slower decline.

7. Dispersion of injected material occurs immediately after an eruption, meridional movement taking place approximately along isentropic flow lines. In the case of an equatorial eruption, global dispersion may occur in a period of about 6 months.

TABLE OF CONTENTS

	Page
FOREWORD	i
ABSTRACT	iii
LIST OF FIGURES	vii
LIST OF TABLES	xiii
1. INTRODUCTION	1
2. BACKGROUND	3
2.1 Techniques for Studying the Stratospheric Aerosol	3
2.2 The Nature and Behavior of the Stratospheric Aerosol	5
2.3 Volcanic Eruptions During the Period of Study	8
3. DATA SETS AVAILABLE FOR STUDY	11
3.1 SAGE and SAM II	11
3.2 Lidar	16
3.3 Quartz Crystal Microbalance	16
4. GLOBAL STRATOSPHERIC AEROSOL CONCENTRATIONS, FEBRUARY 1979 - DECEMBER 1980	19
4.1 Conversion of Satellite and Lidar Data to Mass Loading	19
4.2 Stratospheric Aerosol Mass Loading	22
5. STRATOSPHERIC EFFECTS OF THE ERUPTION OF SOUFRIÉRE	35
5.1 Introduction	35
5.2 Lidar Observations	35
5.3 SAGE Observations	35
5.4 Interpretation of the Observations on Dispersion	41
5.5 Mass Loading	49
6. STRATOSPHERIC EFFECTS OF THE ERUPTION OF SIERRA NEGRA	53
6.1 Introduction	53
6.2 SAGE Observations	53
6.3 Interpretation and Discussion of Observed Dispersion	59
6.4 Mass Loading Changes	64

TABLE OF CONTENTS - CONCLUDED

		Page
7.	STRATOSPHERIC EFFECTS OF THE ERUPTION OF ST. HELENS.	69
	7.1 Introduction.	69
	7.2 SAGE Observations	70
	7.3 Lidar Observations.	76
	7.4 Dispersion of the New Stratospheric Material	81
	7.5 Mass Loading and Meridional Movement.	85
8.	QUARTZ CRYSTAL MICROBALANCE DATA	89
9.	SUMMARY AND CONCLUSIONS.	93
10.	ACKNOWLEDGEMENTS	97
11.	REFERENCES	99
APPENDIX 1:	REGIONAL AND OPTICAL PROPERTIES OF STRATOSPHERIC AEROSOLS BASED ON MEASUREMENTS BY QUARTZ CRYSTAL MICROBALANCE CASCADE IMPACTOR by A. Zardecki.	103
APPENDIX 2:	CONTOUR PLOTS FOR INDIVIDUAL SAGE POLE-TO-POLE MOVEMENTS FOR THE PERIOD FEBRUARY 21, 1979 - DECEMBER 13, 1980	123

LIST OF FIGURES

		Page
2.1	Latitude distribution of the concentration of stratospheric aerosols (from Rosen et al., 1975). Numbers on the diagram give the number of aerosol particles per mg of air	6
4.1	Conversion factor for extinction/aerosol mass as a function of dustsonde channel ratio for the inner stratosphere (models were taken from Russell, 1981). Also shown is a value calculated using the numerical data obtained by Hofmann and Rosen (1981)	21
4.2	The ratio (backscattering function at 0.69 μm)/(extinction cross-section at 1.00 μm) plotted as a function of particle radius..	23
4.3	Contour map for aerosol extinction for the period March 22 - April 28, 1979. Units used are 10^{-4} km^{-1}	25
4.4	Contour map for aerosol/molecular extinction ratio for the period March 22 - April 28, 1979	26
4.5	Contour plot showing the probability distribution for the height of the aerosol/molecular extinction ratio maximum at different latitudes. The data in the plot are for the period March 1 - May 31, 1979	27
4.6	Contour plot showing the probability distribution for the altitude difference between the peak aerosol/molecular extinction ratio and the tropopause. Data in this plot are for the period March 1 - May 31, 1979	28
4.7	Latitude variation of the mean stratospheric optical depth (measured from two kilometers above the tropopause) for the period March 22 - April 28, 1979	30
4.8	Mean hemisphere optical depth, as determined by the SAGE satellite between February 1979 and November 1980	31
5.1	Map showing the location of the Soufriére Volcano	36
5.2	Airborne lidar flight path on April 17-18, 1979. Figures shown alongside the flight path are the heights in kilometers of the stratospheric layers observed on the flight. . .	38
5.3	Examples of lidar profiles observed in the vicinity of the Soufriére volcano	39

LIST OF FIGURES, Cont'd

		Page
5.4	SAGE measurements shortly after the April 1979 eruptions of Soufriére	40
	(a) Normal aerosol extinction profile as determined by SAGE satellite system	40
	(b) Enhanced aerosol profile observed on April 24, 1979	40
	(c) Locations of enhanced aerosol extinction (50 percent or more above normal) are marked by crosses. Altitude of each layer peak is shown in km. Latitudes for each day of SAGE measurements are shown by dashed lines	40
5.5	Variation in height of the volcanic plume as it moved northward over the Atlantic Ocean and of the corresponding tropopause for those locations	42
5.6	SAGE and lidar measurements of Soufriére plumes	43
	(a) Map showing areas and altitudes of enhanced extinction (50 percent or more above normal) as observed by SAGE between April 21 and 28, 1979	43
	(b) Airborne lidar observations in the vicinity of St. Vincent, April 18 and 19, 1979. Also shown are the calculated air movements at three pressure levels during the interval between the eruption at 2057 GMT on April 17, 1979, and the time of the flight	43
5.7	(a) Calculated wind trajectory at 50-mbar pressure level (20.7 km) for the period April 19 to 22, 1979. Starting point for trajectory is based on lidar data of April 18	48
	(b) High-altitude pressure map at 70-mbar level at 1200 GMT on April 26, 1979: Crosshatched area shows position of stratospheric plume on this day; dashed line indicates trajectory of plume on preceeding and following days	48
6.1	Examples of SAGE extinction profiles obtained at the time of the Sierra Negra eruption	54

Page

6.2 Maps showing the stratospheric optical depth, measured from two kilometers above the tropopause, as obtained by SAGE 56

(a) September 15 - October 21, 1979 56

(b) November 22 - December 30, 1979 56

6.3 Zonal mean extinction obtained by SAGE 57

(a) September 15 - October 21, 1979 57

(b) November 22 - December 30, 1979 57

Dashed lines show the mean latitude for each day's observations. The solid line at the base of the plotted extinction values shows a height two kilometers above the tropopause.

Code for shading:

SHADING	MEAN EXTINCTION
	$0\text{-}1 \times 10^{-4} KM^{-1}$
	$1\text{-}2 \times 10^{-4} KM^{-1}$
	$2\text{-}4 \times 10^{-4} KM^{-1}$
	$4\text{-}6 \times 10^{-4} KM^{-1}$
	$6\text{-}8 \times 10^{-4} KM^{-1}$
	$> 8 \times 10^{-4} KM^{-1}$

6.4 Zonal mean extinction obtained by SAGE 58

(a) January 27 - March 6, 1980 58

(b) May 12 - June 20, 1980 (Eastern hemisphere only) 58

Dashed lines show the mean latitude for each day's observations. The solid line at the base of the plotted extinction values shows a height two kilometers above the tropopause.

Code for shading:

SHADING	MEAN EXTINCTION
	$0\text{-}1 \times 10^{-4} KM^{-1}$
	$1\text{-}2 \times 10^{-4} KM^{-1}$
	$2\text{-}4 \times 10^{-4} KM^{-1}$
	$4\text{-}6 \times 10^{-4} KM^{-1}$
	$6\text{-}8 \times 10^{-4} KM^{-1}$
	$> 8 \times 10^{-4} KM^{-1}$

6.5 Contour plots of stratospheric extinction ratios before and after the eruption of Sierra Negra. The variation of the extinction ratio is shown as a function of altitude and time for four different northern hemisphere latitude belts 60

Page

6.6 (a) Potential temperature as a function of altitude and latitude for December 1979. Also shown in the figure are the position of the tropopause and the new stratospheric volcanic layer produced by Sierra Negra 62

(b) Figure showing the manner in which the extent and position of the volcanic layer is defined 62

6.7 Potential temperature as a function of altitude and latitude for February, 1980. Also shown in the figure are the position of the tropopause and the new stratospheric volcanic layer produced by Sierra Negra 63

6.8 (a) Mean stratospheric optical depth (from two kilometers above the tropopause), for three latitude zones, between February 1979 and June 1980 65

(b) Mean stratospheric optical depth increase produced by the eruption of Sierra Negra for the same latitude zones as shown in Figure 6.8(a). A scale showing the equivalent mass loading is drawn on the right hand ordinate 65

6.9 (a) Time variation of the total stratospheric mass loading increase produced by the eruption of Sierra Negra 67

(b) The ratio (aerosol loading increase poleward of 20^{o}S and 20^{o}N)/(aerosol loading increase between 20^{o}S and 20^{o}N) plotted as a function of time between November 1979 and June 1980 67

7.1 Stratospheric aerosol extinction profiles obtained by SAGE at a wavelength of 1 μm 71

(a) Normal profile unaffected by volcanic effluents 71

(b) Profile showing an enhancement caused by Mt. St. Helens of about a factor of 10 near the layer peak 71

7.2 Map showing the stratospheric optical depth, measured from two kilometers above the tropopause, as obtained by SAGE for the period May 12 - June 20, 1980 72

Page

7.3 Zonal mean extinction obtained by SAGE for the period May 12 - June 20, 1980 73

Dashed lines show the mean latitude for each day's observations. The solid line at the base of the plotted extinction values shows a height two kilometers above the tropopause.

Code for shading:

SHADING	MEAN EXTINCTION
	$0-1 \times 10^{-4} KM^{-1}$
	$1-2 \times 10^{-4} KM^{-1}$
	$2-4 \times 10^{-4} KM^{-1}$
	$4-6 \times 10^{-4} KM^{-1}$
	$6-8 \times 10^{-4} KM^{-1}$
	$> 8 \times 10^{-4} KM^{-1}$

7.4 Map showing the stratospheric optical depth, measured from two kilometers above the tropopause, as obtained by SAGE for the period July 21 - August 26, 1980 74

7.5 Zonal mean extinction obtained by SAGE for the period July 21 - August 26, 1980 75

Dashed lines show the mean latitude for each day's observations. The solid line at the base of the plotted extinction values shows a height two kilometers above the tropopause.

Code for shading:

SHADING	MEAN EXTINCTION
	$0-1 \times 10^{-4} KM^{-1}$
	$1-2 \times 10^{-4} KM^{-1}$
	$2-4 \times 10^{-4} KM^{-1}$
	$4-6 \times 10^{-4} KM^{-1}$
	$6-8 \times 10^{-4} KM^{-1}$
	$> 8 \times 10^{-4} KM^{-1}$

7.6 Lidar profiles obtained at NASA-Langley, Hampton, Virginia, before and after the eruption of Mt. St. Helens 77

7.7 Lidar profiles obtained at NASA-Langley, Hampton, Virginia, between July 1980 and June 1981 78

7.8 Flight path for the airborne lidar system in December, 1980 79

Page

7.9 Two-color airborne lidar profiles taken in December 1980 during the flight to Frobisher Bay 80

(a) Taken near Plattsburgh, New York State 80

(b) Taken near Frobisher Bay 80

7.10 Mean zonal wind velocity in summer plotted as a function of height and latitude (Newell et al., 1972) 82

7.11 Times of arrival of aerosol layers between 12 km and 16 km as observed by various lidar stations around the globe. The dashed lines show the expected air movements at the latitudes and heights involved (Newell et al., 1972) 83

7.12 Times of arrival of aerosol layers above 20 km as observed by various lidar stations around the globe. * Layer at 20 to 22 km. ● Layer at 20 to 24 km. The cross-hatched area represents the average expected range of stratospheric air movements. Also shown are the dates, latitudes and longitudes of SAGE observations 84

7.13 Variation of stratospheric optical depth and equatorial mass loading in the equatorial sector ($20^{o}S$ - $20^{o}N$) during the period April - October 1980 86

8.1 Aerosol particle size distributions obtained by the Quartz Crystal Microbalance over Greenland in November 1978 and by wire impactor over Alaska in July 1979 (Farlow et al., 1981) 90

LIST OF TABLES

Table No.		Page
2.1	Techniques for Studying the Stratospheric Aerosol.	4
2.2	Recent Volcanic Eruptions Affecting the Stratosphere	9
3.1	SAGE Global Movements.	12-15
3.2	Langley Research Center Airborne Lidar Flights Between April 1979 and June 1981	17
4.1	Stratospheric Aerosol Mass Loading Changes, 1979 - 1980. . .	33
5.1	Dates and Times of Major Eruptions of Soufrière Volcano. . .	37
5.2	Caribbean Mean Wind Velocities (April 15 to 24).	46
5.3	Parameters of Stratospheric Cloud Over West Africa	46
5.4	Atmospheric Extinction and Stratospheric Mass Loading from Soufrière, St. Vincent.	50
8.1	Comparison of QCM and Other Data	91
9.1	Stratospheric Aerosol Mass Loading Changes - Summary	94
9.2	Comparison of the Stratospheric Effects Produced by the Eruptions of Soufrière, Sierra Negra, St. Helens and Ulawun	95

1. INTRODUCTION

The most important reason for the continued study of stratospheric aerosols is their potential impact on global climate. The primary aerosol parameters that need to be measured for this purpose are their concentration, size distribution, shape, composition and refractive index. All these characteristics show regional, global and temporal variations, creating the need for a global aerosol data base. A significant part of this information is in the process of being supplied by five NASA sensor systems--ground-based and airborne lidar; quartz crystal microbalance (QCM) cascade impactor; stratospheric aerosol measurements II (SAM II); and stratospheric aerosol and gas experiment (SAGE).

These three sensor types complement one another extremely well, each providing information about a separate aspect of the overall stratospheric aerosol problem. Lidar measures aerosol backscatter with good spatial and temporal resolution. Ground-based systems have been used to provide detailed time histories of the variations in aerosol content over a single point on the ground. An airborne system has the additional advantage that it may be moved rapidly to a point of interest, e.g., a volcanic eruption, or even used to explore a given region of the stratosphere. Use of multiwavelength systems provides some information about aerosol size distributions. The SAGE and SAM II satellites measure aerosol extinction at 0.45 μm (SAGE) and 0.45 μm and 1.0 μm (SAGE and SAM II). They do not have the ability to resolve very fine spatial detail, as may be done using lidar, but are able to make aerosol extinction measurements with almost global coverage. They, thus, provide an overall global monitoring capability for stratospheric aerosols, not presently achievable by any other technique. In contrast to the above sensors, the QCM is an in-situ measurement device that both samples, for future study and analysis, as well as determines the aerosol mass distribution function. The collected samples are later studied for size, shape and chemical composition. The QCM has proved itself a very useful instrument for the study of the latter aerosol properties. Its use as a probe for the mass distribution function is still under investigation. The results of these calibration studies are not yet complete and we have been unable to use the mass distribution data in the present analysis.

The main emphasis of the work presented in this report is on the analysis of the stratospheric effects of volcanic eruptions occurring between the launch of the SAM II satellite experiment (October 24, 1978) and October 31, 1980. During this period, four volcanic eruptions occurred that produced observed stratospheric effects; three of these were at low latitudes, one at a midlatitude. Although the effects of these eruptions spread away from the position of the source, relatively little volcanic material reached the polar regions, except from the eruption of Mt. St. Helens on May 18, 1980. Because SAM II observations are confined to latitudes

poleward of about 65°, in contrast to SAGE observations which covered all latitude between about 70° N and 70° S, little SAM II data have been studied and results from this satellite will not be presented here. An extensive study has been made of SAGE data between its launch on February 18, 1979, and October 31, 1980, and a somewhat less detailed study of data up to December 31, 1980. Where lidar data are available, these also have been studied in detail, using that obtained from both ground-based and airborne systems and this analysis has been carried through in less detail to data obtained in the summer of 1981. For the reason given earlier, which will be discussed in more detail in Section 3.3, the quartz crystal microbalance data have not been included in this study of volcanic effects.

In this report, separate chapters are devoted to an analysis of the observed effects of each of the three volcanoes--Soufriére, Sierra Negra and St. Helens. Although the eruption of Ulawun occurred within the October 1978 to October 1980 time period, its main stratospheric effects did not take place until November or December 1980, and these will only be outlined in Chapters 4 and 9, in comparison with the effects of the other eruptions. It may be noted also, that no significant lidar data are available showing the effects of the Sierra Negra and Ulawun eruptions. Appreciation of the stratospheric effects of volcanic eruptions is most easily made in terms of the background stratospheric aerosol for nonvolcanic periods. For this reason, Chapter 4 is devoted to a discussion of the overall global aerosol variation in 1979 and 1980, covering a period of relatively low volcanic activity as well as one with several significant eruptions. This chapter also contains a discussion of the assumptions made and techniques used to convert aerosol extinction to mass loading.

2. BACKGROUND

2.1 Techniques for Studying the Stratospheric Aerosol

In the Introduction we listed, as the primary aerosol parameters, their concentration, size distribution, shape, composition and refractive index. In order to measure these parameters over as large a range of space and time as possible, a variety of different methods are employed. These may conveniently be divided into in situ and remote techniques, and a list of those more commonly used is given in Table 2.1. Of those listed, only satellite occultation (SAGE and SAM II (McCormick et al, 1979)) has global coverage; analysis of this data has thus added greatly to our knowledge of stratospheric aerosol climatology. Satellite occultation's main disadvantage is that, with a limited number of such satellites in orbit, it is a matter of chance if the observation point happens to be near a region of particular interest, such as a volcanic eruption. This gap is, at present, filled by the use of airborne lidar which may be directed rapidly to a place of interest. Ground-based lidar is valuable because it is able to provide a continuous time history of the behavior of the stratospheric aerosol over a single point on the globe (Swissler et al, 1982). Moreover, lidar systems have a good vertical (ground-based and airborne) and horizontal (airborne) spatial resolution, that is not obtainable from SAGE and SAM II. Aerosol layering and changes related to regional atmospheric dynamics may be particularly well studied using lidar.

Satellite occultation and lidar give only limited information on aerosol size distributions (via multiwavelength measurements) and less on aerosol shape (some information is obtainable from lidar polarization measurements). Information on these is at present obtained using in situ techniques which also sample the aerosol for subsequent composition determination. The in situ techniques may be divided into two classes, impactors (and filter samplers) and optical counters. Measurements made by the latter are most commonly limited to size distribution and concentration measurements only, although a wider range of particle radii, from 0.1 → >1 μm, may be studied, than is possible by direct sampling (Hofmann and Rosen, 1981). Composition and shape measurements on aerosols are made by in situ sampling and subsequent analysis. Filter sampling (Lazrus and Gandrud, 1974; Gandrud and Lazrus, 1981) using both aircraft and balloon platforms is used to provide, both an elemental analysis of the collected aerosol, and to estimate the mass mixing ratio of the dominant stratospheric sulfate constituent. Aerosol size distribution is difficult to obtain directly from filter sampling and more commonly inertial impactors are used for this purpose (Gras and Ayers, 1979; Farlow et al, 1981). Impacted particles are directly examined by electron microscope and sized over a wide range (radius $\geq$0.03 μm). Problems arise with deformation of the particle upon impact, particularly for liquid droplets and considerable errors may arise, especially with the larger particles.

TABLE 2.1: TECHNIQUES FOR STUDYING THE STRATOSPHERIC AEROSOL

Method or instrument	Parameters measured (or deduced)	Coverage possible
Remote		
Satellite occultation -SAGE and SAM II	Aerosol extinction (concentration + some information on size distribution)	Global, tropopause or below to 35 km
Ground-based and airborne lidar	Aerosol backscatter (concentration + some information on size distribution and shape)	Single location (ground-based), regional (airborne), 0 → 30 km
In Situ		
Airborne inertial impactor -Wire collector, QCM, etc.	Size distribution and concentration, shape, composition. Mass distribution.	Regional, 0 → 20 km
Balloon and airborne filter samplers	Composition, aerosol mass mixing ratio	Regional, 0 → 20 km (aircraft), → 30 km (balloon)
Balloon and airborne light scattering particle counters	Size distribution and concentration (including condensation nuclei)	Regional, 0 → 20 km (aircraft), → 30 km (balloon)

It should be noted that lidar and statellite occultation measurements extend throughout the stratospheric aerosol layers (tropopause → 35 km). Balloon sampling has the same vertical coverage but in situ airborne measurements are limited to about 20 km maximum altitude. For many purposes this is sufficient, but under some circumstances, such as the recent eruption of El Chichon, which injected material up to 30 km, airborne measurements may not provide sufficient coverage.

2.2 The Nature and Behavior of the Stratospheric Aerosol

The stratospheric aerosol is relatively simple compared to the tropospheric aerosol. Nevertheless, it has certain properties and characteristics which will be outlined in this section before proceeding to a discussion of the new data obtained by SAGE and lidar and, in particular, the volcanic effects. The various aspects, which we shall review briefly only, are as follows.

1. The variation of aerosol concentration with global location and altitude. Its time variation and the effects of volcanic eruptions.
2. The chemical composition.
3. The aerosol size distribution and particle shape.
4. The sources and sinks for stratospheric aerosols and the in situ chemical and microphysical processes.

Figure 2.1 shows a contour plot of distribution of stratospheric aerosol mass with latitude and altitude, based on data from Rosen et al (1975). The main features are the manner in which the mixing ratio contours follow the height variation of the tropopause, with a maximum mixing ratio about 8 km above the tropopause at all latitudes. Significant variations in this picture occur after a volcanic eruption has injected material directly into the stratosphere (Cadle et al, 1976; Newell and Deepak, 1982; Lazrus et al, 1979). Such an eruption creates a strong local increase in aerosol concentration which rapidly expands to a regional scale and, more slowly, to a global scale. (Cadle et al, 1976, suggests a period of about 6 months for global dispersion.) This is followed by a gradual decay (Swissler et al, 1982) which is quasi-exponential with a decay constant of 6 to 12 months.

The background aerosol in the stratosphere has been shown to consist mainly of sulfate and the model adopted by Russell et al (1981) consisted of 75 percent H_2SO_4 plus 25 percent $(NH_4)_2SO_4$. Near the tropopause this would be contaminated by tropospheric aerosols with both insoluble (soil and silicate dust) and soluble components. Recently, Hayes et al, 1980, and Russell and Hamill (1982) have questioned the existance of $(NH_4)_2SO_4$ in appreciable quantities in the stratosphere and their present aerosol model consists of a H_2SO_4/H_2O moisture in an approximately 3:1 mass ratio. This picture is seriously perturbed after a volcanic eruption injects material

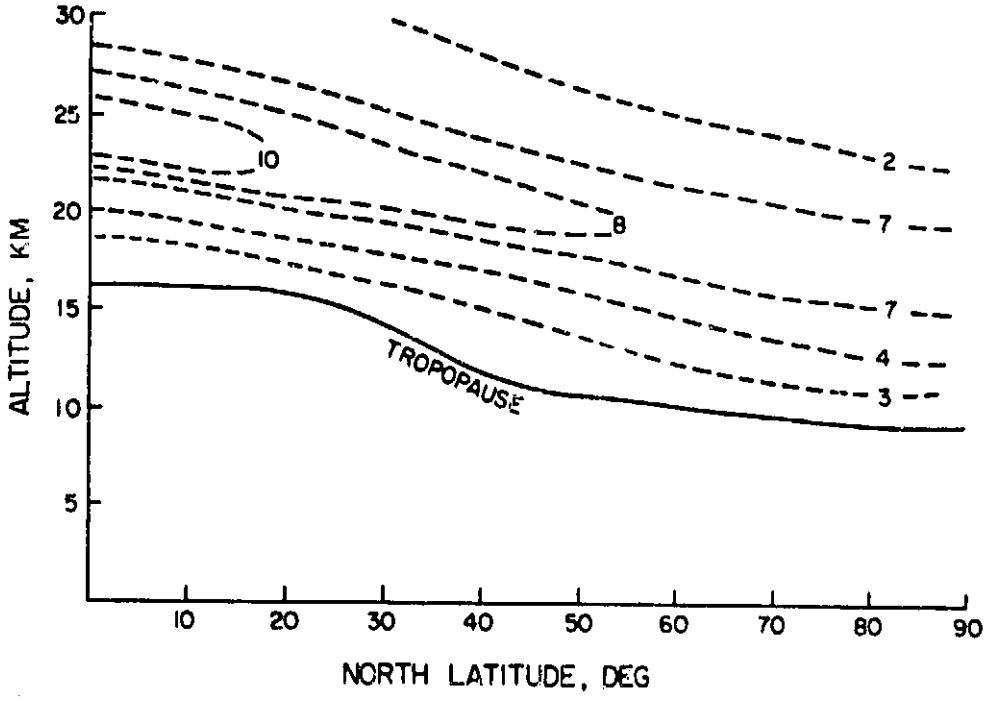

Figure 2.1 Latitude distribution of the concentration of stratospheric aerosols (from Rosen et al., 1975). Numbers on the diagram give the number of aerosol particles per mg of air.

directly into the stratosphere. Solid volcanic ash, consisting of irregular particles with sizes from 0.1 μm to 3.0 μm is present in large quantities along with the liquid and gaseous components (Cadle et al, 1980; Farlow et al, 1980). The larger particles, because of their mass, do not remain long in the stratosphere but fall into the troposphere where they mix and become lost.

Aerosol size distribution are traditionally unimodal (Russell et al, 1981) with a peak in the size distribution (dn/d log r versus log r) at around 0.1 μm (Gras and Laby, 1981). The distribution is narrow and the concentration of particles of radii 1 μm is four to six orders of magnitude lower than that for particles of radii 0.1 μm. There is considerable difficulty in measuring the larger aerosol particles because of their low concentrations and the above picture has been recently challenged by measurements obtained by Hofmann and Rosen (1981). Using a new large particle optical counter, they have detected a second maximum in the aerosol size distribution at a radius near 1 μm. Their results were obtained after the recent eruption of Mt. St. Helens and may not be typical of the long-term background aerosol; nevertheless, they must be considered as a factor that will add additional uncertainty into optical modeling calculations.

The stratospheric aerosol is believed to be formed during volcanically quiet periods from OCS which diffuses upwards from the troposphere. This is supplemented by SO_2 directly injected into the stratosphere by volcanoes (Toon et al, 1979; Turco et al, 1979; Turco et al, 1980a,b). The OCS and SO_2 are oxidized to H_2SO_4 which then nucleates onto small condensation nuclei present in the stratosphere. Particle growth occurs by condensation of H_2O and H_2SO_4 onto the nucleated particles and coagulation by collision also serves to form larger particles. Particles are subject to transport mechanisms--diffusion and sedimentation. At the tropopause particles will be lost by sedimentation; evaporation, particularly at the upper levels, will also act as a particle sink. The interaction of all these factors leads to a very complicated behavior for the stratospheric aerosol and recently attempts have been made to include these in one-dimensional models (see references above). That these have some measure of success may be an indication that, to a first approximation, zonal and meridional variations, in the undisturbed aerosol layer, are secondary to the local physical and chemical processes. Nevertheless, many problems remain, these range from the question of the relative importance of OCS and SO_2 oxidation as source mechanisms for the aerosol to the behavior and nature of both the largest and the smallest aerosol particles. In particular, models are just beginning to be produced for the perturbing effect of volcanic eruptions (Turco et al, 1982). The exact manner in which the new aerosol develops depends upon the actual concentrations of SO_2 and H_2O in the volcanic plume. A maximum optical depth should occur about 3 months after the eruption, followed by an approximately exponential decay, with a time constant of 6 to 12 months.

2.3 Volcanic Eruptions During the Period of Study

The years 1975 to 1979 following the eruption of Fuego in Central America, have formed a relatively quiet period in terms of volcanic eruptions that have had a major effect on the stratospheric aerosol content (Swissler et al, 1982). Since November 1979, there have been several eruptions of significance, culminating in the recent eruption of El Chichon which has produced the largest stratospheric effects since the 1963 eruption of Agung, and possibly earlier. Those recent eruptions believed to be of significance are listed in Table 2.2. One earlier 1979 eruption, that of Soufrière, is also listed, not because of its global influence, which was very small, but because its local effects were quite definite and observed both by airborne lidar and by SAGE satellite (McCormick et al, 1982). This list of eruptions is certainly not complete, even for those that have injected material into the stratosphere (e.g., the eruption of Garoloi in August 1980 (Sedlecak et al, 1981) has not been included) but shows those for which we have definite observations made either by SAGE, or lidar, or both. One reason for this lack of completeness is illustrated by the column heights listed in the table. The majority of these column heights are based on visual estimates, both by experienced and inexperienced observers. It may be noted that the column height shown for Ulawun is only 10 km, well below the tropopause height at the latitude of the eruption. Despite this, there is very little doubt that this eruption produced a marked stratospheric effect. The explanation must lie in either an error in the estimated column height or in another unobserved eruption from the same volcano, possibly at night. Some similar reason probably applies to the eruption of December 1981 to January 1982, for which we are not even sure of the responsible volcano.

In the Introduction, it was noted that this report covers analysis of SAGE satellite data from January 1979 to December 1980, and the corresponding lidar data, where available. During this period four eruptions have been observed, sufficient to be able to deduce some general characteristics common to all. In addition, some further lidar data have been available up to the summer of 1981, covering two more eruptions of importance.

TABLE 2.2: RECENT VOLCANIC ERUPTIONS AFFECTING THE STRATOSPHERE

Date	Volcano	Location	Column Height
April 17, 1979	Soufriére	13.3°N, 61.2°W	18 - 20 km
November 13, 1979	Sierra Negra	0.8°S, 91.2°W	14 km
May 18, 1980	St. Helens	46.2°N, 122.2°W	23 km
October 7, 1980	Ulawun	5.0°S, 151.3°E	10 km
April 27, 1981	Alaid	50.8°N, 155.5°E	15 km
May 15, 1981	Pagan	18.1°N, 145.8°E	13 - 20 km
December - January 1982	Possibly Pagan	--	Lidar at 10 N shows peak at 17 km
March 19, 1982	St. Helens	46.2°N, 122.2°W	14 km
March 28 - April 4, 1982	El Chichon	17.3°N, 93.2°W	26 km

3. DATA SETS AVAILABLE FOR STUDY

3.1 SAGE and SAM II (McCormick et al, 1979)

The SAM II experiment was launched on board the NIMBUS-7 satellite on October 23, 1978, and has since been making aerosol extinction measurements at a wavelength of 1.0 μm. As indicated in the Introduction, the observations are confined to latitudes polewards of about 65° N and S and, for this reason, have not been extensively studied for volcanic effects. SAGE was launched on February 18, 1979, aboard the AEM-B satellite into a highly processing orbit giving its measurements global coverage. SAGE was designed to make two sets of observations per day--at satellite sunrise and sunset, using four radiometer channels. Two of these, at 0.45 μm and 1.00 μm, have been inverted to obtain aerosol extinction coefficients. Due to a partial failure of the satellite power supply, a few months after launch, the observational schedule was reduced in June 1979 to sunset events only and routine data were obtained for these until the final satellite failure in November 1981.

During the period of work covered by this report, SAGE data for 1979 and 1980 only were available. The basic transmission data were inverted to obtain a vertical extinction profile at 0.45 and 1.00 μm for each event. The vertical resolution on these profiles is 1 km and, although the data are basically stratospheric, a significant number of the profiles extend downward into the troposphere. The orbit of SAGE is such that approximately 15 sunset (and 15 sunrise events during the period immediately after launch) were obtained each day, separated by 24° in longitude. The latitude of observation changes slowly from pole to pole, a complete cycle taking about 2 months. A list of SAGE movements for the entire satellite life history is shown in Table 3.1.

It must be noted that the SAGE data used in this report were inverted using a preliminary inversion scheme. The effect of this on the data product has been twofold:

1. The 1 μm extinction profiles, although close to the best obtainable values, contain small errors. Analyses carried out at a later date have shown that any systematic error is probably very small (<3 percent) but that individual data points may be in error by as much as 10 percent. In terms of the volcanic effects to be discussed, such an error is small and not likely to change the main conclusions, qualitatively or quantitatively.

2. The 0.45 μm channel may contain significant errors and use of the 0.45 μm/1.00 μm ratios based on the preliminary inversion scheme

TABLE 3.1: SAGE GLOBAL MOVEMENTS

Date	Day No.	Latitude of Sunset Events	Latitude of Sunrise Events	Comments
Feb 21, 79	52	60.0°S	49.4°N	First data
Mar 3	62	29.3°S	57.7°N	Sunrise northern limit
Mar 22	81	64.6°N	31.0°S	Sunset northern limit
Apr 5	95	38.3°N	58.5°S	Sunrise southern limit
Apr 29	119	52.2°S	41.9°N	Sunset southern limit
May 14	134	19.9°S	71.3°N	Sunrise northern limit
May 18 - 25	138 - 145			Sunlit period
May 30	150	68.1°N	27.0°S	Sunset northern limit
June 10	161	49.1°N	46.5°S	Sunrise southern limit
June 12 - Aug 3	163 - 215			Data very erratic
Jul 25	206		60.3°N	Final sunrise data
Aug 4	216	65.6°N		Start sunset data only
Aug 7	219	73.2°N		North limit
Sep 13	256	60.6°S		South limit
Oct 20	293	54.5°N		North limit

TABLE 3.1: Continued

Date	Day No.	Latitude of Sunset Events	Latitude of Sunrise Events	Comments
Nov 21, 79	325	70.1°S		South limit
Dec 31	365	46.4°N		North limit
Jan 14 - 26, 80	14 - 26			Sunlit period
Jan 27		71.3°S		South limit
Mar 4	64	57.1°N		North limit
Mar 26 - Apr 7	86 - 98			Data gap
Apr 8	99	57.1°S		South limit
Apr 30 - May 8	121 - 129			Sunlit period
May 11	132	71.9°N		North limit
June 23	175	46.4°S		South limit
Jul 7 - 19	189 - 201			Sunlit period
Jul 20	202	69.3°N		North limit
Aug 28	241	55.6°S		South limit
Sep 28	272	61.7°N		North limit
Oct 21 - Oct 30	295 - 304			Sunlit period

TABLE 3.1: Continued

Date	Day No.	Latitude of Sunset Events	Latitude of Sunrise Events	Comments
Oct 31, 80	305	74.8°S		South limit
Dec 13	348	46.5°N		North limit
Dec 25, 80 - Jan 10, 81	360 - 10			Sunlit period
Jan 11	11	67.8°S		South limit
Feb 17	48	53.6°N		North limit
Mar 7 - 16	66 - 75			Data gap
Mar 19	78	63.3°S		South limit
Apr 13 - 20	103 - 110			Sunlit period
Apr 21	111	75.7°N		North limit
June 5	156	46.7°S		South limit
June 16 - 29	167 - 180			Sunlit period
Jul 1	182	66.7°N		North limit

TABLE 3.1: Concluded

Date	Day No.	Latitude of Sunset Events	Latitude of Sunrise Events	Comments
Aug 10, 80	222	50.9°S		South limit
Aug 28 - Sep 3	240 - 246			Data gap
Sep 4	246	72.8°N		North limit
Oct 2 - 11	275 - 284			Data gap
Oct 12	285	70.9°S		South limit
Nov 18	322	46.7°N		Data ends

should be made with extreme cautior. Use of such data will not be further discussed in this report.

3.2 Lidar

NASA-LaRC is currently using two lidar systems to study stratospheric aerosols. One is a large ground-based system located in Hampton, VA (37° N, 76° W) which operates using a ruby laser (0.6943 μm). The other is an airborne system which has the capability of operating using either a ruby laser or a Nd:YAG laser (1.06 μm).

The ground-based system has been in use for many years, it has a receiving mirror with a diameter of 48 inches and a ruby lidar with an available output energy of 2½ J at 0.1 Hz (McCormick, 1975). The system has been in fairly continuous operation since 1974 and a good long term data set has been built up for scattering from stratospheric aerosols (McCormick et al, 1978; Swissler et al, 1982) which clearly shows volcanic effects. These observations have continued through to the present time covering, in considerable detail, the period (January 1980 to June 1982) discussed in this report.

The airborne lidar system is of more recent construction, particular in terms of the availability of the Nd:YAG channel. Special missions have been flown to investigate the stratospheric effects following volcanic eruptions (McCormick, 1982; Kent, 1981) and the system has been used to assist in the validation of SAGE/SAM II satellite data (McCormick et al, 1983; Russell et al, 1981). Table 3.2 shows a list of missions flown between April 1979 and June 1981, the data from which will be discussed in this report.

3.3 Quartz Crystal Microbalance

In November 1978, a set of correlative experiments was carried out over Söndrestrom, Greenland, with the objective of testing the validity of the data obtained by the SAM II experiment (Russell et al, 1981). As part of this series of experiments a quartz crystal microbalance was flown on board a Sabreliner aircraft at altitudes of 9.5 to 12.5 km. The QCM is a multistage impactor that allows aerosol particles to be separated into ten different size fractions between 0.045 and >22 μm. The mass of aerosol within each size range is determined from the change in resonant frequency of the piezoelectric crystals used as collection surfaces (compared to a reference crystal) and constituent composition is obtained from post-flight SEM analysis of the samples. Data taken at various flight altitudes during this series of experiments has been made available to us for analysis.

TABLE 3.2: LANGLEY RESEARCH CENTER AIRBORNE

LIDAR FLIGHTS BETWEEN APRIL 1979 AND JUNE 1981

Date	Flight Area
April 14-20, 1979	Caribbean and Brazil
May 21-28, 1980	Eastern USA and Canada
Sept. 16-24, 1980	Virginia to Washington State, USA and return
Dec. 9-15, 1980	New York State, USA and Frobisher Bay, Canada
June 27, 1981	Virginia Coast, USA

Because it has been discovered with the Söndrestrom measurements that the techniques employed with the QCM, in particular the crystal coatings and temperature pairings were inadequate for stratospheric measurements, it is considered that the Söndrestrom data set is of poor quality. Through additional experience with stratospheric flights on the U-2 aircraft, these techniques have been improved considerably. In addition, calibration studies are being conducted under similar stratospheric conditions which will further refine the instrument accuracy. As these studies are not yet complete, we decided against the use of QCM data, in our study of volcanic effects, even where such data exists.

A brief discussion of our own analysis of the Söndrestrom data is given in Section 8 of the report and, in somewhat more detail, in the Appendix.

4. GLOBAL STRATOSPHERIC AEROSOL CONCENTRATIONS, FEBRUARY 1979 - DECEMBER 1980

4.1 Conversion of Satellite and Lidar Data to Mass Loading

The SAGE and SAM II satellite systems and lidar measure respectively the aerosol extinction and aerosol backscatter at certain wavelengths. These are optical quantities, which can only be converted to aerosol concentrations if certain assumptions are made concerning both the scattering mechanism and the aerosol properties. It is commonly assumed that Mie theory may be employed to calculate the optical characteristics, that is, that the aerosols are spherical in shape. This assumption is probably justified when we have an aged aerosol population that is not too close to the tropopause. Immediately, after a volcanic eruption, significant quantities of volcanic ash are normally present along with gaseous and liquid effluents. The ash particles are almost certainly nonspherical and use of Mie theory may lead to serious errors. Development of an alternative theory to calculate scattering from such particles has not been attempted for a variety of reasons. The first is the extreme difficulty of carrying out such calculations for irregular particles although certain shapes, such as ellipsoidal, are amenable to treatment (Schuerman, 1980). More important, perhaps, is that such calculations are normally only required under conditions in which other errors are much larger. Volcanic ash probably only resides in the stratosphere for a few weeks after a significant eruption (Hofmann and Rosen, 1981). During this period the concentrations of aerosol are highly localized and very irregular. Present sampling techniques, including SAGE, do not permit a complete sampling of the aerosol distribution. A few localized values only may be obtained which are then used to estimate the overall distribution. Very considerable errors enter at this stage which are certainly comparable to those involved in assuming the applicability of Mie theory. A further point is that, as indicated above, the ash has a short residence time; from the point of view of understanding the eruption mechanism, it is undoubtedly important, from the point of view of the long term climatic effects of the eruption, it is of secondary importance compared to the sulfuric acid aerosol. Similer arguments may be advanced for the region of the stratosphere just close to the tropopsphere. This is a region of exchange between troposphere and stratosphere and larger particles may occur here. It is also a region in which penetration of the stratosphere by tropospheric cloud takes place. Under such conditions, very large errors in the estimation of stratospheric mass loading may occur and, as will be discussed later, we have tended to ignore this region when calculating mass loading.

Russell et al (1981) have presented an extensive discussion of stratospheric aerosol models and the intercomparison of satellite and lidar data. In this comparison they have used nine different commonly used size distributions and made a detailed error analysis based on these size distribution types and the range of likely refractive indices. In their analysis they have used the dustsonde ratio obtained by research workers at the University of Wyoming, Department of Physics and Astronomy as a key parameter. The dustsonde ratio $N_{0.15}/N_{0.25}$ is defined as the ratio of the number of particles with radii >0.15 μm to that with radii >0.25 μm. There is a large data base on this parameter for stratospheric aerosols and it is a useful single parameter for describing the relative number of large and small particles. Derivation of a conversion factor for the optical scattering or extinction to mass as a function of this ratio is particularly useful as dustsonde measurements are available following the recent volcanic eruptions. In their analysis Russell et al (1981) assume the aerosol to consist of a mixture of sulfuric acid, water and ammonium sulfate. In the inner stratosphere (more than 2 km above the troposphere) they assume the aerosol to consist of an equal mixture by weight of 60 percent H_2SO_4 (n = 1.40), 75 percent H_2SO_4 (n = 1.42), 90 percent H_2SO_4 (n = 1.43) and $(NH_4)_2SO_4$ (n = 1.52). In our calculations, which will be presented below, we have used the same mixture of components.

Recently, Russell et al (1982) have modified their model to take account of one new development and a factor previously omitted from their calculations. Results obtained by Hayes et al (1980) have indicated that the $(NH_4)_2SO_4$ previously believed to exist in the stratosphere, may have been produced in the course of transport and laboratory analysis. Russell et al have deleted $(NH_4)_2SO_4$ from their model and have included the effect of temperature on the refractive index of H_2SO_4/H_2O mixtures. By a curious coincidence the changes in optical scattering and extinction produced by including these modifications cancel almost exactly, leaving the conclusions based on the original model almost unchanged.

Mie calculations have been carried out, using Russell et al's (1981) models of the aerosol size distribution for the extinction (at 1.0 μm) to mass ratio as a function of dustsonde channel. This has been done with both an $H_2SO_4(9)/H_2O(3)/(NH_4)_2SO_4(4)$ mixture at room temperature and an $H_2SO_4(3)/H_2O(1)$ mixture at stratospheric temperatures. Over the channel ratio range 1.2 → 16 the maximum difference between the extinction/mass ratio for the two compositions was less than 2 percent. The curve for the latter is shown in Fig. 4.1 where it can be seen that the ratio can vary between 4×10^2 and 2×10^3 m^2 kg^{-1}. The figure also shows a mean prevolcanic dustsonde ratio as 4.7 (E/M = 1.22 10^3 m^2 kg^{-1}) and a value 100 days after the St. Helens eruption as 5.5 (E/M = 1.10×10^3 m^2 kg^{-1}). These values are essentially the same, being well within the spread of dustsonde ratios (3.5 → 7 at the layer maximum) shown by Pinnick et al (1976) for a range of global soundings. Immediately after an eruption when considerable quantities

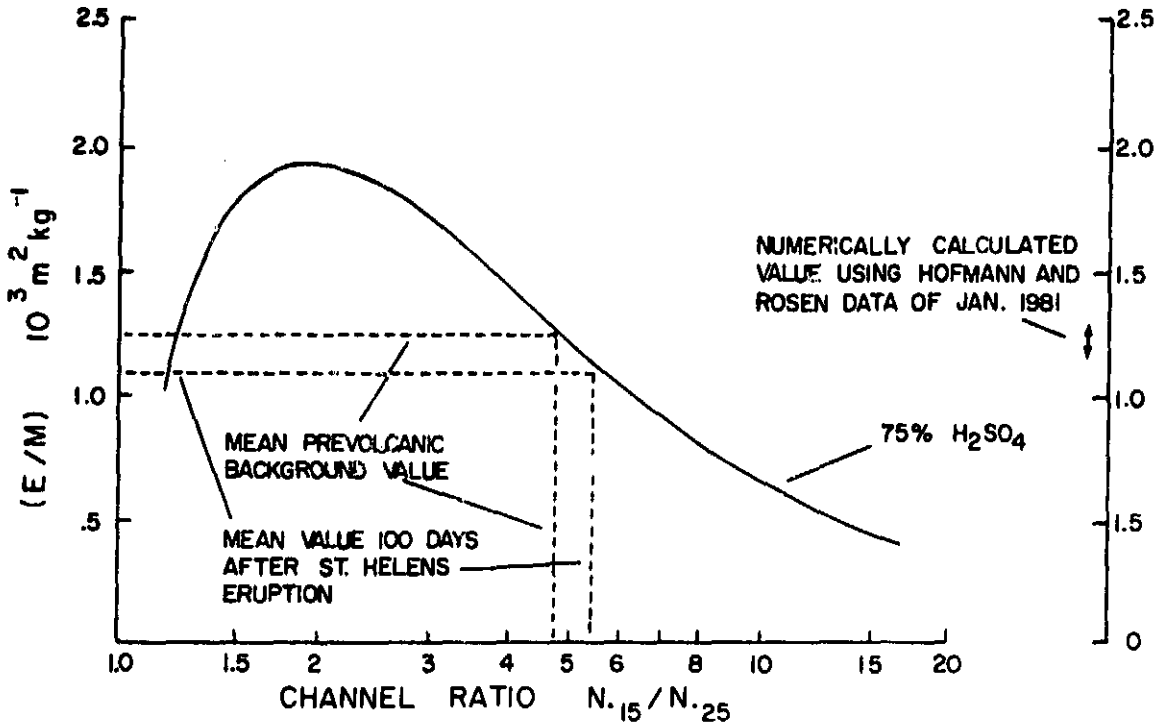

Figure 4.1 Conversion factor for extinction/aerosol mass as a function of dustsonde channel ratio for the inner stratosphere (models were taken from Russel et al., 1981). Also shown is a value calculated using the numerical data obtained by Hofmann and Rosen (1981).

of ash are present, the dustsonde ratios are erratic and the size distribution is then far from the standard values. Also shown in Fig. 4.1 is the result of a numerical calculation using Hofmann and Rosen's data of January 1981 after the eruptions of St. Helens and Ulawun. It can be seen that the value agrees well with those based on the models. This is somewhat coincidental, as analysis of a larger number of postvolcanic size distributions shows that this ratio is variable and that its actual value is uncertain due to the lack of knowledge of the exact concentration of the larger particles with radii of the order of 1 μm. In this report the value 1.22 $m^2\ kg^{-1}$ has been adopted as a single value for converting extinction to mass loading. It should be remembered that this factor is an approximation only.

Less use has been made in this report of lidar data, for the calculation of aerosol mass loading, than of the SAGE extinction data. Russell et al (1981) have discussed in detail the conversion of backscatter cross-sections to extinction cross-sections and expressed their results as functions of model type and dustsonde channel ratio. Over the same range of channel ratios as shown in Fig. 4.1 the backscatter/extinction ratio $B_{0.69}/E_{1.00}$ varies from about 0.02 to 0.10 sr^{-1}. This is shown in different form in Fig. 4.2, where this ratio is plotted as a function of aerosol particle radius. It can be seen that the function has a minimum value for particle radii between 0.2 and 0.7 μm. This is the particle group, for normal stratospheric aerosol distributions, that is responsible for the majority of the backscatter. Where we have found it useful to convert lidar backscatter to equivalent SAGE extinction we have used the conversion factor $B_{0.69}/E_{1.00} = 0.03\ sr^{-1}$. (The corresponding value for $B_{0.69}$/Mass is 36.6 $m^2\ sr^{-1}\ kg^{-1}$.)

4.2 Stratospheric Aerosol Mass Loading

In order to study the stratospheric effects of volcanic eruptions, it is necessary to have a clear picture of the background stratospheric aerosol prior to the eruption. Of particular importance is the stratospheric aerosol mass loading, both from the aspect of the total global mass loading as a function of time and of the aerosol distribution with height and latitude. Some information on these has already been discussed in Section 2.2 but a far more detailed picture has emerged from a study of the 1979 and 1980 SAGE data; this picture will be presented in this section.

Nineteen hundred seventy nine (1979) represented the last year of relatively low volcanic activity. Although Soufriére erupted in April 1979 and produced significant local stratospheric effects, its influence on the global stratospheric aerosol was negligible. The SAGE data between its launch in February 1979 and the eruption of Sierra Negra in November is representative of the background stratospheric aerosol insofar as the term has meaning. These data have been used in several ways. The total global mass loading has been calculated, contour plots of extinction and extinction ratio as a function of latitude have been produced and specific aspects,

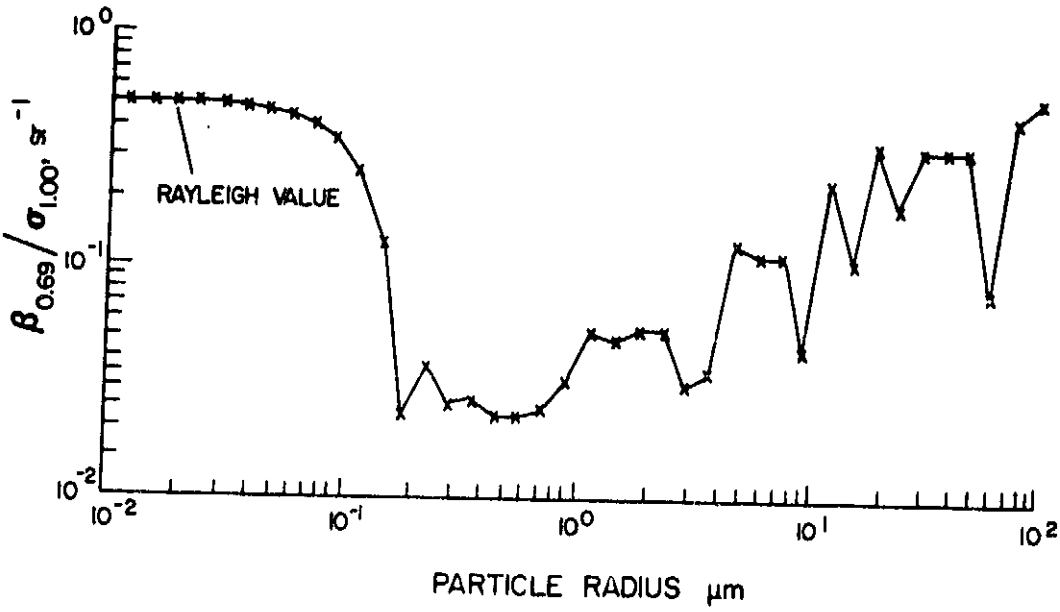

Figure 4.2 The ratio (backscattering function at 0.69 μm)/(extinction cross-section at 1.00 μm) plotted as a function of particle radius.

such as the location of the mixing ratio maximum have been studied in some detail.

SAGE data have been subdivided in sets of measurements, as described in Section 3., representing the movement of the satellite observation point from one latitude extreme to the other. Within each set the data have been further subdivided into 10° latitude intervals and the mean extinction and optical depth calculated within each 10° latitude belt. These data have then been used to calculate the total aerosol mass loading and to plot contour maps of extinction and extinction ratio (aerosol extinction/molecular extinction).

An example of one such contour map for aerosol extinction is shown in Fig. 4.3 for the period March 22 to April 28, 1979. The units used in this figure for extinction are 10^{-4} km^{-1} and the data have been plotted between altitudes of 5 and 35 km. Also plotted on the same figure is the height of the tropopause as a function of latitude. The lines of constant extinction are, to a first order of approximation, parallel to the tropopause altitude. The height of peak stratospheric extinction, which is not clearly shown in the figure, occurs a few kilometers above the tropopause. Below the peak the extinction is fairly constant and near the tropopause the situation is very confused, particularly in low latitudes, by occasional cloud which penetrates the tropopause, producing very high extinction values.

The companion plot to Fig. 4.3 showing extinction ratio rather than extinction is shown in Fig. 4.4. This is remarkable for a strong maximum, about 10 kilometers above the tropopause in equatorial regions, and a continuing ridge at the same altitude above the tropopause extending to high latitudes. The penetration of the tropopause by cloud in low latitudes is still clear and it is interesting to note the extinction ratio minima at tropopause heights occurring near the tropopause folding region in latitudes 25° to 35° N and S. Complete sets of contour plots of extinction and extinction ratio are shown for 1979 and 1980 in Appendix 2.

One particular feature of the stratospheric aerosol layers that has emerged from the SAGE analysis is a marked break between the equatorial and midlatitude layers. This is not shown clearly in Figs. 4.3 and 4.4 due to the latitude smoothing in these plots. Fig. 4.5 shows the data for approximately the same period (Spring 1979) plotted in a slightly different form. This figure shows a probability contour plot for the occurrence of the extinction ratio peak. The data are thus similar to that shown in Fig. 4.4, but is obtained from a study of individual scattering profiles rather than a zonal average. This figure is clearly broken into three sections, one over the equator, the others polewards of latitude 30°. There appears a strong height discontinuity at 20° to 30° coincident with the so-called tropopause break or folding region. Fig. 4.6 shows the same data plotted as a function

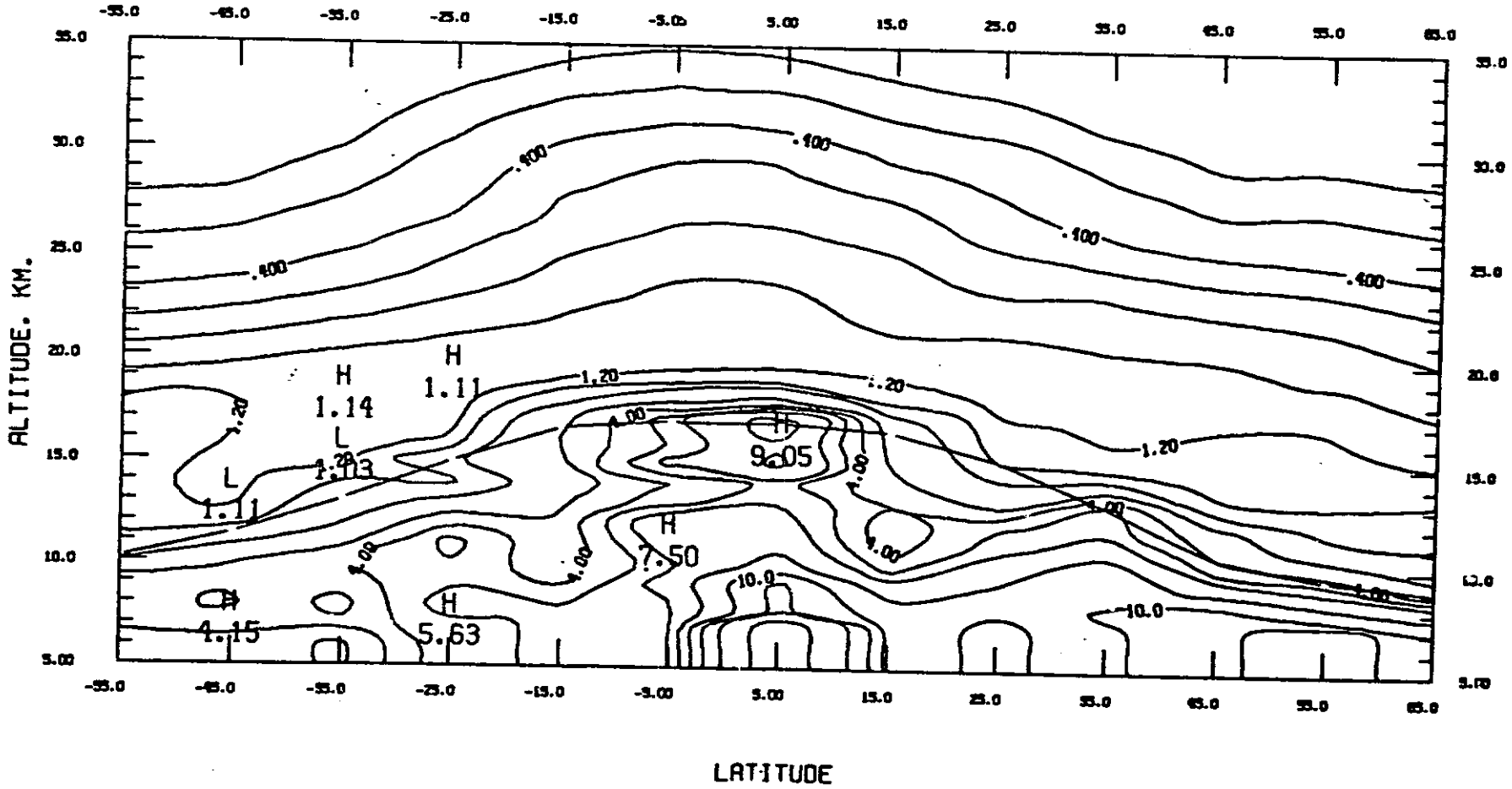

Figure 4.3 Contour map for aerosol extinction for the period March 22–April 28, 1979. Units used are 10^{-4} km^{-1}.

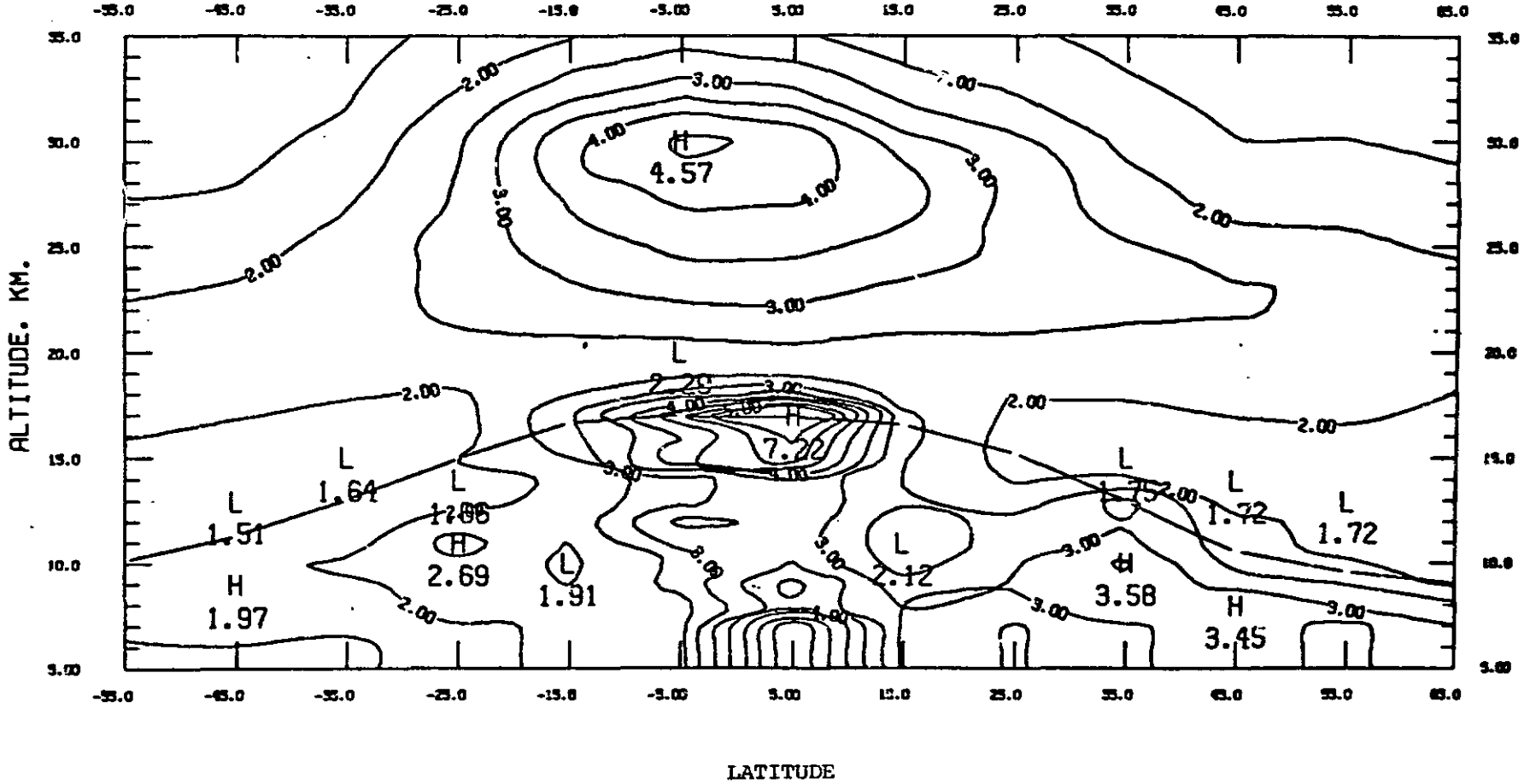

Figure 4.4 Contour map for aerosol/molecular extinction ratio for the period March 22–April 28. 1979.

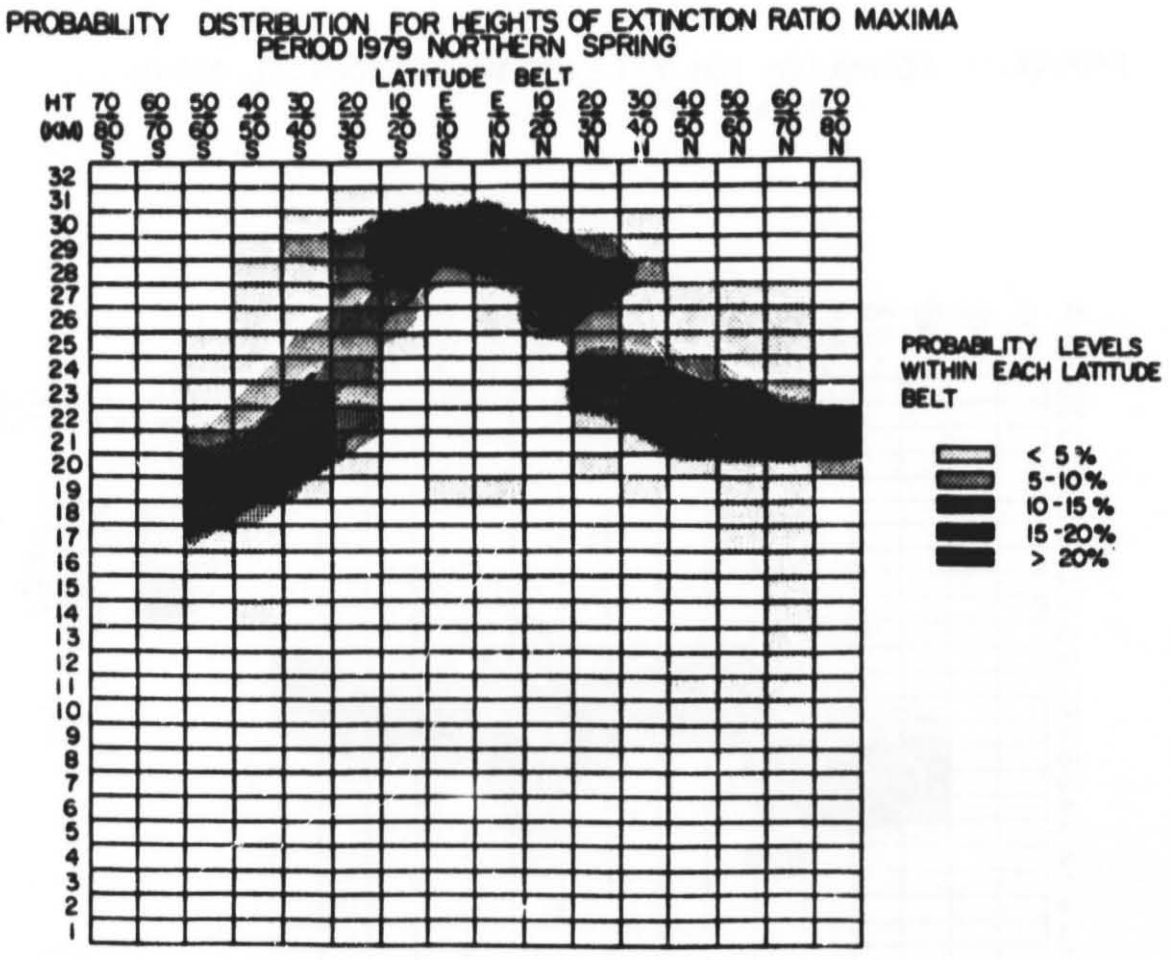

Figure 4.5 Contour plot showing the probability distribution for the height of the aerosol/molecular extinction ratio maximum at different latitudes. The data in the plot are for the period March 1–May 31, 1979.

PROBABILITY DISTRIBUTION FOR (EXT. RATIO MAX.-TROPOPAUSE) HEIGHTS
PERIOD 1979 SPRING

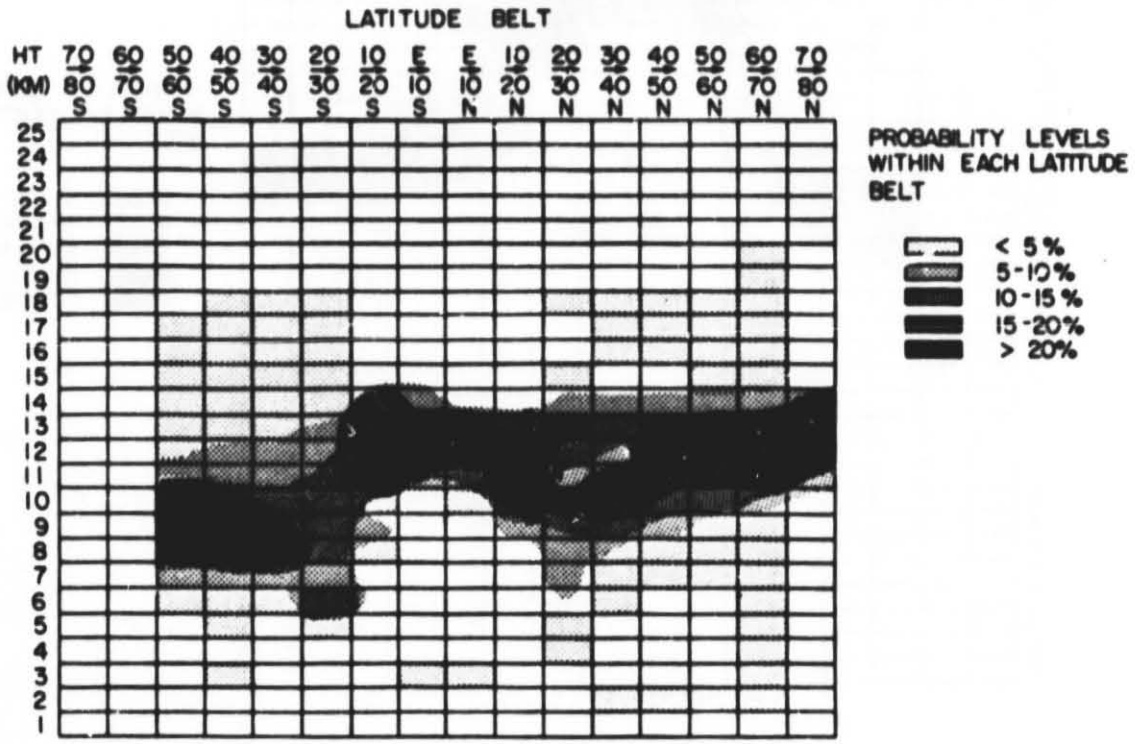

Figure 4.6 Contour plot showing the probability distribution for the altitude differences between the peak aerosol/molecular extinction ratio and the tropopause. Data in this plot are for the period 1 March-May 31, 1979.

of altitude above the tropopause rather than absolute altitude, the difference altitude being calculated for each SAGE event. A mean altitude difference of 10 km is apparent, together with a slight hemispheric asymmetry. Of particular interest is the tropopause folding region where the altitude difference shows its minimum value, suggesting that stratospheric material may be drawn down at these latitudes. Similar plots are obtained for the other seasons, all showing the same behavior near the tropopause folding regions and also showing seasonal variations, as well as a hemispheric asymmetry.

Mass loading calculations have been made, based on the same data subdivisions. The extinction values within each 10° latitude belt have been used to calculate the total stratospheric aerosol optical depth which has then been integrated for each hemisphere. Ideally, in calculating the stratospheric aerosol optical depth, the aerosol extinction should be integrated for all levels above the tropopause. This approach can lead to errors. It is clear from our own data, and from other published data, that clouds can penetrate the tropopause, leading to high extinction levels which, if included, would distort the integrated values which are hopefully obtained for aerosol alone. In addition, the tropopause levels used are based on a global grided analysis and may not be exactly correct for the region in which the SAGE measurement is made. For these reasons, it was decided (a similar approach was used by Russell et al, 1981) to calculate the optical depth from a height 2 km above the tropopause. A further complication was introduced in May 1980, when the algorithm used to derive the tropopause heights was modified, resulting in significant errors in the estimated heights over certain latitude bands. This error was not corrected until 1981 and in order to avoid a data discontinuity, a model rather than the actual tropopause height has been used in most of the calculations presented in this report.

A typical result for the latitude variation of the stratospheric optical depth, defined as above, is shown in Fig. 4.7 for the period March 22 to April 28, 1979. This figure shows minimum optical depth at latitudes of 20° to 30°, typical of all prevolcanic and some postvolcanic data. Fig. 4.7 also shows hemispheric asymmetry which appears to be seasonally variable. This variation is shown more clearly in Fig. 4.8, where the mean hemispheric optical depth is plotted as a function of time from March 1979 to December 1980. The times of the three major volcanic eruptions during this period are marked and the right-hand ordinate shows the equivalent hemispheric mass loading using the conversion factor discussed in the previous section. The following points are shown in the figure.

1. Previous to the eruption of Sierra Negra, both hemispheres show a mean mass loading of about 2.5×10^5 tonnes (global total = 5.0×10^5 tonnes).

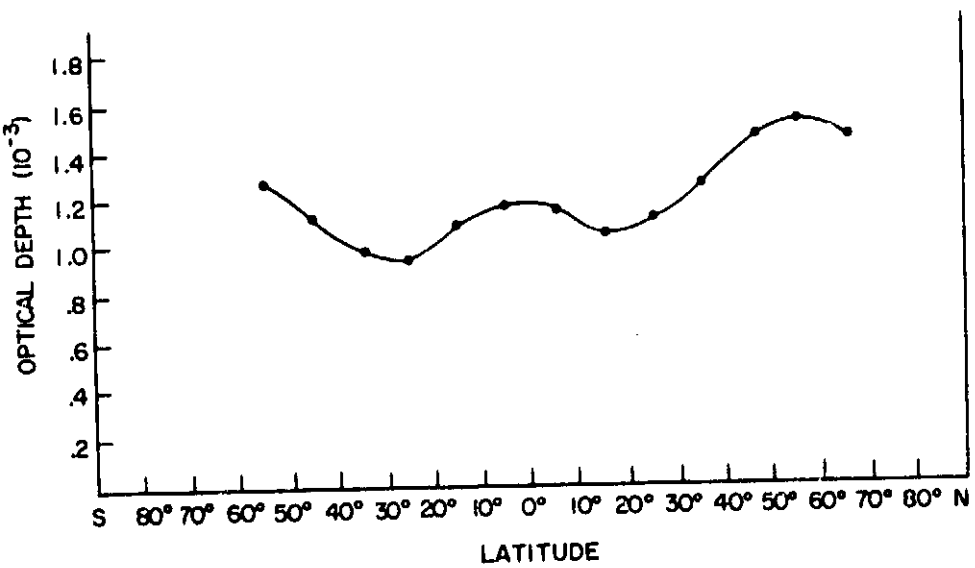

Figure 4.7 Latitude variation of the mean stratospheric optical depth (measured from two kilometers above the tropopause) for the period March 22–April 28, 1979.

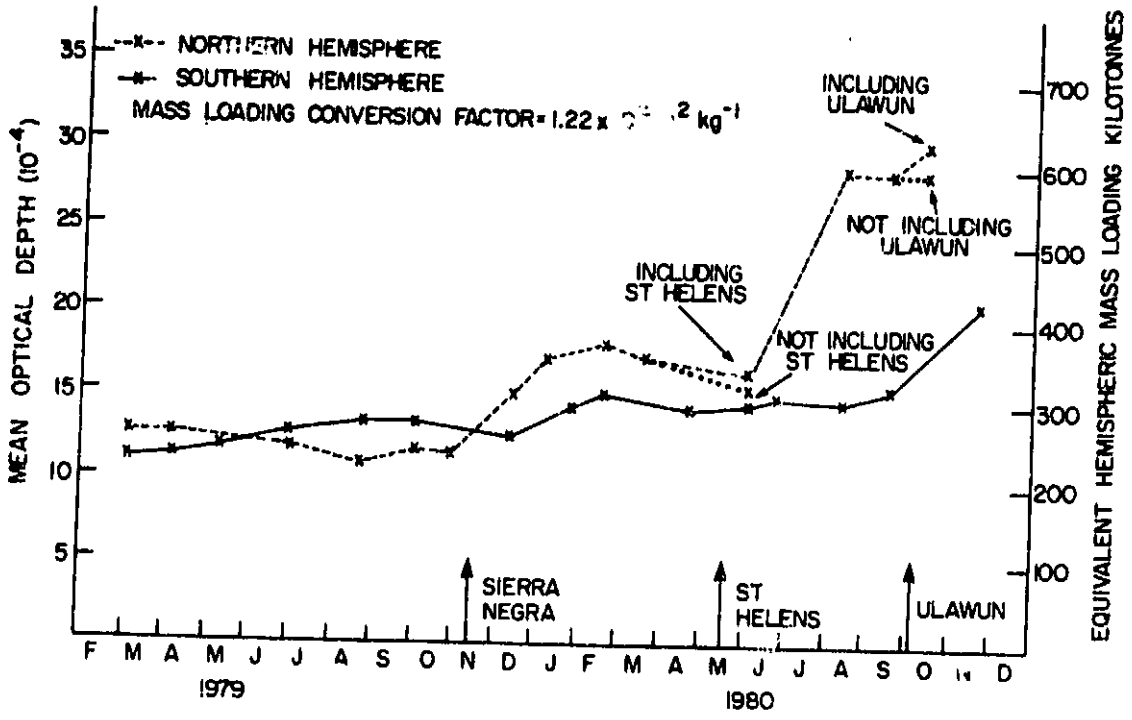

Figure 4.8 Mean hemispheric optical depth, as determined by the SAGE satellite between February 1979 and November 1980.

2. Superimposed upon the mean level than is a seasonal fluctuation with a peak amplitude of about 8 percent. The peak optical depth occurs in later winter - early spring.

3. The three volcanoes marked on the figure all produced stratospheric effects. Full details of the first two of these eruptions are given in Sections 6 and 7. The following is a brief summary of the global behavior of each.

   (a) Sierra Negra: This was an equatorial eruption occurring in November 1979. The movement of the stratospheric input was asymmetric, the majority (at least 60 percent of the injected mass) moved into the northern hemisphere. The maximum stratospheric effect was reached about 3 months after the eruption when the increase in total mass loading was about 1.8×10^5 tonnes or about one-third of the previous background total. In May 1980, it is still possible to separate the effects of Sierra Negra from those of St. Helens. At this time (3 months after maximum loading) the increase due to Sierra Negra has fallen to less than 1.0×10^5 tonnes.

   (b) St. Helens: St. Helens erupted on May 18, 1980, at 46° N. The majority of the injected material moved northwards and relatively little entered the southern hemisphere. A flat maximum in loading was reached 2 to 4 months after the eruption. The eruption of Ulawun occurred too soon after that of St. Helens for the expected decrease to be easily separated. It is, however, anticipated that a study of the 1981 data will assist in this respect. The total loading increase produced by St. Helens was approximately 3.0×10^5 tonnes--an exact estimate being difficult to make on account of the remaining influence of Sierra Negra. Of this total, it seems likely that about 90 percent remained in the northern hemisphere up to September 1980.

   (c) Ulawun: The eruption of Ulawun was equatorial, similar to that of Sierra Negra. Unlike Sierra Negra, the stratospheric input did not move rapidly away from the equator. The 1980 data does not show the peak effects of the eruption, but it is anticipated that they will be contained in the 1981 data. In late November 1980, the increase in southern hemisphere mass loading due to Ulawun was approximately 1.1×10^5 tonnes. A slightly smaller amount entered the northern hemisphere (the hemisphere total is not available due to the SAGE orbital characteristics) giving a total extra loading 6 weeks after the eruption of about 2.0×10^5 tonnes. It is to be anticipated that the 1981 SAGE data will show an increase up to a level comparable with or slightly less than that from Mount St. Helens.

   A summary of the above information is given ir Table 4.1.

TABLE 4.1: STRATOSPHERIC AEROSOL MASS LOADING CHANGES

1979 - 1980

Subject	Mass Loading (10^5 tonnes)		
	Northern Hemisphere	Southern Hemisphere	Global Total
Background (northern winter)	2.5	2.3	4.8
Background (northern summer)	2.2	2.7	4.9
Sierra Negra (peak increase - February 1980)	1.1	0.7	1.8
St. Helens (peak increase - September 1980)	~2.8	~0.2	~3.0
Ulawun (6 weeks after eruption)	~0.9	~1.1	~2.0

5. STRATOSPHERIC EFFECTS OF THE ERUPTION OF SOUFRIERE
(McCormick et al, 1981; McCormick et al, 1982; Kent, 1981; Fuller et al, 1982)

5.1 Introduction

The Soufrière volcano is located on the Caribbean island of St. Vincent (13.3° N, 61.2° W, see Fig. 5.1) and erupted several times in April 1979, sending material to stratospheric heights (Shepherd et al, 1979). Approximately 10 days after the first major eruption, SAGE made measurements at the latitude of St. Vincent while moving from south to north. Events showing enhanced extinction in the stratosphere, attributable to material from the volcano, were observed. Similar but rather weaker events were noted as SAGE moved north during the subsequent week, and the effects disappeared at a latitude of about 40° N. Detailed times and estimated column heights of the various eruptions are listed in Table 5.1 (Shepherd et al, 1979). As for other column height estimates shown in this report, it should be remembered that these are estimates only and subject to considerable error.

At the time of the first eruption the NASA P3 aircraft carrying the airborne lidar system was on a mission in Brazil. It was directed to the location of the volcano and arrived in time to observe the largest eruption of the series on April 17, 1979. On the following day, a mission was flown in the neighborhood of the volcano in order to use the lidar system to study possible stratospheric injection of material by the eruption.

5.2 Lidar Observations

The flight path for the lidar mission of April 17-18 was determined on the basis of local meteorological observations made in Trinidad (11° N, 62° W, see Fig. 5.2). Strongly scattering layers were observed above the local tropopause (h ≈ 16 km) with aerosol/molecular scattering ratios as large as 100 (see Fig. 5.2 for the height of these layers). These were thin (less than 1 km in thickness) and extended up to 20 km altitude. Strong shearing had occurred, with different parts of the plume moving in different directions. Examples of the scattering profiles, typical of those to be observed immediately after a volcanic eruption are shown in Fig. 5.3. The plume movements have been interpreted in terms of the high altitude wind systems as measured at Trinidad and will be discussed below in Section 5.4.

5.3 SAGE Observations

An example of a typical low-latitude background aerosol extinction profile observed by SAGE is shown in Fig. 5.4(a). No enhancement over background due to a high-altitude plume is present, and the extinction decreases fairly slowly with altitude between about 12 km and 22 km.

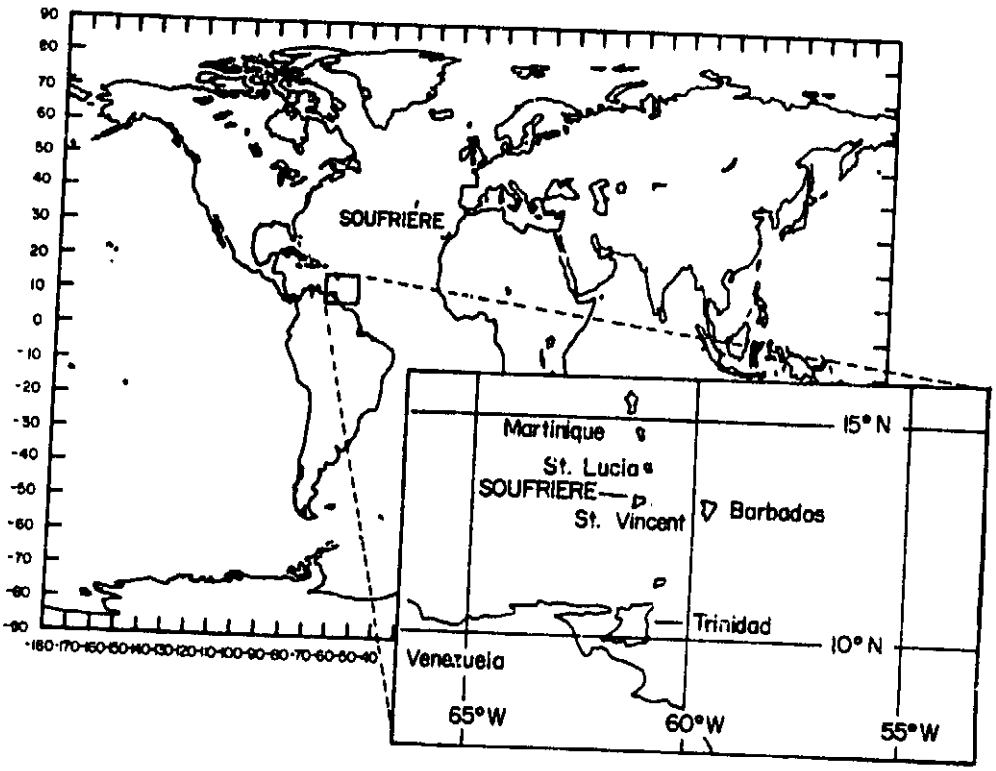

Figure 5.1 Map showing the location of the Soufriere volcano.

TABLE 5.1: DATES AND TIMES OF MAJOR ERUPTIONS OF SOUFRIÉRE VOLCANO

Date	Time, GMT	Estimated column altitude, km
April 13, 1979	2108	17 to 18
April 14, 1979	1550	17 to 18
April 17, 1979	2057	18.7
April 22, 1979	1037	17

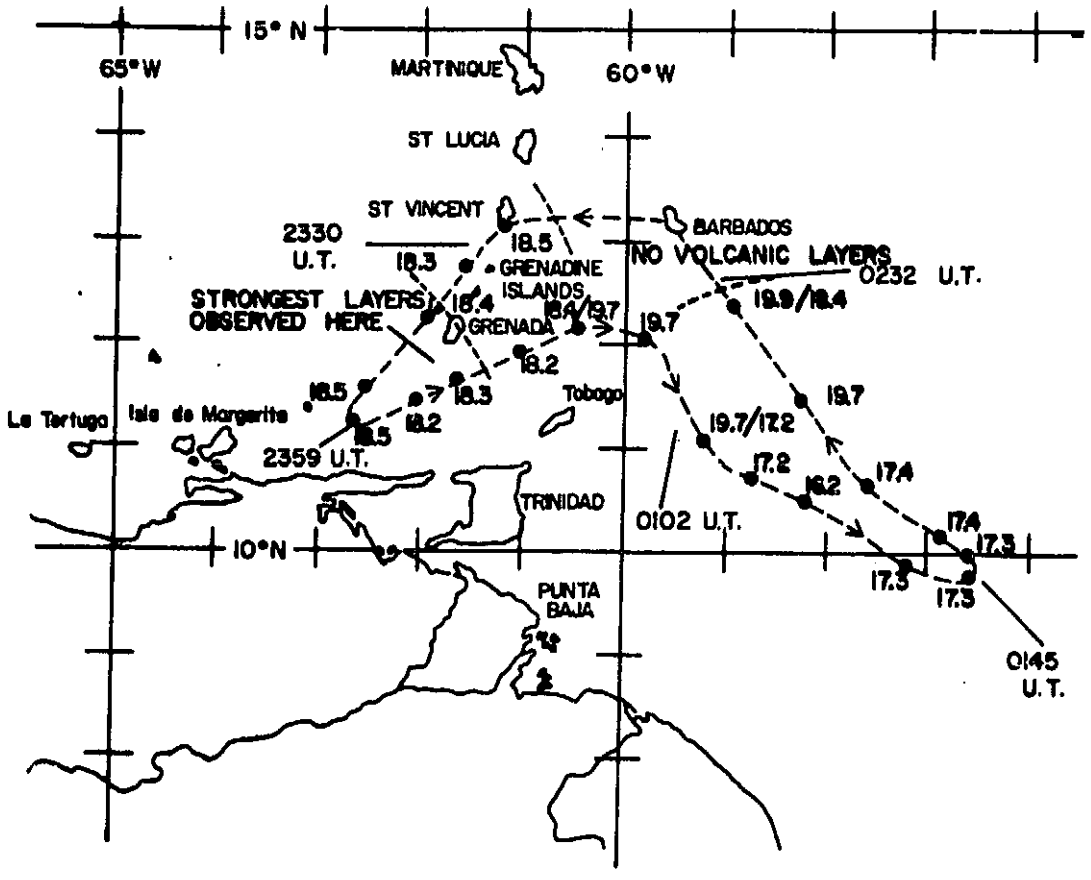

Figure 5.2 Airborne lidar flight path on April 17-18, 1979. Figures shown alongside the flight path are the heights in kilometers of the stratospheric layers observed on the flight.

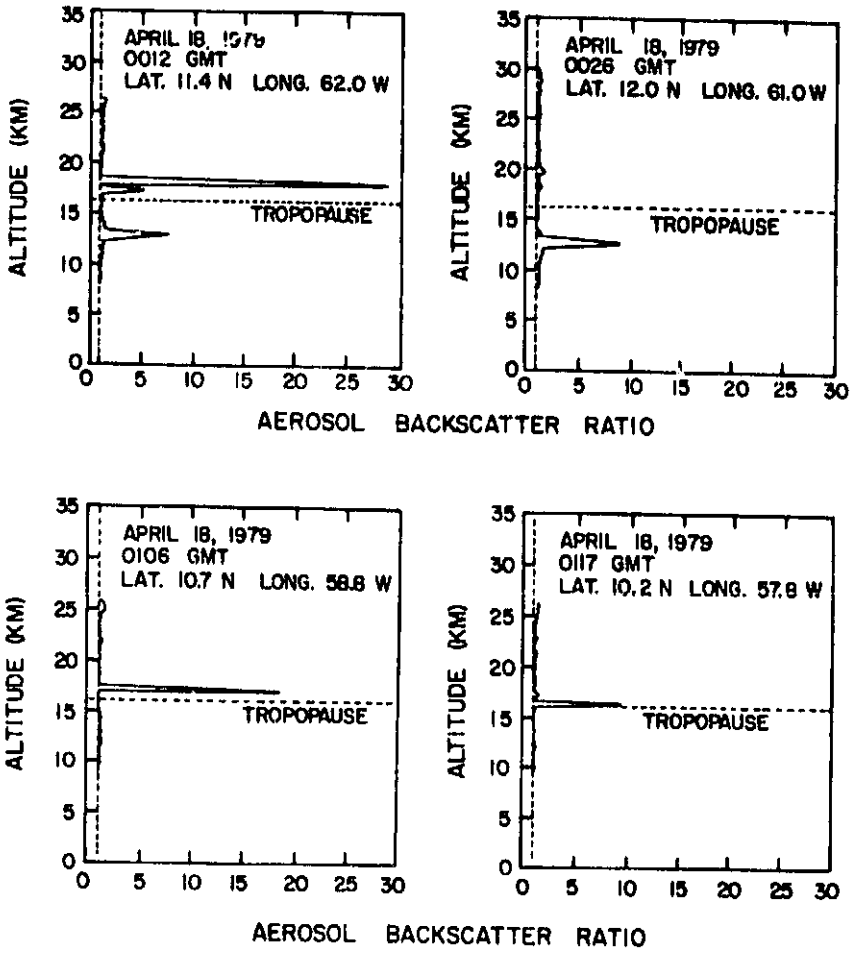

Figure 5.3 Examples of lidar profiles observed in the vicinity of the Soufriere volcano.

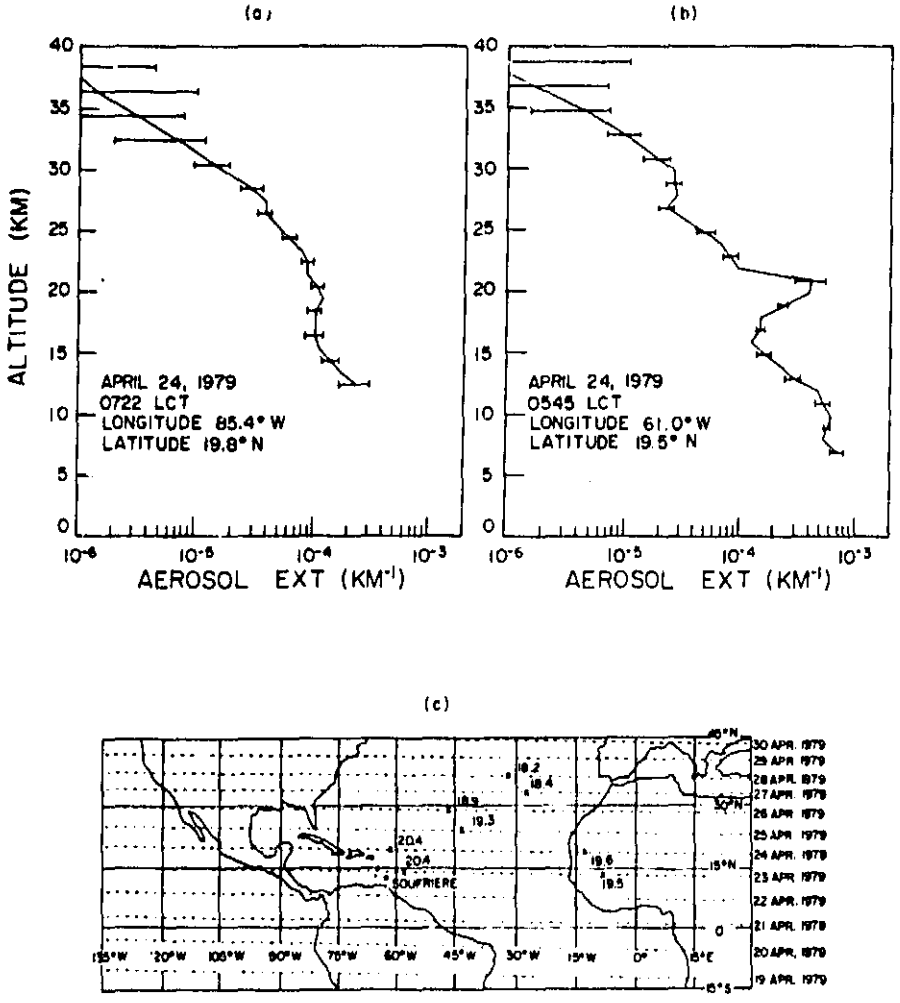

Figure 5.4 SAGE measurements shortly after the April 1979 eruptions of Soufriere.
(a) Normal aerosol extinction profile as determined by SAGE satellite system.
(b) Enhanced aerosol profile observed on April 24, 1979.
(c) Locations of enhanced aerosol extinction (50 percent or more above normal) are marked by crosses. Altitude of each layer peak is shown in km. Latitudes for each day of SAGE measurements are shown by dashed lines.

Figure 5.4(b) shows the profile obtained on the same day when SAGE was close to St. Vincent. The profile has a maximum which is approximately four times greater than normal at an altitude of about 20.5 km. Such enhanced values were observed on at least eight occasions after the Soufiére eruptions in April. Figure 5.4(c) shows the locations of these events. The events shown in this figure have been restricted to occurrences on which the enhancement was 50 percent or more above the normal value at that height and latitude, and with a peak at least 2 km above the tropopause. The latter restriction has been included to eliminate records with a possible contamination from tropospheric high-altitude water or ice clouds.

Two groups of events are seen, one over West Africa and the other over the Atlantic Ocean. These two groups are believed to be related to separate volcanic eruptions, and their interpretation is discussed in more detail in the next section. The plume which moved northeast over the Atlantic Ocean gradually descended. This is shown in more detail in Fig. 5.5 where both the layer and the tropopause height descend in a similar manner as latitude increases.

In Fig. 5.6(a), the SAGE data have been redrawn in a slightly different form with the tropopause plus 2 km restriction removed. Shading is used to indicate the various plumes and their altitudes. All information for heights down to 18 km has been included. At the lower latitudes, the tropopause was occasionally above 17 km. Nevertheless, both areas of high extinction now show extensions at low altitudes toward the south. These extensions are probably associated with the volcanic emissions and not cirrus clouds.

5.4 Interpretation of the Observations on Dispersion

In order to estimate the mass and interpret the dispersion of the material injected into the stratosphere, the SAGE and LIDAR observations must first be related to the individual volcanic eruptions. The interpretation of the SAGE data in terms of the individual explosions is not immediately obvious. In order to analyze movements of the stratospheric plumes in detail, it is desirable to have as much high-altitude meteorological information as possible from the vicinity of the volcano and along the plume trajectory. Unfortunately, in this case, the observed trajectories lie over the Atlantic Ocean, where there are no meteorological stations. A large-scale analysis, therefore, would seem to offer the best hope for calculating the possible plume movements. Global maps of temperature and geopotential height for this time period were obtained from the National Oceanic and Atmospheric Administration (NOAA). These maps were based on a combination of satellite and rawinsonde observations (Smith et al, 1979). Use has also been made of high-altitude wind data (rawinsonde) from Barbados (150 km east of St. Vincent) and Trinidad (250 km south of St. Vincent).

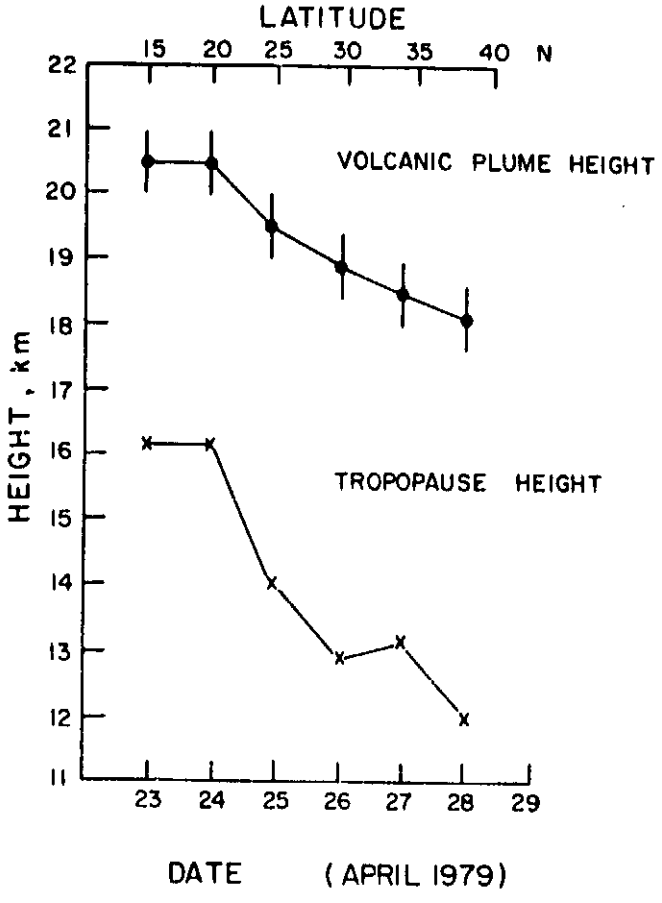

Figure 5.5 Variation in height of the volcanic plume as it moved northwards over the Atlantic Ocean and of the corresponding tropopause for these locations.

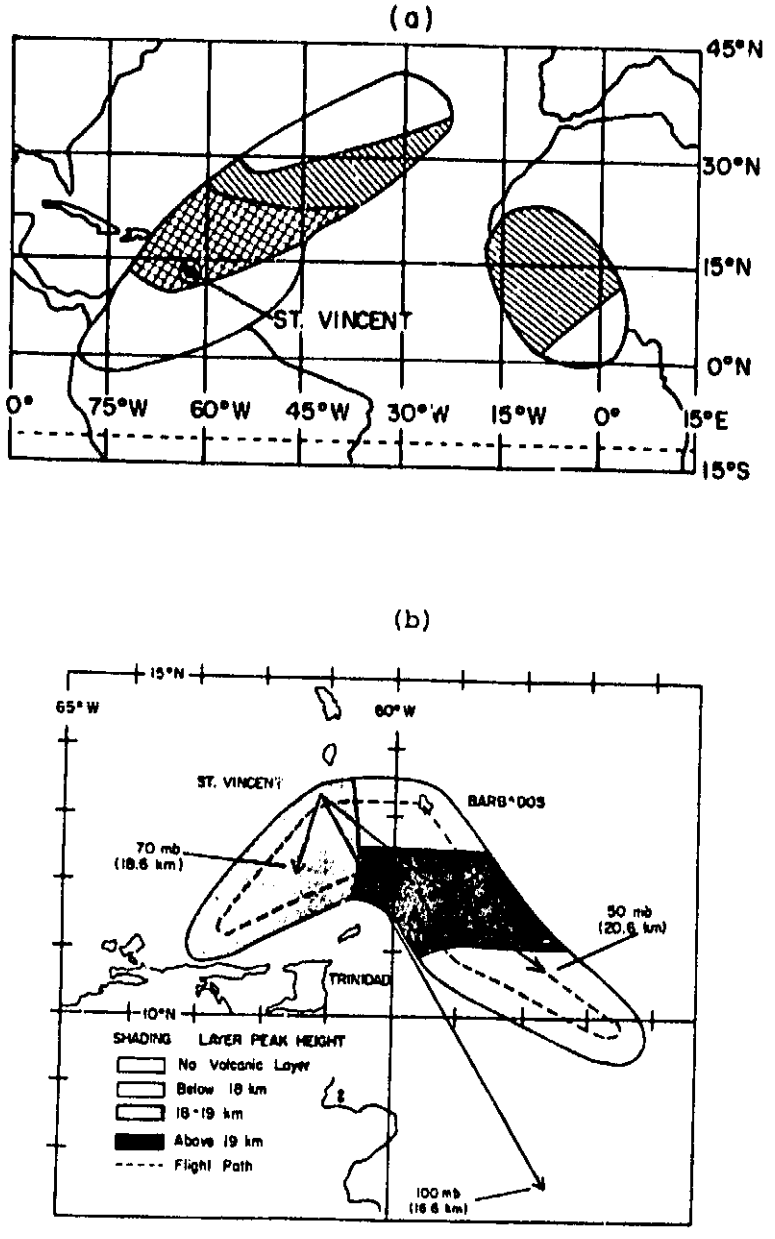

Figure 5.6 SAGE and lidar measurements of Soufriere plumes.

(a) Map showing areas and altitudes of enhanced extinction (50 percent or more above normal) as observed by SAGE between April 21 and 28, 1979.

(b) Airborne lidar observations in the vicinity of St. Vincent, April 18 and 19, 1979. Also shown are the calculated air movements at three pressure levels during the interval between the eruption at 2057 GMT on April 17, 1979, and the time of the flight.

While interpretation of the SAGE data has been made using a combination of local and global wind trajectory analysis, that for the lidar data are more usefully made using the local meteorological data only. In contrast to the SAGE observations, where identification of the plume responsible for a given observation is a significant problem, the lidar observations almost certainly relate to the eruption of April 17. Fig. 5.6(b) shows the data of Fig. 5.2 redrawn in simplified form and estimates of the movements expected from high altitude winds superimposed. The latter are based on a combination of meteorological information from Barbados and Trinidad and show a generally southerly movement with strong shear. There is, in general, very good agreement between the lidar observations and the observed wind measurements both in terms of the general southerly movement and the rather complicated shear pattern. It should also be noted that the lower level material would be expected to move along the vectors for the 70 and 100 mb levels, in rough agreement with the SAGE map shown in Fig. 5.6(a).

In order to discsuss the SAGE observations, it is necessary to review the general characteristics of the low-latitude winds in the vicinity of the volcanoes, which show the following main features.

1. A strong zonal component, along with a weak and somewhat erratic meridional component.

2. A reversal in the zonal component at a height of 19 to 20 km. The wind direction above this height is toward the west and below it toward the east.

3. A fairly rapid increase in wind speed with increasing latitude. The profile and height of the zonal wind reversal remain similar.

Trajectories for the material injected into the stratosphere by the explosions of April 13 and 17 have been calculated (McCormick et al, 1981). These calculations were made using winds derived geostrophically from the NOAA geopotential height maps. They were based on the assumption that the injected material remains on the 70-mbar surface (1 mbar = 100 Pa). These trajectories indicate that the material from the explosion of April 13 moved eastward across the Atlantic Ocean and reached the coast of Africa about April 20. The material from the explosion of April 17 commenced moving in an eastward direction but then turned north after it reached longitude 42° W. Both trajectories agree qualitatively with the position of the plumes over West Africa and over the Atlantic Ocean as determined by SAGE, but the trajectory analysis predicts the material arrives at these locations too early. Moreover, the trajectory for the explosion of April 17 does not correspond with the airborne lidar observations. This disagreement is believed to arise because global maps tend to emphasize larger scale features of the flow fields and neglect local fluctuations, and also because the geostrophis approximation used in calculating the trajectory appears

to overestimate wind speeds when used closer to the equator than about 15° N. A detailed comparison was made of winds devised geostrophically from the NOAA maps with the measured values from two groups of Caribbean meteorological stations. The results of this analysis indicate that acceptable agreement was obtained for stations between 16° and 19° N, but for stations between 10° and 13° N, the geostrophic wind exceeded the true wind speed by roughly a factor of two.

A somewhat simpler analysis, based on data from the local Caribbean rawinsonde stations, may be used in attempting to identify the origins of the two plumes. It is clear, from consideration of the velocity required, that the plume seen over West Africa on April 23 and 24 cannot be associated with the explosion of April 22. It could, however, originate with either of the explosions of April 13 and 14 (considered as a single event), or 17. In the former case, an eastward velocity of 7.4 m/s would be required; in the latter, an eastward velocity of 12.1 m/s. The relative plausibility of these two values may be examined in terms of data from Caribbean stations. Table 5.2 lists the observed mean wind velocities for the period between April 15 and 24, 1979, and Table 5.3 lists the required eastward velocity for transport to Africa by April 23. Wind data are shown in Table 5.2 for the 50- and 70-mbar levels (20.7 and 18.6 km) which bound the altitude of the West African stratospheric cloud. Because the latitude of the cloud is no longer the same as that of St. Vincent, wind data for San Juan, Puerto Rico, have been added to those for Barbados and Trinidad. The strong latitudinal variation in the wind is clear and comparison of the values in Table 5.2 with those in Table 5.3 indicates that it is very unlikely that the cloud originated from the April 17 explosion. The hypothesis that it originated from the April 13 and 14 explosions is further substantiated by a detailed examination of the daily zonal wind behavior at Barbados and Trinidad. On April 15, 16, and 17, strong eastward winds (5 to 15 m/s) were observed at the 50- to 70-mbar level. On April 18, 19, and 20, the mean zonal wind was close to zero, preventing any systematic eastward drift of the cloud produced by the eruption of April 17. One further point may be noted. Figure 5.6(a) shows that, for the West African cloud, the lower altitude part of the cloud has moved farther, and, therefore, considerably faster, than the upper altitude part. This corresponds to the normally observed decrease of the eastward zonal wind with increasing altitude during this season in the lower stratosphere.

Although it has been deduced that the West African cloud originated at St. Vincent April 13 and 14, the problem of identifying the source of the other and larger cloud still remains. The SAGE events shown in Fig. 5.4(c) seem to indicate that the plume extending over the North Atlantic Ocean originated at the volcano on April 22, coincident with the final major explosion. This ignores the question of what happened to the cloud from the explosion of April 17, which produced the highest column of the series and which, as we have seen earlier, initially moved in a southerly direction.

TABLE 5.2: CARIBBEAN MEAN WIND VELOCITIES (APRIL 15 TO 24)

Station	Latitude	Altitude, km	Eastward velocity, m/s
Barbados and Trinidad (average)	12° N	18.6 20.7	3.5 3.9
San Juan	18.5° N	18.6 20.7	7.8 -2.0

TABLE 5.3: PARAMETERS OF STRATOSPHERIC CLOUD OVER WEST AFRICA

Height, km.	19.5
Mean latitude (average of measurements on April 23 and 24). .	16° N
Required eastward velocity if originating on April 13 or 14, m/s	7.4
Required eastward velocity if originating on April 17, m/s	12.1

In order to see if the North Atlantic plume could be related to this earlier eruption an analysis of the air movements at a pressure level of 50 mbar (20.7 km) has been carried out using rawinsonde data from Barbados and Trinidad. The starting point for the trajectory was 12° N 60° W at 0000 GMT on April 19, which is based on the lidar observations of the plume at this height, position, and time. Subsequent movements up to 1037 GMT on April 22, when the final major eruption occurred, are shown in Fig. 5.7. The total movement, then, from St. Vincent between April 17 and 22, is only a few degrees in longitude and latitude, placing it very close to the location of the SAGE observation of April 23. Furthermore, it is reasonable that the dispersion of the plume over this period would allow it to extend back to the volcano, thus overlapping any plume produced by the explosion of April 22. The SAGE observation of April 23, therefore, most likely pertains to the plume due to the eruption of April 17, but the proximity to the volcano and the prevailing winds make it impossible to rule out some contribution due to the eruption of April 22. Similar considerations apply to the observations made subsequently.

It appears that the clouds still in the vicinity of St. Vincent on April 22 and 23 commenced to move rapidly northeastward over the Atlantic Ocean. The explanation lies in the arrival of a new weather system into the area. During the period April 20 to 23, a strong low-pressure trough extended southward along the Atlantic coast of the United States into the Caribbean. In conjunction with a high-pressure area centered east of the Caribbean, this produced a movement to the northeast, the beginning of which is apparent in Fig. 5.7(a). Subsequent to April 23, the low-pressure region moved slowly northeast across the Atlantic and finally abated on April 28. It seems clear that the plume was moved by this system, and Fig. 5.7(b) depicts the meteorological situation at 70 mbar on April 26 when the plume was observed at approximately 30° N. The final date on which the plume was seen agrees with that on which the low-pressure region abated; the required speed of movement of about 8 m/s is typical for this altitude and latitude region.

Figure 5.4(c) indicates that the cloud extending northward over the Atlantic descended as it moved. This is in agreement with general deductions based on the 70-mbar temperature map for April 18 over this region. This map shows that air parcels traveling northward tended to warm up, a feature that remained true throughout the following week. This warming is almost certainly caused by adiabatic compression due to downward motion. Calculations have been carried out to determine the amount of descent expected, assuming that an air parcel follows an isentropic trajectory. These showed that a parcel at a height of 20 km and a latitude of 10° N would have been expected to descend between 1 and 2 km by the time it reached 40° N. This value is in agreement with the SAGE measurements given in Figs. 5.4(c) and 5.5.

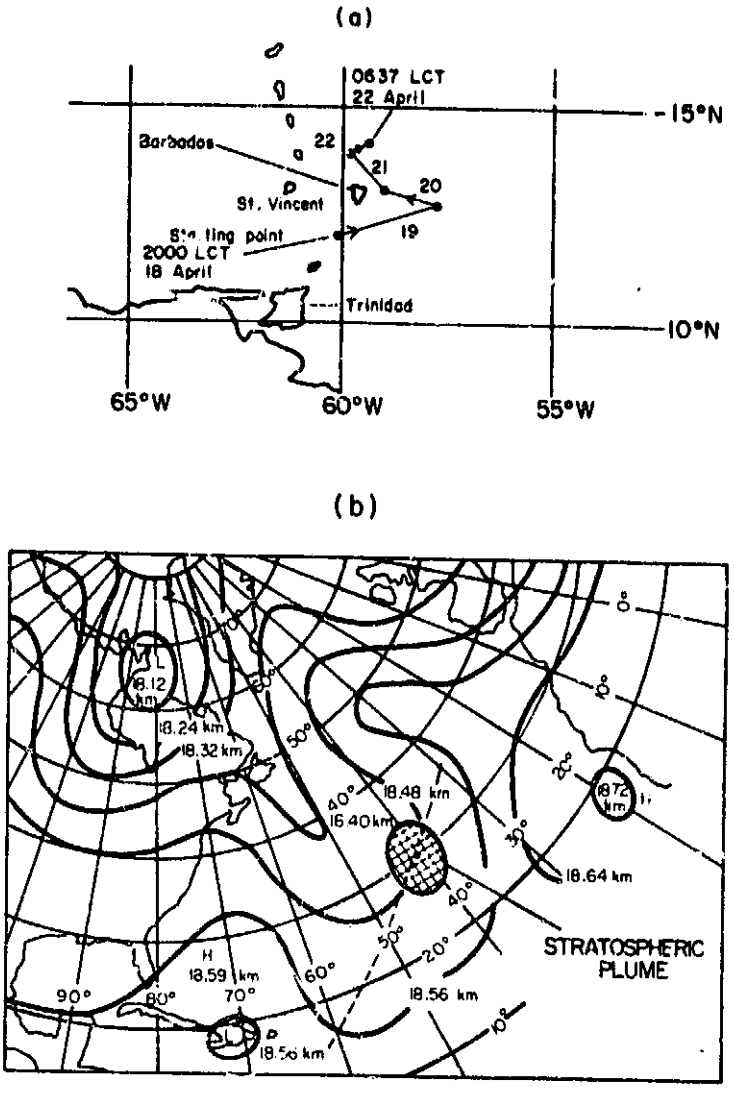

Figure 5.7 *(a) Calculated wind trajectory at 50-mbar pressure level (20.7 km) for the period April 19 and 22, 1979. Starting point for trajectory is based on lidar data of April 18.*
(b) High-altitude pressure map at 70-mbar at 1200 GMT on April 26, 1979. Crosshatched area shows position of stratospheric plume on this day; dashed line indicates trajectory of plume on preceding and following days.

In order to assess the observability of the volcanic clouds by SAGE the dispersion of the clouds must be estimated. A climatological analysis (McCormick et al, 1981) indicated that the clouds would have expanded to a size of 1000 km or more after a period of about 10 days, in agreement with estimates based on the SAGE data.

5.5 Mass Loading

It is possible to use the map in Fig. 5.4(c), in conjunction with the actual extinction values, to provide an estimate of the total mass of new stratospheric aerosol created by these volcanic eruptions. Such an estimate is subject to some error, as the geographical sampling by SAGE is somewhat coarse and, in order to convert the extinction values into a mass loading, a model for the aerosol particle size distribution and composition must be employed. As far as the geographical extent of the plume is concerned, it has been assumed that the extinction measured in each of the eight stratospheric events is representative of the aerosol spread over a rectangular area whose dimensions are given by the longitudinal separation of SAGE events and the latitudinal separation of SAGE tracks (approximately 24^{o} longitude by 5^{o} latitude).

An intermediate step in the calculation of the mass loading is the integrated extinction B_{aI} defined by the following equation:

$$B_{aI} = \sum_{\text{Plume}} A\left(\beta_{ah} - \beta_{anh}\right) \Delta h$$

where

β_{ah} = extinction due to aerosols at a height h in the plume

β_{anh} = normal background extinction due to aerosols at a height h

Δh = height interval (1 km in practice)

A = area of Earth's surface covered

The summation is carried out from the bottom to the top of the plume. The results of the calculations are shown in Table 5.4, where the West African and Caribbean-North Atlantic plumes have been listed separately. Only the events of April 23 and 24 are included in the values shown for the integrated extinction and mass loading for the Caribbean-North Atlantic plumes. This

TABLE 5.4: ATMOSPHERIC EXTINCTION AND STRATOSPHERIC AEROSOL MASS LOADING FROM SOUFRIÉRE, ST. VINCENT

	Area of Earth covered, km^2	Vertical thickness, km	Integrated extinction, km^2	Estimated mass loading, metric tons
West African plume	3.1×10^6	1.4	6.3×10^2	$0.52 \pm 0.2 \times 10^3$
Caribbean-North Atlantic plume	7.7×10^6	2.1	18.8×10^2	$1.6 \pm 0.6 \times 10^3$
Total	10.8×10^6	1.9	25.1×10^2	$2.1 \pm 0.7 \times 10^3$
Background global value	5.1×10^8	Stratosphere (tropopause + 2 km upwards)	6.1×10^5	$5.0 \pm 1.0 \times 10^5$

is because it is thought that the remainder of this plume emerged from, and contains some of, the same material that was seen on these two days. The value shown for the layer thickness is the width of a rectangle whose area is equal to that under the layer peak and whose length is fitted to the layer peak. As might be expected, the integrated extinction for the Caribbean-North Atlantic plume is greater than for the West African plume because the former contains the material injected into the stratosphere by the largest explosion of the series. (Also shown in Table 5.4 are corresponding values for the entire global stratospheric aerosol, estimated from SAGE global data.) It can be seen that, on a global scale, the Soufriére event was small, contributing less than 0.5 percent to the total integrated extinction. Conversion to mass loading has been made using the ratio $E/M = 1.22 \times 10^3$ m^2/kg as described in Section 4.1 resulting in the values shown in the final column of Table 5.4 Estimates of errors are shown in the table, which are based on a consideration of the errors in the actual measurement of the extinction, in sampling, in the estimates of the area of the Earth's surface covered, and in the extinction-to-mass conversion ratio. In addition, a small error may arise due to uncertainty of the composition of the newly injected or formed aerosol, which may contain a certain amount of fine ash with a considerably higher refractive index (Cadle et al, 1976).

6. STRATOSPHERIC EFFECTS OF THE ERUPTION OF SIERRA NEGRA

6.1 Introduction

The Sierra Negra volcano, in the Galapagos Islands (0.83° S, 91.17° W), erupted on November 13, 1979, producing an eruptive cloud large enough to be seen on NOAA's SMS-1 weather satellite. The cloud separated into two lobes moving SE and SW, respectively, at an altitude estimated, from infrared imagery, to be about 15 km. Although volcanic activity extended into December, no further eruptive clouds were detected (SEAN Bulletin 4, Nos. 11 and 12, 1979).

At the time of the November 13 eruption, SAGE was making observations in the southern hemisphere. The observations reached their most southerly point on November 22, 1979, and then moved north, passing over the latitude of the volcano on December 13, 1979. New stratospheric material was clearly visible north of latitude 15° S and the development and movement of this material was visible on the SAGE extinction profiles up to the time of the eruption of St. Helens (May 18, 1979). No lidar observations were made on the stratospheric effects of this volcano, using any of the NASA-Langley systems, although enhanced scattering was observed at Fukuoka, Japan, which was attributed to its effects (Fujiwara et al, 1982).

6.2 SAGE Observations

As the SAGE observation point moved northwards in December 1979, evidence of increased scattering that could definitely be attributed to the Sierra Negra eruption, was first obtained at a latitude of about 20° S. Examples of extinction profiles obtained during this northward movement are shown in Fig. 6.1. Fig. 6.1(a) shows a typical profile of the undisturbed stratospheric aerosol layer, Fig. 6.1(b) shows one taken in a region of volcanic enhancement. A clear volcanic layer at a height of 19 km is evident, with an extinction that is over one order of magnitude greater than the normal background level. Several such profiles were observed and their geographical distribution is discussed below. Fig. 6.1(c) shows the mean extinction profile for all observations taken within the latitude belt 0° to 10° S. The average is over both normal and volcanically enhanced layers and, unlike the single profile in Fig. 6.1(b), it has no clear maximum above the tropopause. This was a characteristic of all such mean profiles close to the equator at this time. Further away from the equator,

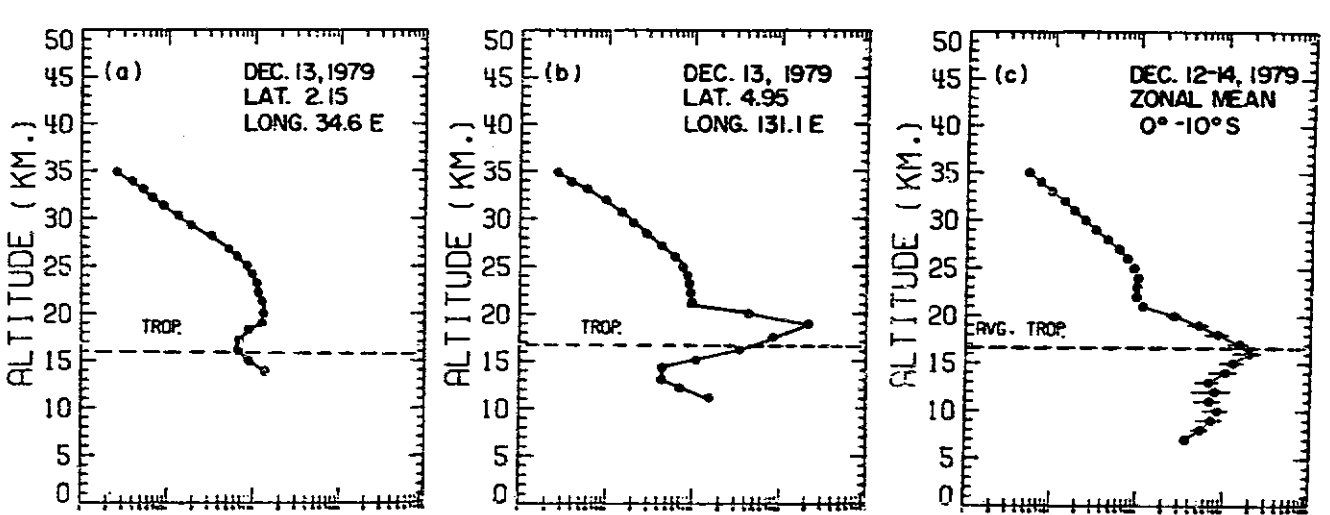

Figure 6.1 Examples of SAGE extinction profiles obtained at the time of the Sierra Negra eruption.

at this time, and on the equator at later times, the volcanic layer becomes more distinctly separated.

Fig. 6.2 shows global contour maps of the stratospheric optical depth before and after the Sierra Negra eruption. As in Section 4.2, the optical depth has been measured from 2 km above the tropopause (a model tropopause has been used) and is plotted for complete movements of SAGE from one extreme of latitude to the other. The map in Fig. 6.2(a) shows very clearly the typical nonvolcanic behavior, with optical depth minima occurring at latitudes of 25° to 30° and maxima lying between and outside these latitudes. Fig. 6.2(b) shows the corresponding posteruption contour map. The location of the SAGE observations moved north and passed over the latitude of Sierra Negra 30 days after main eruption. The data in the southern part of the map thus represent an earlier epoch relative to the time of the eruption than that shown in the northern section. The map clearly shows areas of enhanced extinction from the Sierra Negra eruption, with a strong concentration on the equator, close to the eruption site and a significant amount already moving toward the north. (The isolated point of large optical depth at 58° S, 162° W is believed to be associated with clouds close to, or penetrating, a high local tropopause.)

The data have been plotted in a different format in Fig. 6.3. This figure shows the zonal mean extinction for the same two periods as a function of height and latitude. That in Fig. 6.3(a) shows little detail but Fig. 6.3(b) shows very clearly the northward movement of the volcanically injected material. Fig. 6.4(a) and Fig. 6.4(b) show similar zonal mean extinction plots for the periods January 27 to March 6, 1980, and May 12 to June 20, 1980. The latter period is after the eruption of St. Helens, but sufficiently close so that its stratospheric effects were still confined to the western hemisphere. At this time the Sierra Negra effects were well distributed longitudinally and Fig. 6.4(b) shows the zonal mean extinction for the eastern hemisphere only. The main features by these figures are:

1. The movement of part of the material from the equatorial stratosphere to the high latitude stratosphere, the dominant movement being to to the north, but some material clearly moving to the south (but becoming disconnected from the main mass).

2. The existence of a reservoir of material over the equator even as late as June 1980 (seven months after the eruption) whose altitude gradually increased.

3. The material changing latitude tends, as a first approximation, to follow the tropopause altitude changes.

(a)

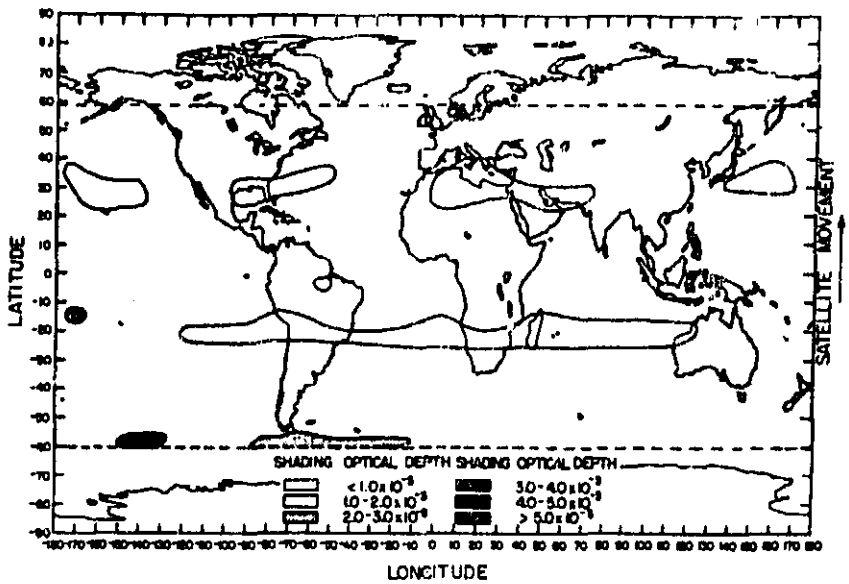

(b)

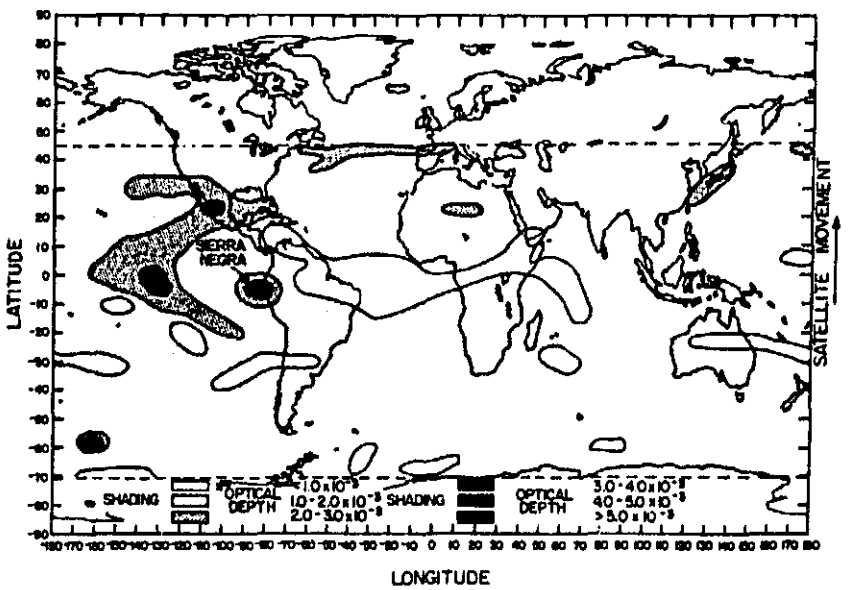

Figure 6.2 Maps showing the stratospheric optical depth, measured from two kilometers above the tropopause, as obtained by SAGE.

(a) September 15–October 21, 1979.

(b) November 22–December 30, 1979.

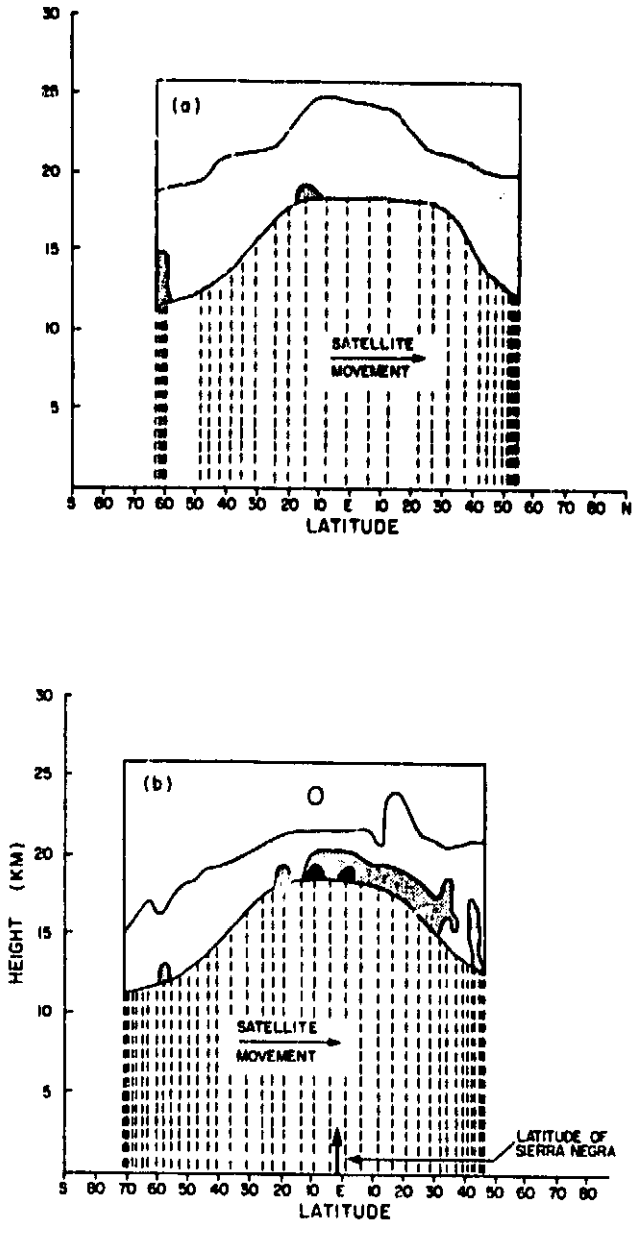

Figure 6.3 Zonal mean extinction obtained by SAGE.
(a) September 15–October 21, 1979.
(b) November 22–December 30, 1979.
Dashed lines show the mean latitude for each day's observations. The solid line at the base of the plotted extinction values shows a height two kilometers above the tropopause.
Code for shading:

SHADING	MEAN EXTINCTION
	$0-1 \times 10^{-4} KM^{-1}$
	$1-2 \times 10^{-4} KM^{-1}$
	$2-4 \times 10^{-4} KM^{-1}$
	$4-6 \times 10^{-4} KM^{-1}$
	$6-8 \times 10^{-4} KM^{-1}$
	$> 8 \times 10^{-4} KM^{-1}$

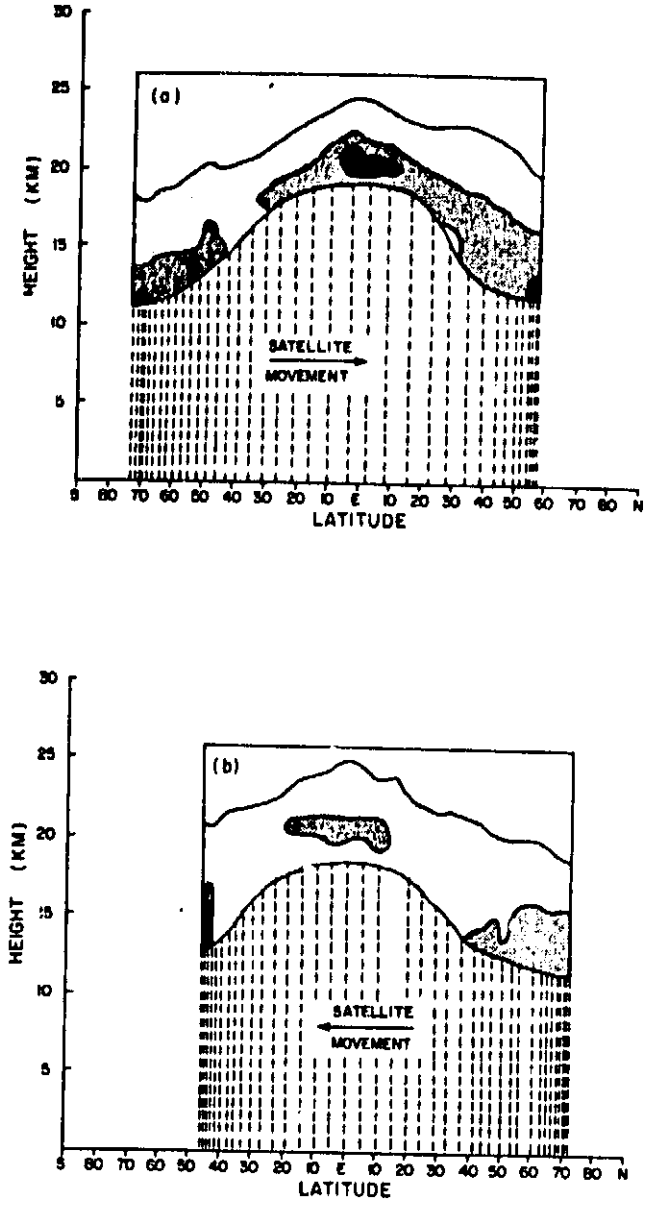

Figure 6.4 Zonal mean extinction obtained by SAGE.
(a) January 27–March 6, 1980.
(b) May 12–June 20, 1980 (Eastern Hemisphere only).
Dashed lines show the mean latitude for each day's observations. The solid line at the base of the plotted extinction values shows a height two kilometers above the tropopause.
Code for Shading:

SHADING	MEAN EXTINCTION
	$0-1\times10^{-4}$ KM^{-1}
	$1-2\times10^{-4}$ KM^{-1}
	$2-4\times10^{-4}$ KM^{-1}
	$4-6\times10^{-4}$ KM^{-1}
	$6-8\times10^{-4}$ KM^{-1}
	$>8\times10^{-4}$ KM^{-1}

In order to show more clearly the altitude changes in the peak (or apparent peak) of the injected material the data have been replotted in Fig. 6.5 in terms of aerosol/molecular extinction ratio, rather than aerosol extinction. This figure shows contour plots of the mean extinction ratio as a function of altitude and time for the four 10° latitude bands between the equator and 40° N. Fig. 6.5(a), for latitude band 0° to 10° N, shows the injection of material near the equator, its rapid initial increase in altitude and subsequent show rise. (Note the penetration by the tropopause of high altitude clouds.) Fig. 6.5(b) is essentially similar to Fig. 6.5(a) but Fig. 6.5(c) and Fig. 6.5(d) show that the material arrived at these latitudes reasonably well separated from the tropopause. It should be noted, however, that both Fig. 6.5(c) and Fig. 6.5(d) show the same gradual rise in peak altitude and that the separation of the peak from the tropopause increases with increasing latitude. Similar plots have been prepared for the southern hemisphere. These show the same features, although somewhat more weakly, because of the lower concentrations of injected material.

6.3 Interpretation and Discussion of Observed Dispersion

Mean zonal wind velocities on the equator, particularly at the 70 mb and 50 mb levels (approximately 18.5 and 20.5 km) are characteristically weak (Newell et al, 1972). Their typical order of magnitude--about 1 m sec^{-1}--implies a movement of about 90 km per day or about 3000 km in the 30 days between the date of eruption and the arrival of the SAGE observation point at the equator. This is of the same order of magnitude as the movements shown in Fig. 6.2(b), although the actual wind systems are likely to be dominated by the biennial oscillation and by irregular winds. Fig. 6.2(b) further shows that the meridional movement has been at least as great as the zonal movement on the equator and that, as expected, the zonal movement and dispersion at high latitudes has been greater than that at lower latitudes.

The mean meridional circulation across the equator in the lower stratosphere varies seasonally (Reiter, 1975) with a south-north movement occurring in December-February and a north-south movement occurring in June-August. The mean south-north movement in the northern winter agrees well with the movement of the new aerosol as shown in Fig. 6.3(b). The expected reverse movement in May-June 1980 is not immediately obvious in the data plots already shown but is, in fact, detectable and will be commented on in more detail in Section 6.4.

Trajectories for the movement of upper air parcels may be calculated by assuming that they move isentropically; that is, that they follow surfaces of constant potential temperature (Dutton, 1976). Potential temperature, defined as

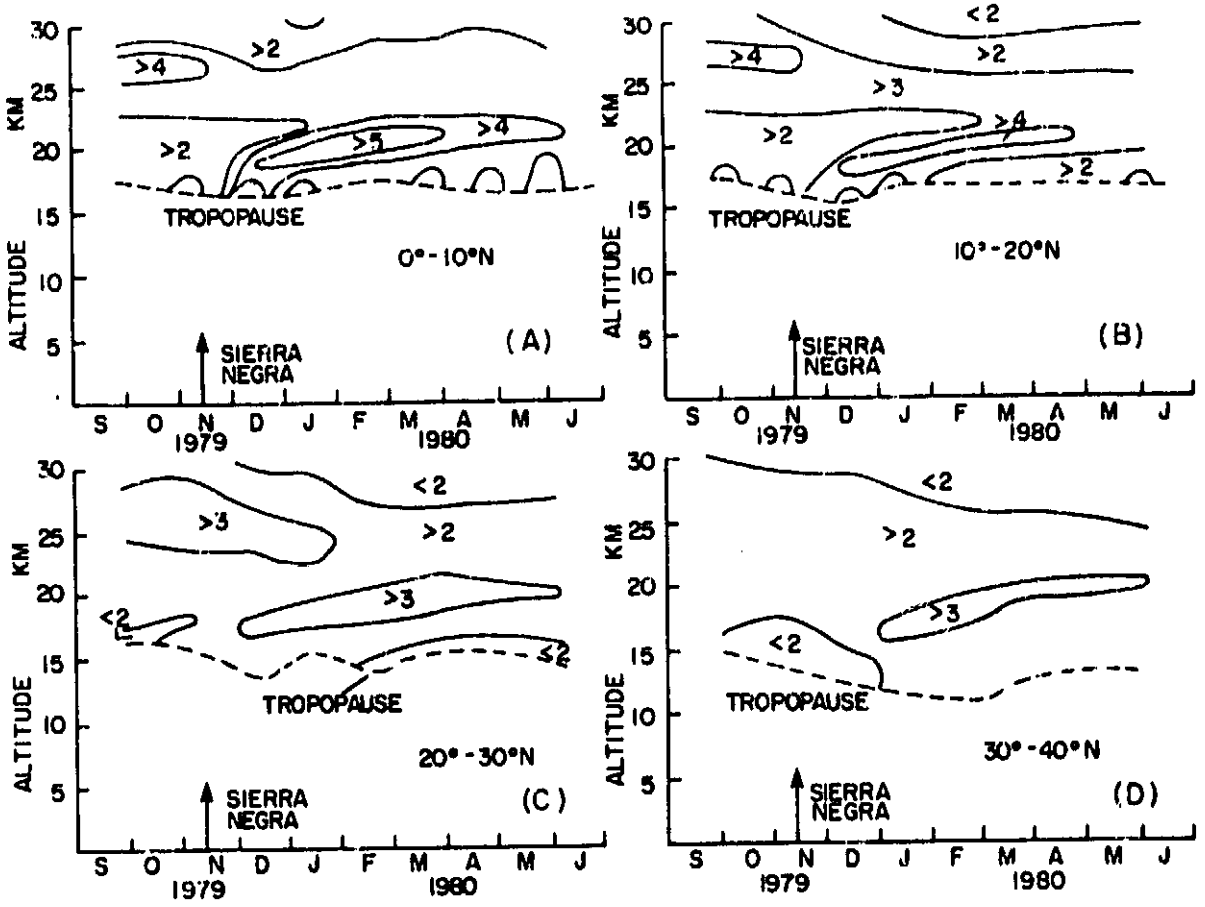

Figure 6.5 Contour plots of stratospheric extinction ratios before and after the eruption of Sierra Negra. The variation of the extinction ratio is shown as a function of altitude and time for four different Northern Hemisphere latitude belts.

$$\theta = T \left(\frac{1000}{p}\right)^{R/C_p}$$

where T is the thermodynamic temperature and p is the pressure in millibars, varies very considerably with both altitude and latitude. It is of interest to examine whether the stratospheric aerosol, for which the newly injected volcanic material serves as an excellent marker, follows isentropic surfaces.

In order to examine whether the material from Sierra Negra moved approximately isentropically when changing latitude, potential temperatures corresponding to the periods of satellite observation have been calculated using the NOAA meteorological data supplied for the times and locations of the measurements. The resulting contour plot for potential temperature in December 1979 is shown in Fig. 6.6(a). Superimposed on the potential temperature contours are the tropopause height and a shaded area showing the region of the volcanic layers defined in terms of the aerosol/molecular extinction ratio. An example of the way in which this layer is defined is shown in Fig. 6.6(b) where the extinction ratio for the prevolcanic period October 21 to November 21, 1979, has been plotted as well as for the post-volcanic period November 22 to December 21, 1979. The layer is defined as lying between the points where the difference between the curves is greater than half the difference at the peak of the volcanically enhanced layer (shaded area in Fig. 6.6(b)). It may be noted that, although the volcanic layer falls with increasing latitude, it lifts away from the tropopause. Although there is considerable irregularity, the layer of enhanced extinction follows quite closely the lines of constant potential temperature. Fig. 6.7 shows a second example, the potential temperature data being calculated for February 1980 and the SAGE data shown for the January 27 to March 6, 1980, sweep period. Although the layer has now moved up in altitude at all latitudes, it still lies reasonably closely to the constant potential temperature contours, particularly in the northern hemisphere.

Several explanations may be advanced for the height increase for the layer that is shown in Fig. 6.5. The first possibility is that it is produced over the equator by the mean Hadley cell circulation (Reiter, 1975). The increase at other latitudes is then produced by transport of the material outwards from the equatorial reservoir. This is plausibly supported by the fact that, as shown in Fig. 6.7, the layer is much thicker at high latitudes than it is at the equator, as would be expected if it contained material transported from the equator at different times. Using Reiter's plots of mean meridional mass circulation, it is possible to calculate a mean Hadley cell vertical velocity for the stratosphere over the equator. This varies from about 0.3 mm s^{-1} at a height of 16 km to zero at about 20 km. Over a period of 1 month the vertical movement would be less than, or equal to, about 0.8 km. This is in quite good agreement with the movements shown in Fig. 6.5, moreover the vertical movement slowed as the layer reached greater altitudes.

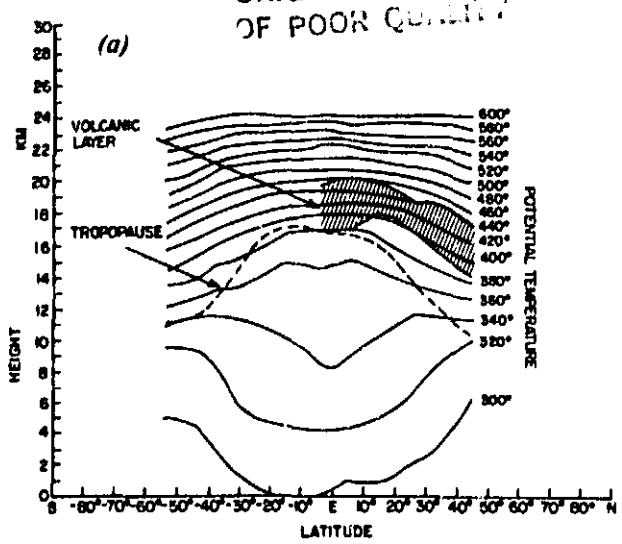

LATITUDE BAND 20° - 30°N

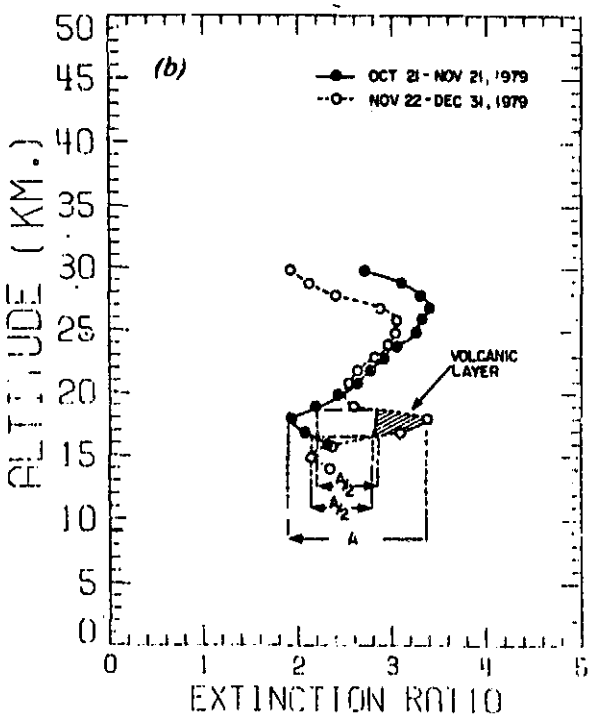

Figure 6.6 *(a) Potential temperature as a function of altitude and latitude for December 1979. Also shown in the figure are the positions of the tropopause and the new stratospheric volcanic layer produced by Sierra Negra.*

(b) Figure showing the manner in which the extent and position of the volcanic layer is defined.

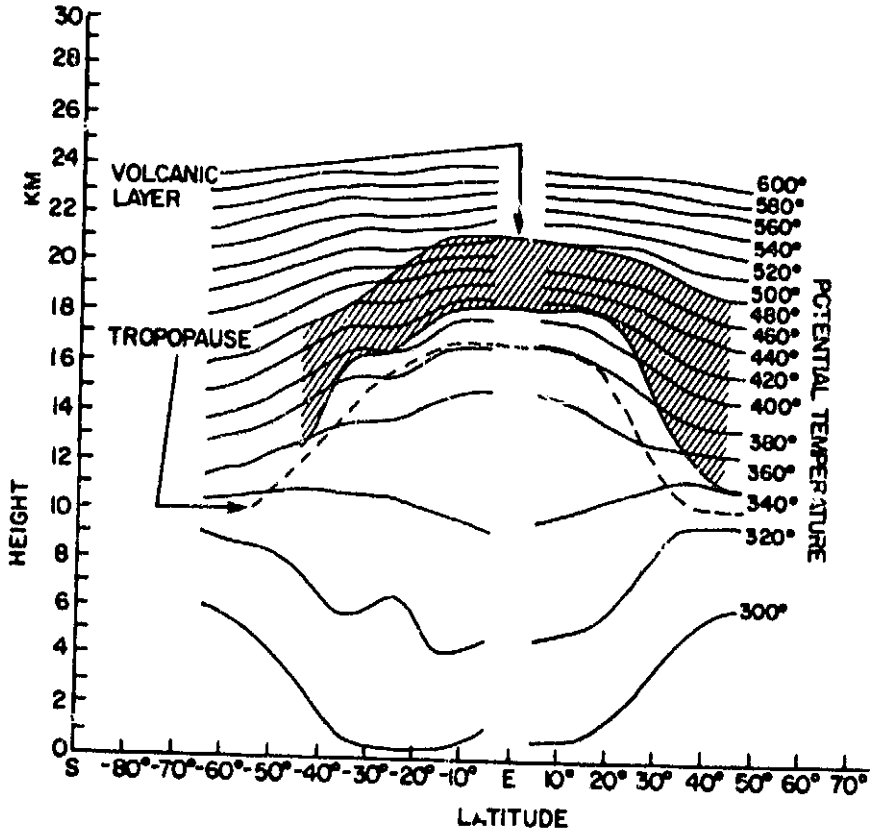

Figure 6.1 Potential temperature as a function of altitude and latitude for February 1980. Also shown in the figure are the position of the tropopause and the new stratospheric volcanic layer produced by Sierra Negra.

Hadley cell circulation is not the only explanation for the observed height increase. It is possible that fractionation occurred in the original volcanic plume, with the gaseous component rising higher. Initially, this would be invisible at a wavelength of 1 μm. Subsequent slow conversion to H_2SO_4 aerosol would give the impression of a rise in the layer height. A simpler explanation is that the apparent movement is simply a combination of vertical diffusion, causing the layer to expand, combined with sedimentation of the larger particles from the bottom of the layer into the tropopause where they are lost. Some cleansing of the bottom of the layer will also undoubtedly occur due to cloud action near the tropopause.

To distinguish between the above possibilities is not easy and careful modeling work is required on them and any other mechanisms to identify certain characteristics of each that might be sought for in the SAGE data.

6.4 Mass Loading Changes

In Section 4.2 a brief outline was given of the stratospheric aerosol mass loading changes associated with the Sierra Negra eruptions. Fig. 4.8 showed the time history for the mass loading in each hemisphere in which it could be seen that more new aerosol moved into the northern than the southern hemisphere. In order to continue discussion of the mass loading changes observed, it is convenient to divide the stratosphere into three regions: an equatorial zone between +20° and -20° latitude and a northern and a southern zone lying between the poles (SAGE data only extended to about ±70° latitude) and 20° latitude on either side of the equator. This division follows the manner in which the nonvolcanic aerosol appears to be divided globally and it enables one to discuss conveniently the way in which the eruptions of both Sierra Negra and Ulawun created equatorial reservoirs of stratospheric material (it also, fortuitously, divides the global surface into three almost exactly equal regions). Fig. 6.8(a) shows the way in which the stratospheric aerosol mean optical depth varied within each of these three global sectors from February 1979 to June 1980. (Data in June 1980 is plotted for the eastern hemisphere only because of contamination of the western hemisphere by material injected by Mount St. Helens.) Previous to the Sierra Negra eruption there is virtually no variation in the equatorial sectors whereas the other two sectors show a strong antiphase seasonal variation. In order to examine the increases in each sector due to Sierra Negra in more detail, the seasonal variation of the background aerosol in each sector has been modeled through to June 1980. In this modeling, it has been assumed that the equator shows no seasonal change and that the northern and southern sectors show equal antiphase variations. The modeled variations are shown as dashed lines on Fig. 6.8(a). Fig. 6.8(b) shows the optical depth for each sector with the modeled background variation removed. A right-hand ordinate has been added to the figure showing the approximate equivalent mass loading in each sector. The figure shows the following points:

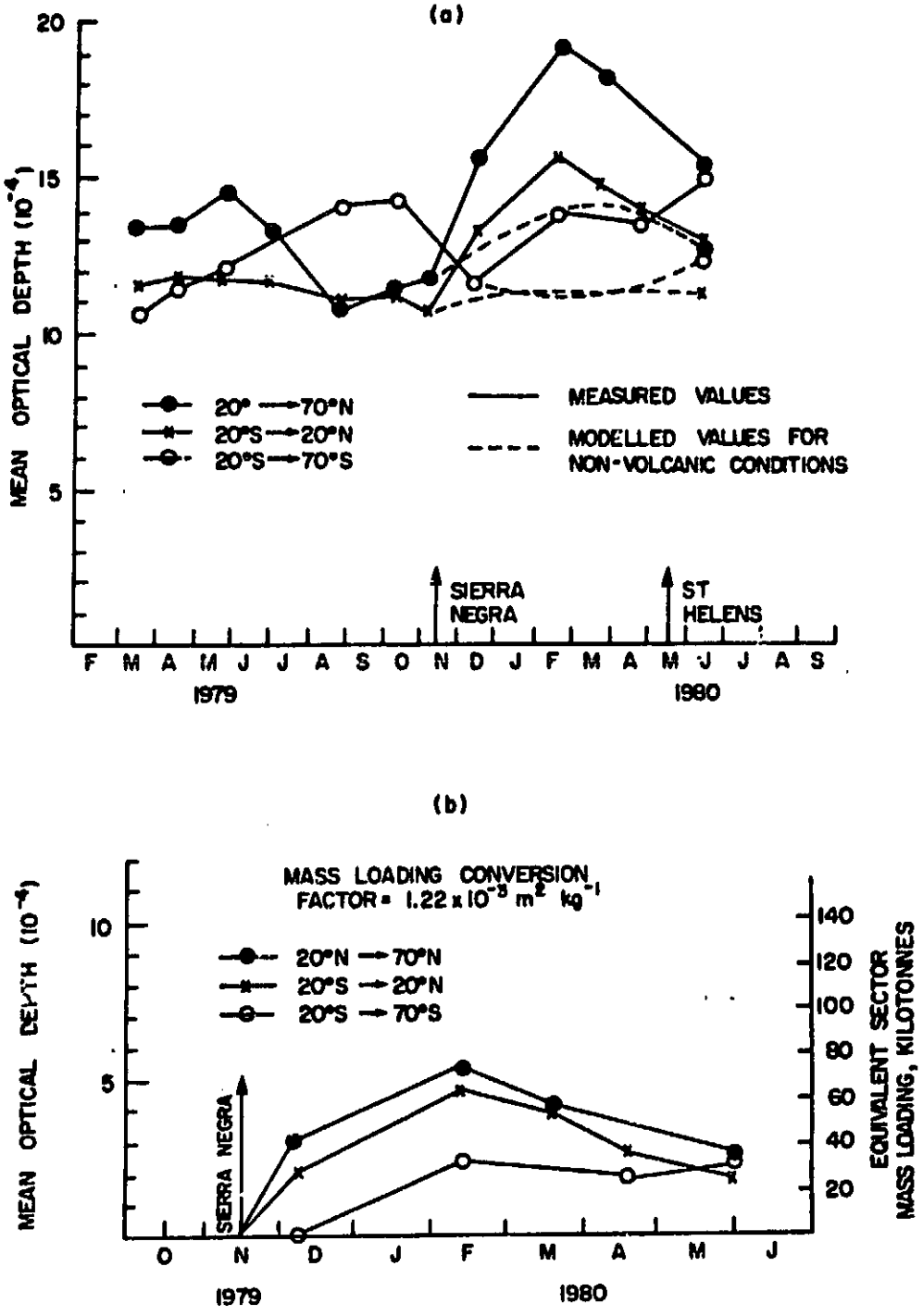

Figure 6.8 *(a) Mean stratospheric optical depth (from two kilometers above the tropopause), for three latitude zones, between February 1979 and June 1980.*

(b) Mean stratospheric optical depth increase produced by the eruption of Sierra Negra for the same latitude zones as shown in Figure 6.8(a). A scale showing the equivalent mass loading is drawn on the right-hand ordinate.

1. The equatorial and northern sectors reached their maximum optical depth about 3 months after the eruption following which, a slow decrease occurred. This decrease is more rapid for the equator than for the northern sector.

2. The southern sector mass loading did not start to become appreciable until after December 1979 and showed a significant increase in April-June, 1980, at a time when the other sectors were showing a mass decrease.

The slow rise to a maximum optical depth, which is shown more clearly in Fig. 6.9(a) for the total global mass loading by Sierra Negra is almost certainly associated with conversion of SO_2 gas to H_2SO_4 aerosols. As discussed in Section 2.2, estimates of the lifetime of SO_2 in the stratosphere are of the order of 25 to 100 days. In the case of this volcano, the equilibrium mass loading (production = loss) is reached after about 90 ±20 days. The decline following the initial rise is to be ascribed to various loss mechanisms such as sedimentation of the larger particles and stratospheric-tropospheric exchange, both near the tropopause free region and at other points where clouds penetrate the tropopause. The exponential decay time shown by he curve in Fig. 6.9 is about 5 months. This agrees quite well with the time of 7 months quoted by McCormick et al (1978) for the period immediately after the Fuego eruption on the basis of lidar measurements.

The different variation of the mass loading in the northern and southern sectors as shown in Fig. 6.8(b) is almost certainly related to the global circulation. As was commented on earlier, circulation across the equator in the stratosphere, at the solstices, is from the summer to winter hemisphere. This explains well the initial rapid movement of material into the northern sector. It also explains the behavior of the southern sector. In December very little flow is expected from the equator into the southern hemisphere but a considerable flow would be expected in May-June. This corresponds exactly to the variation of the mass loading in the southern sector which shows no change in November-December 1979, but a rather surprising increase in May-June of 1980, when the levels in the other sectors are decreasing.

Fig. 6.9(b) shows the ratio of the total volcanic mass loading outside the equatorial sector to that within the equatorial sector. It, thus, provides an indication of the rate at which the material is dispersing latitudinally and of the sense in which we still have an equatorial reservoir. It may be noted that there is an initial rapid increase in the ratio followed by a further slow rise towards the value for the background prevolcanic level. Based on the diagram, it may be stated that the material was well distributed globally after about 6 months.

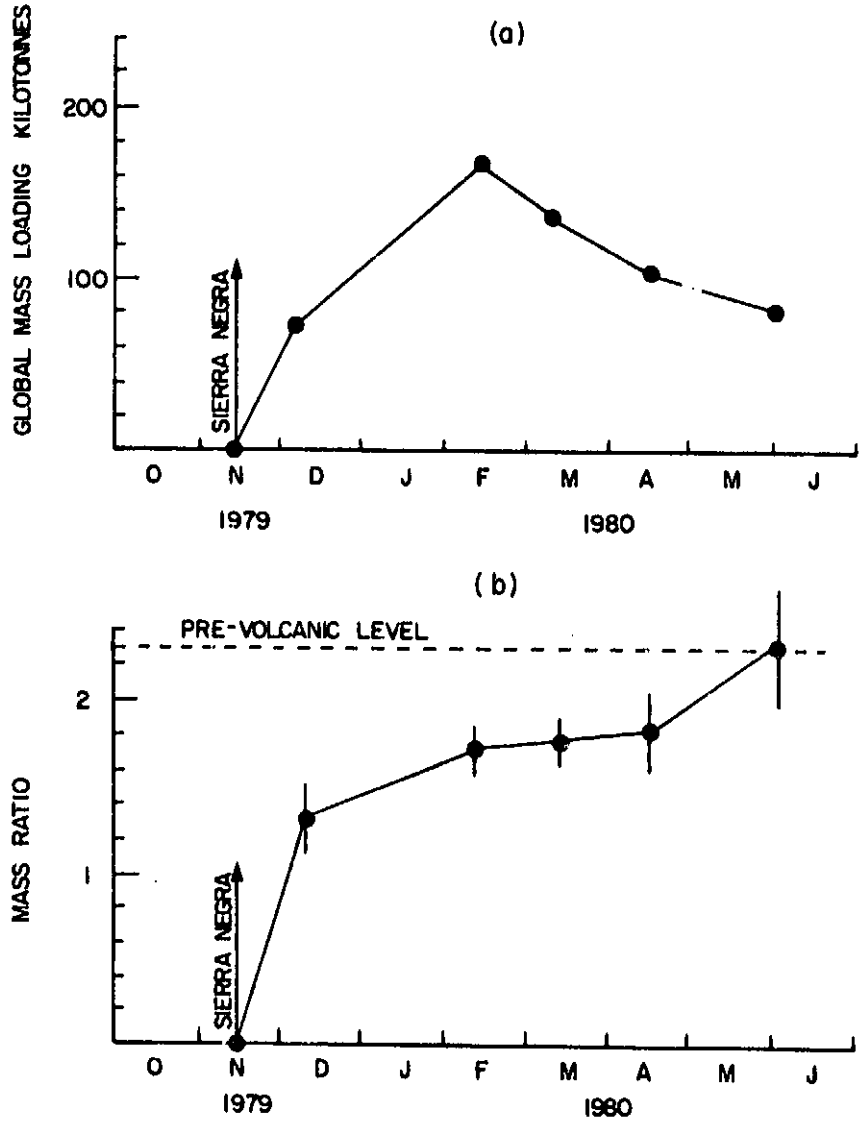

Figure 6.9 *(a) Time variation of the total stratospheric mass loading increase produced by the eruption of Sierra Negra.*

(b) The ratio (aerosol loading increase polewards of 20°S and 20°N)/(aerosol loading increase between 20°S and 20°N) plotted as a function of time between November 1979 and June 1980.

7. STRATOSPHERIC EFFECTS OF THE ERUPTION OF ST. HELENS

7.1 Introduction (Newell and Deepak, 1982; *Science 211*, 815-838, 1981)

Mount St. Helens erupted on May 18, 1980, sending material to a height estimated, by radar, to be greater than 24 km. This eruption lasted about 9 hours, the column height averaging about 16 km. Several smaller eruptions occurred during the following 6 months, but, although several of them penetrated the tropopause, their durations were all to be measured in minutes, rather than hours, and the maximum observed height for these eruptions was about 15 km. It is thought that these later eruptions will have produced local stratospheric affects but had little impact, on a global scale, compared to that of the May 18 eruption. The location of Mount St. Helens within the USA has meant that there was a concentration of scientific effort to study its eruptions which has not been equalled for any other volcano. Consequently, there are measurements of its effluents made from the ground, from in situ aircraft and from space, enabling a detailed picture of the eruption to be constructed.

Prevailing westerly winds on May 18 swept the lower sections of the plume (0 → 15 km) rapidly to the east and out over the Atlantic Ocean. That portion between 12 and 15 km circled the globe in about 15 days. The upper section of the plume (18 → 25 km) drifted slowly westward and out over the Pacific Ocean, circling the globe westward in about 60 days. At altitudes between 15 and 18 km the motion was exceedingly complex, lying initially over the western USA and Canada.

Estimates of the total mass of volcanic material injected into the atmosphere are approximately 2.4×10^8 tonnes. Most of this mass settled rapidly from the troposphere. In situ sampling of the stratospheric plume 3 months after the eruption suggested that the residual aerosol mass in the stratosphere was then about 2.5×10^5 tonnes. Samples taken at various times after the eruption showed a mixture of ash and sulfuric acid with highly variable ratios.

At the time of the May 18 eruption, SAGE was making measurements over high northern latitudes and moving south. It was thus ideally situated to view the stratospheric cloud produced by the volcano and the observation point passed over the latitude of St. Helens on May 25. It returned to the same latitude in early August when considerable dispersion of the stratospheric material had taken place.

Lidar measurements made at NASA-Langley a few days after the May 18 eruption, observed the lower stratospheric plume passing overhead. In addition, an airborne mission was mounted on May 21 to observe the extent of this plume. Observations continued to be made at NASA-Langley (and at other lidar stations around the globe) and several more airborne missions were flown under the plume during the months following the eruption.

7.2 SAGE Measurements (Kent, 1980)

At the time of the May 18 eruption SAGE was making measurements at latitude 62° N. The observation point moved south during the succeeding days and SAGE first obtained evidence of a significant volcanic enhancement on May 22 at 54°, 101° W. During the following days, as it passed over the latitude of Mt. St. Helens and moved south very large extinction values were recorded over and near the North American continent. An example of such extinction profile is shown in Fig. 7.1 in comparison with a normal profile. Such volcanic layers were observed at all altitudes up to 23 km. At this stage, only a few days after the eruption, relatively little dispersion had occurred and a contour map of the stratopsheric optical depth (from the tropopause + 2 km) is shown in Fig. 7.2. In this figure there are two very clear areas of volcanic enhancement corresponding to the two stratospheric air streams described in Section 7.1. The lower level plume, at an altitude of about 16 km has moved eastward over the Atlantic Ocean. The upper level plume, at an altitude of about 23 km, has moved more slowly westward over the Pacific coastline. The equivalent zonal extinction plot is shown in Fig. 7.3. There is a long thin column of material at about 50° N reaching up to 23 km; the regions of enhanced extinction close to the tropopause at lower latitudes correspond to the plume over the Atlantic Ocean.

On its return north in July 1980, SAGE entered a fully sunlit period and no observations were possible. The next observation of the volcanic cloud was then not taken until August 1980. A map of the optical depth and zonal extinction are shown in Figs. 7.4 and 7.5. A very considerable amount of dispersion has taken place, coupled with an increase in the mean optical depth. The new aerosol appears to have moved towards the north, although it should be noted that if an equivalent movement south had taken place in the same altitude range (12 → 18 km), much of the material would have entered the tropopause and become lost. In spite of the complete zonal dispersion, the stratospheric material still shows a great deal of inhomogeniety on a continental scale. The material at the upper levels (21 - 23 km) has moved southward rather than northwards, lying mainly in the latitude band 20° to 40° N. Some parts of this cloud have retained their coherence, such as that mass appearing on Fig. 7.4 at 33° N, 110° E which represents the most intense concentration of material at an altitude of 23 km. The smaller mass at 28° N, 34° E is also at the same altitude. Similar plots to those shown for May and August 1980 have been prepared for successive SAGE sweeps up to the time of eruption of Ulawun, showing the development of the St. Helens stratospheric material. The main features of these plots are as follows.

1. The injected material remained at high northern latitudes at least up to October 1980, when small amounts crossed the equator.

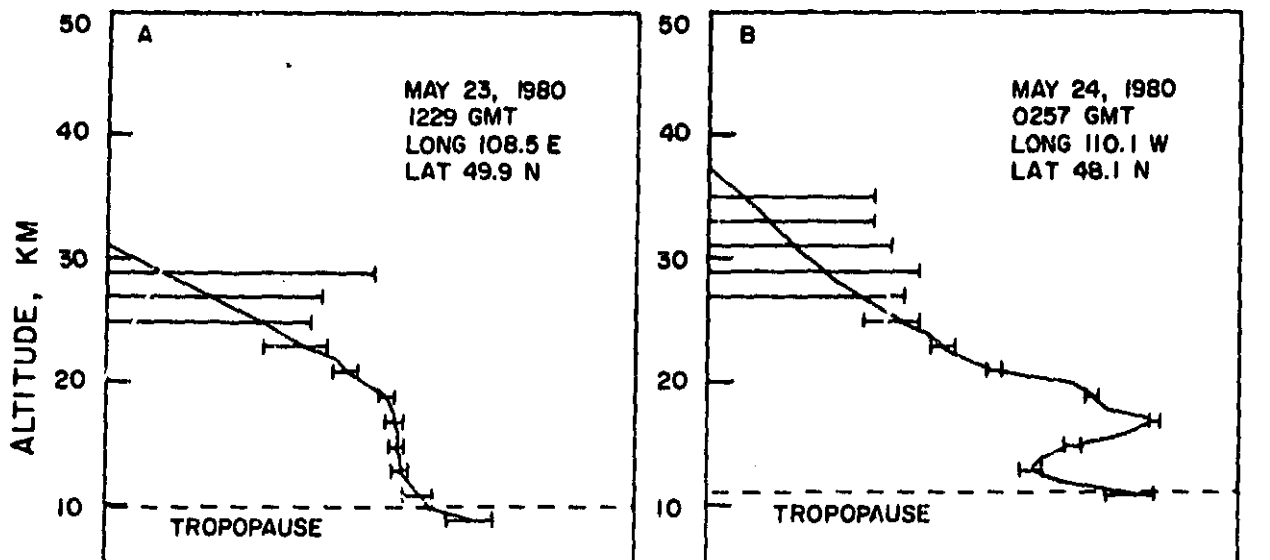

Figure 7.1 Stratospheric aerosol extinction profiles obtained by SAGE at a wavelength of 1 μm.
(a) Normal profile unaffected by volcanic effluents.
(b) Profile showing an enhancement caused by Mount St. Helens of about a factor of 10 near the layer peak.

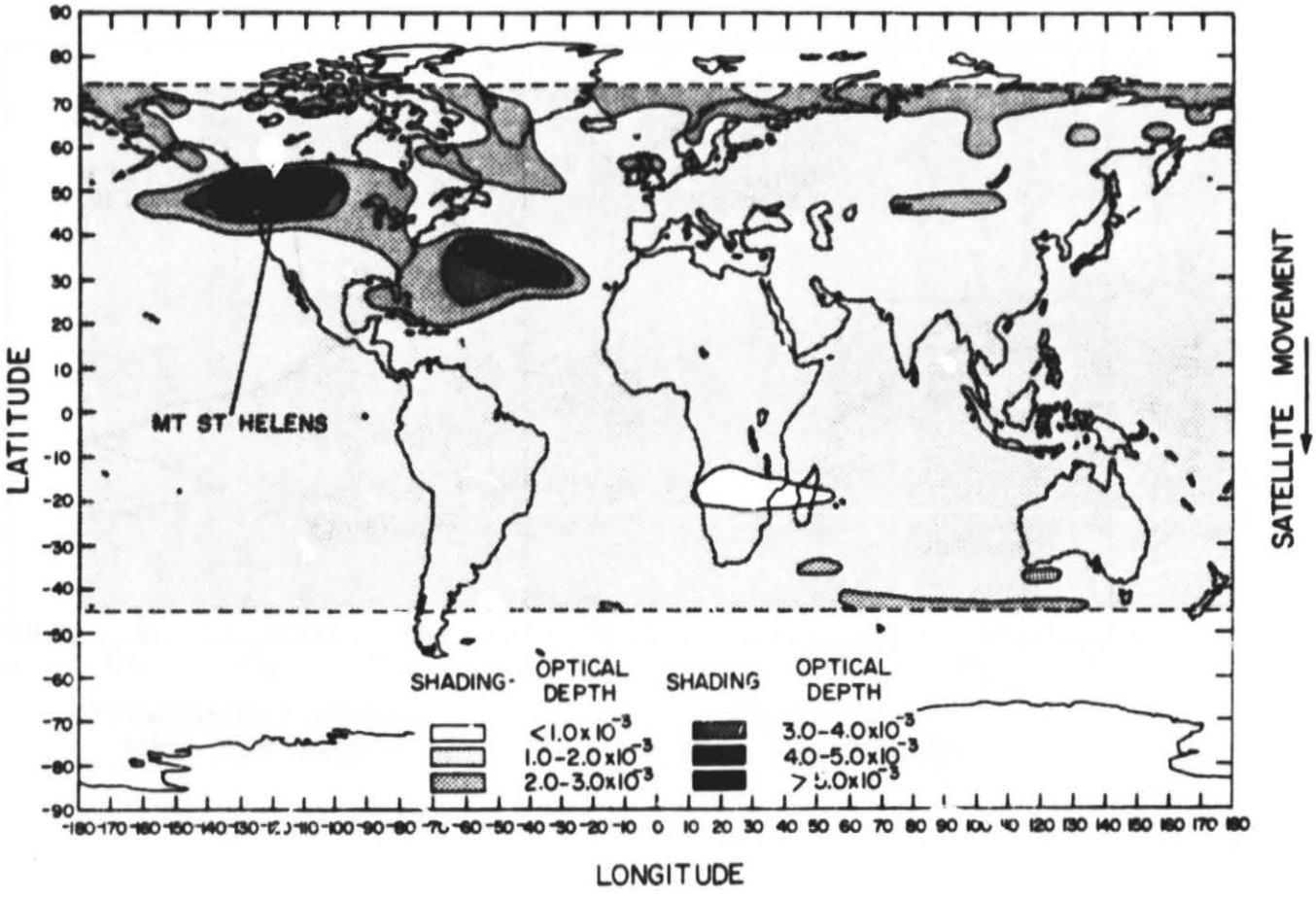

Figure 7.2 Map showing the stratospheric optical depth, measured from two kilometers above the tropopause, as obtained by SAGE for the period May 12–June 20, 1980.

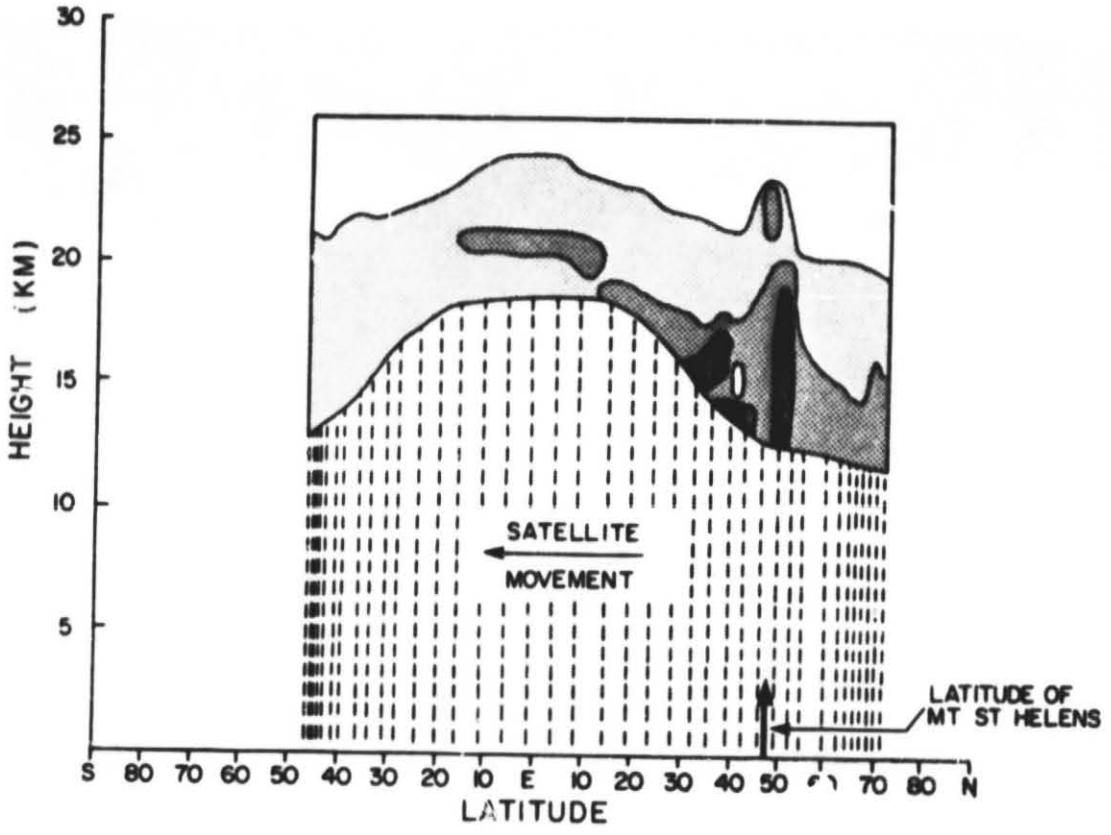

Figure 7.3 Zonal mean extinction obtained by SAGE for the period May 12–June 20, 1980. Dashed lines show the mean latitude for each day's observtions. The solid line at the base of the plotted extinction values shows a height two kilometers above the tropopause.
Code for shading:

SHADING	MEAN EXTINCTION
	$0-1 \times 10^{-4} KM^{-1}$
	$1-2 \times 10^{-4} KM^{-1}$
	$2-4 \times 10^{-4} KM^{-1}$
	$4-6 \times 10^{-4} KM^{-1}$
	$6-8 \times 10^{-4} KM^{-1}$
	$> 8 \times 10^{-4} KM^{-1}$

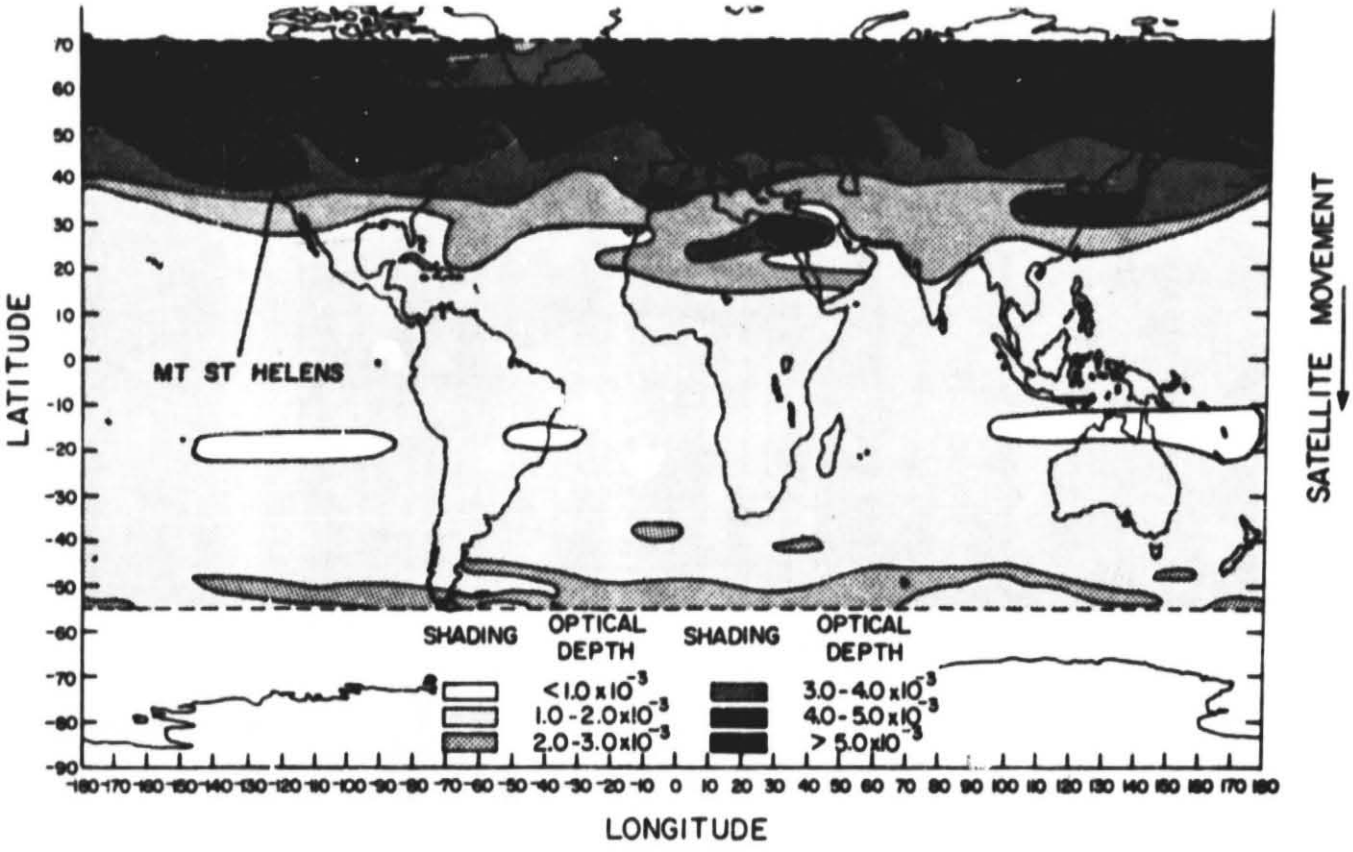

Figure 7.4 Map showing the stratospheric optical depth, measured from two kilometers above the tropopause, as obtained by SAGE, for the period July 21–August 26, 1980.

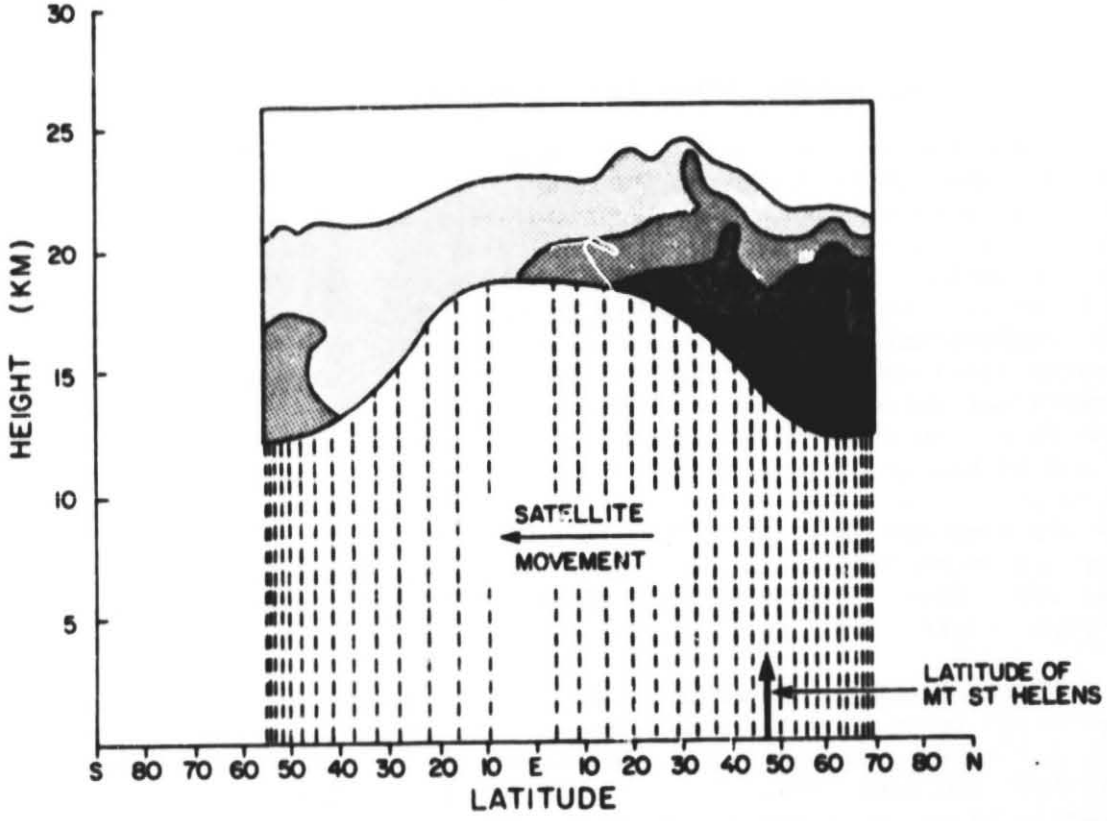

Figure 7.5 Zonal mean extinction obtained by SAGE for the period July 21–August 26, 1980. Dashed lines show the mean latitude for each day's observations. The solid line at the base of the plotted extinction values shows a height two kilometers above the tropopause.
Code for shading:

SHADING	MEAN EXTINCTION
	$0-1 \times 10^{-4}$ KM^{-1}
	$1-2 \times 10^{-4}$ KM^{-1}
	$2-4 \times 10^{-4}$ KM^{-1}
	$4-6 \times 10^{-4}$ KM^{-1}
	$6-8 \times 10^{-4}$ KM^{-1}
	$> 8 \times 10^{-4}$ KM^{-1}

2. The magnitude of the zonal and meridional inhomogenities gradually decreased with the material becoming stratified horizontally and latitudinally.

3. The equivalent mass loading (see Fig. 4.8) increased from May to August 1980, and then remained approximately constant until October 1980. The following map for November-December 1980 showed a slight decrease between latitudes 40° and 50° N, but unfortunately the observations did not extend further north than 48° N.

7.3 Lidar Observations (Kent, 1981; McCormick, 1982)

Lidar measurements were taken with the ground-based system at NASA-Langley immediately following the eruption of May 18, 1980. New stratospheric layers were first observed at altitudes less than 20 km on June 4. An example of a profile taken on the following day is shown in Fig. 7.6 together with an earlier nonvolcanic profile. The profile in Fig. 7.6(b) is typical of those observed for new volcanic material with sharp, thin layers of high peak backscatter ratio. The LaRC airborne lidar system was also flown on several missions over the eastern USA and Canada between May 21 and 28. Peak backscatter ratios as high as 100 were recorded on one flight south of Lake Erie. On these flights material was seen at various heights between 12 and 16 km, the layers at the greater altitudes being observed further south in general. One of the most striking factors of these observations was the vertical shearing of the layers. On the flight of May 27 near the coast of South Carolina a thin layer with a thickness of about 0.5 km was observed. Over a flight path of about 400 km this layer was found to descend smoothly from an altitude of 16.0 km to 13.5 km.

Observations continued at NASA-Langley and several more airborne missions were flown to observe the development of the new layers (see Table 3.2). Fig. 7.7 shows a succession of further profiles from NASA-Langley between July 1980 and June 1981. That of July 14, 1980, shows the merging of the separate layers to a rather jagged single profile. Fig. 7.7(b) shows a new layer at a height of 21 km (this was first seen on July 25). By November (Fig. 7.7(c)) a great deal of smoothing had taken place in the scattering profile and layering is no longer evident. The final figure for June 11, 1981, does indeed have material from Mount St. Helens still present but shows the layering characteristic of a new eruption. The material is believed to have come from the eruption of Alaid on April 27, 1981.

One of the more interesting missions flown by the airborne system was that to Frobisher Bay on December 9-15, 1980. A map of the flight path is shown in Fig. 7.8. On comparison with Fig. 7.5, it can be seen that this flight is to a region where there was a strong concentration of stratospheric aerosol at altitudes below 20 km. Examples of two-color lidar profiles taken are shown in Fig. 7.9. The layer is smooth at both locations and the increase in

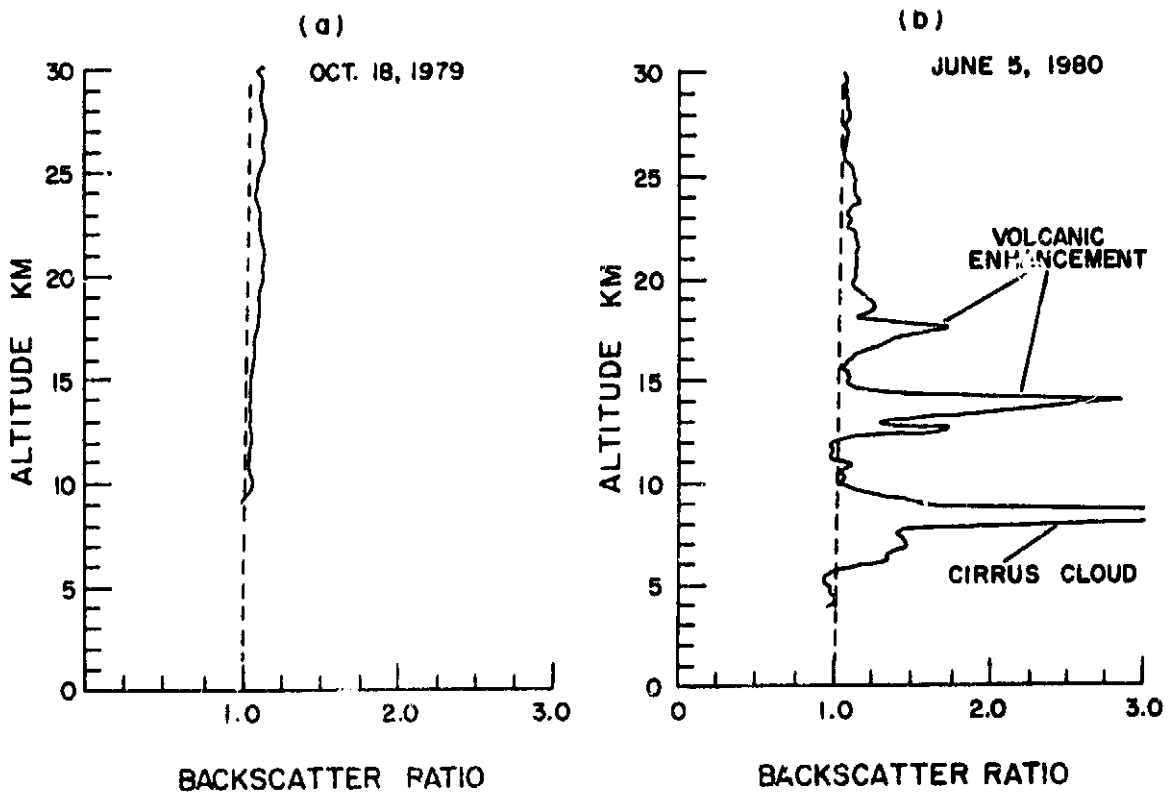

Figure 7.6 Lidar profiles obtained at NASA-Langley, Hampton, Virginia, before and after the eruption of Mount St. Helens.

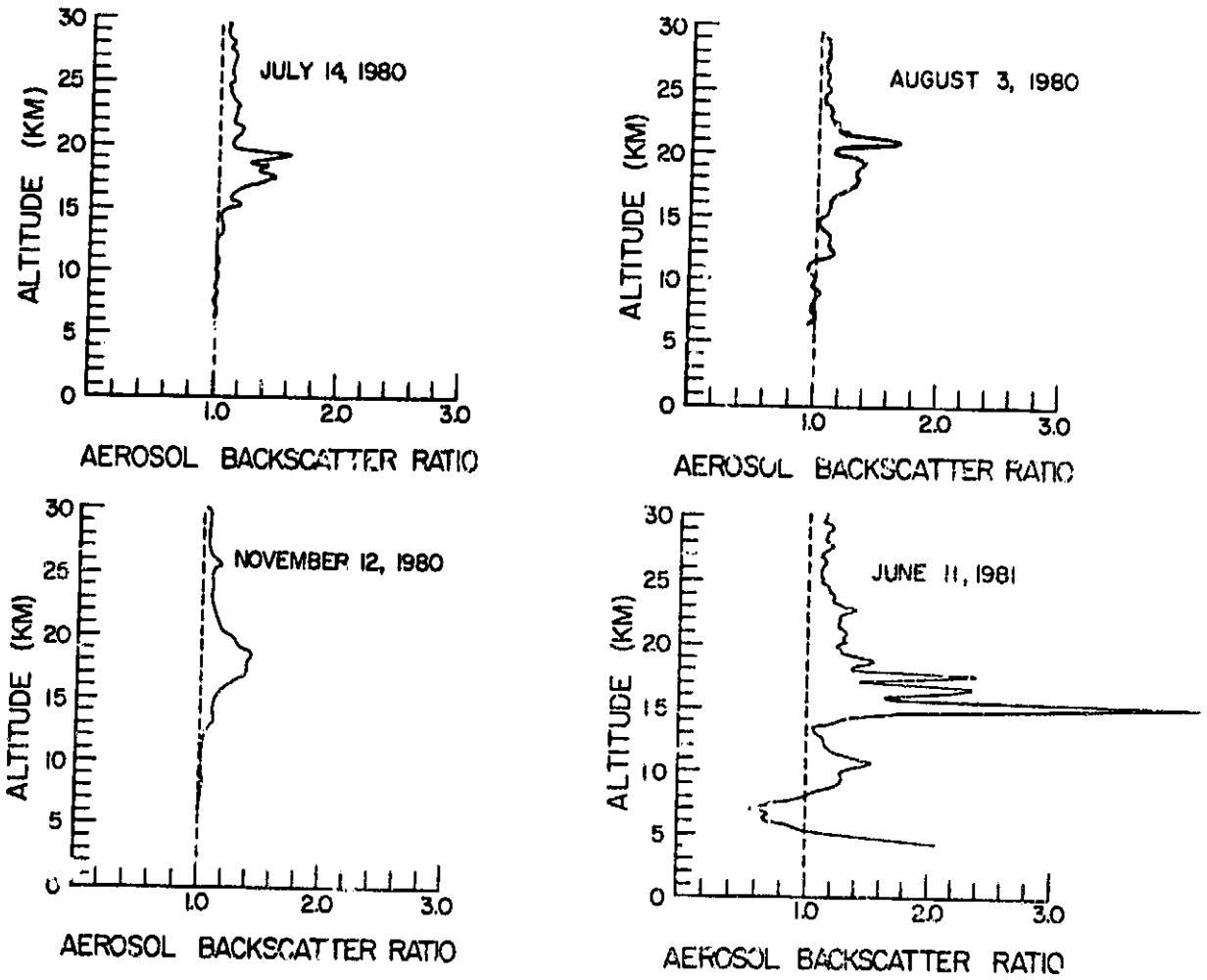

Figure 7.7 Lidar profiles obtained at NASA-Langley, Hampton, Virginia, between July 1980 and June 1981.

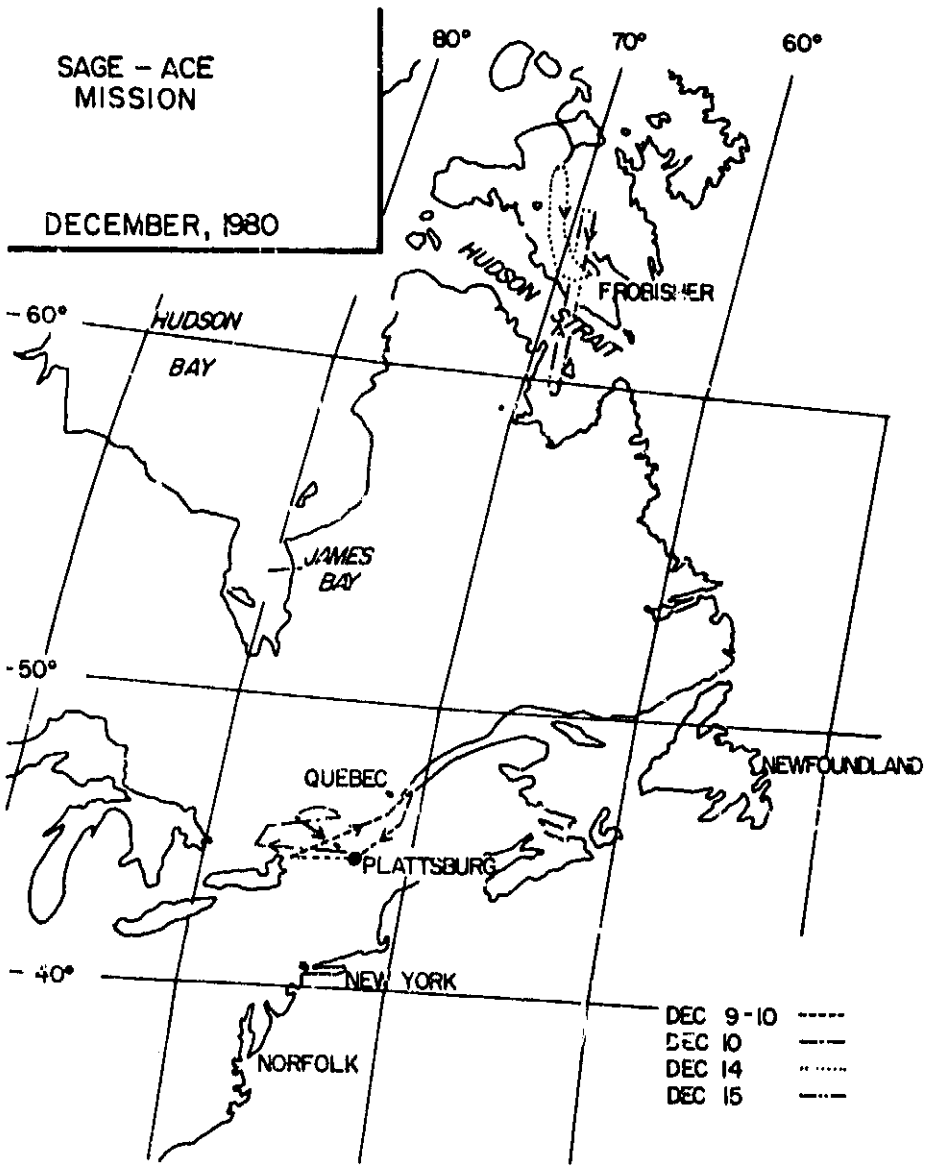

Figure 7.8 Flight path for the airborne lidar system in December 1980.

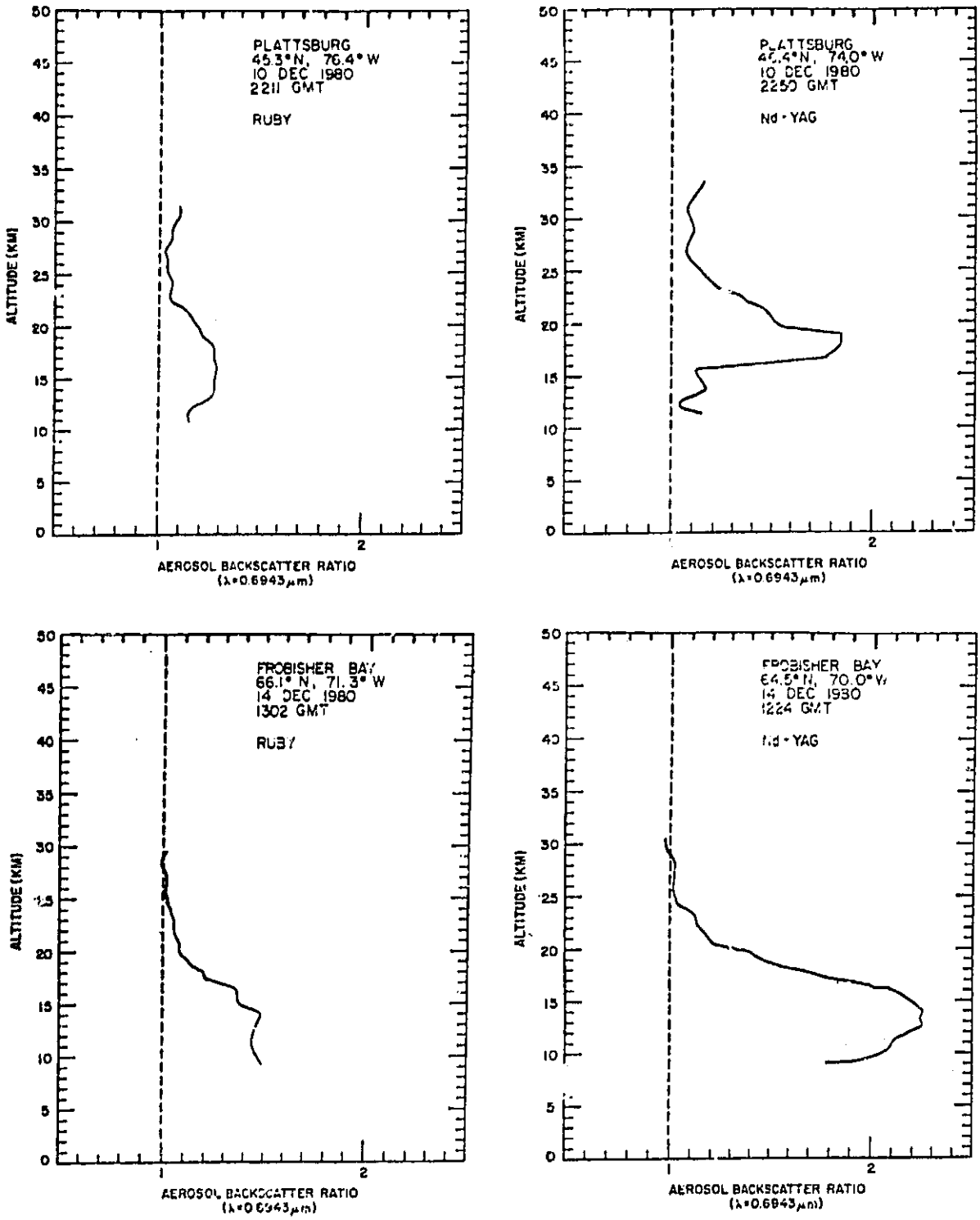

Figure 7.9 Two-color airborne lidar profiles taken in December 1980 during trhe flight to Frobisher Bay.
(a) Taken near Plattsburgh, New York State.
(b) Taken near Frobisher Bay.

intensity between Plattsburg (46° N) and Frobisher Bay (65° N) is evident. The backscatter ratio for the Nd:YAG wavelength is greater at all altitudes, than that for the ruby wavelength. This is as theoretically expected, model calculations for the H_2SO_4/H_2O aerosol predict a ratio of about 2.5 → 3 for scattering at the two wavelengths. This is in good agreement with values at the layer maxima in these two figures. There is, in addition, some variation with altitude below the maximum, where the Nd:YAG backscatter falls more rapidly than the ruby backscatter. This may be caused by a change in size distribution or refractive index and has not thus far been examined in detail.

Lidar measurements on the St. Helens stratospheric effects have been made at many stations in other parts of the USA and in Europe and Japan. These clearly show the arrival of the material in its passage round the globe and will be described in the next section on dispersion.

7.4 Dispersion of the New Stratospheric Material

The two most significant features of the dispersion of the new stratospheric material from St. Helens are:

1. its separation into two major plumes, traveling in opposite directions around the globe, and

2. the movement of the majority of the material northward, to be retained at latitudes north of 40° N.

The global movement of the plume is most easily seen by the appearance of scattering layers over the worldwide network of lidar stations in the northern hemisphere. Newell et al's (1972) tables for mean summer zonal wind velocity have been used to predict the expected global circuit times for various levels and heights in the atmosphere. The results of these predictions are shown in Fig. 7.10, where it can be seen that material at a height of about 13 km may be expected to orbit the Earth in about 18 days. In contrast, the westward moving material above 20 km will be expected to take three to four times as long. Published lidar data on the times of arrival of stratospheric layers has been used to construct Figs. 7.11 and 7.12 (Hirono et al, 1982; Iwasaka and Hayashida, 1980; D'Altoni and Visconti, 1981; Reiter et al, 1980; Hauchecorne et al, 1980; Thomas et al, 1981; Gardner et al, 1980; Eloranta 1980; DeLuisi et al, 1980). In addition the dates of observation by SAGE of high altitude layers, have been added to Fig. 7.12. These figures also show the predicted movement from Newell et al's tables (dashed line in Fig. 7.11, shaded area in Fig. 7.12). In Fig. 7.12, it has also been possible to distinguish between the arrival of material at 20 to 22 km and at 22 to 24 km. Similarly, in Fig. 7.11, distinction has been made, where possible, between the times of arrival of material at 12, 13 to 14 and 15 km.

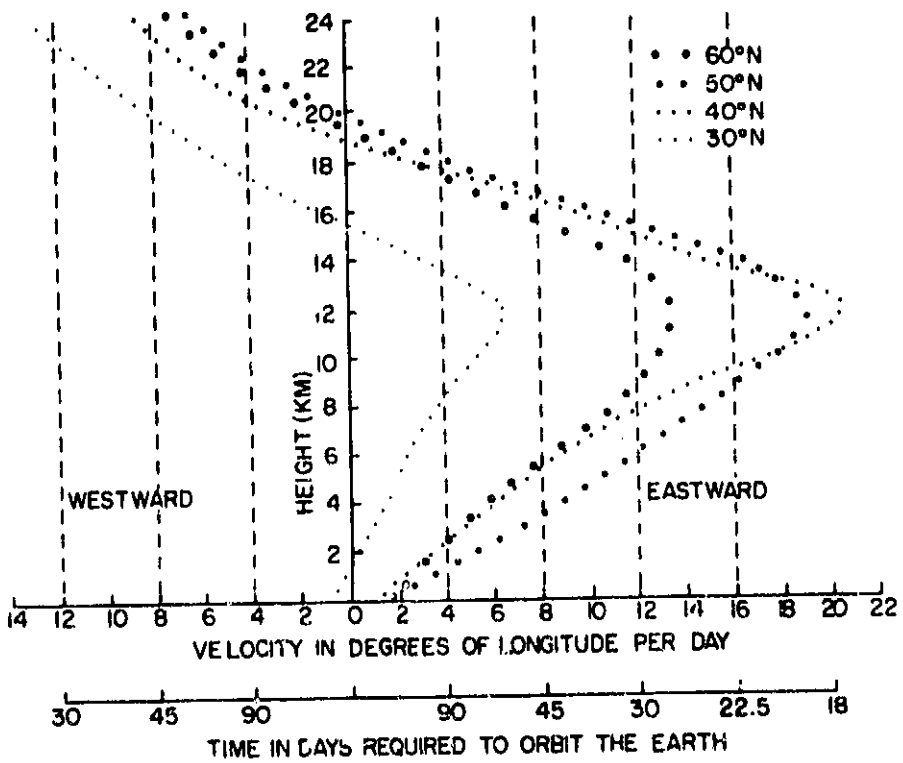

Figure 7.10 Mean zonal wind velocity in summer plotted as a function of height and latitude (Newell et al., 1972).

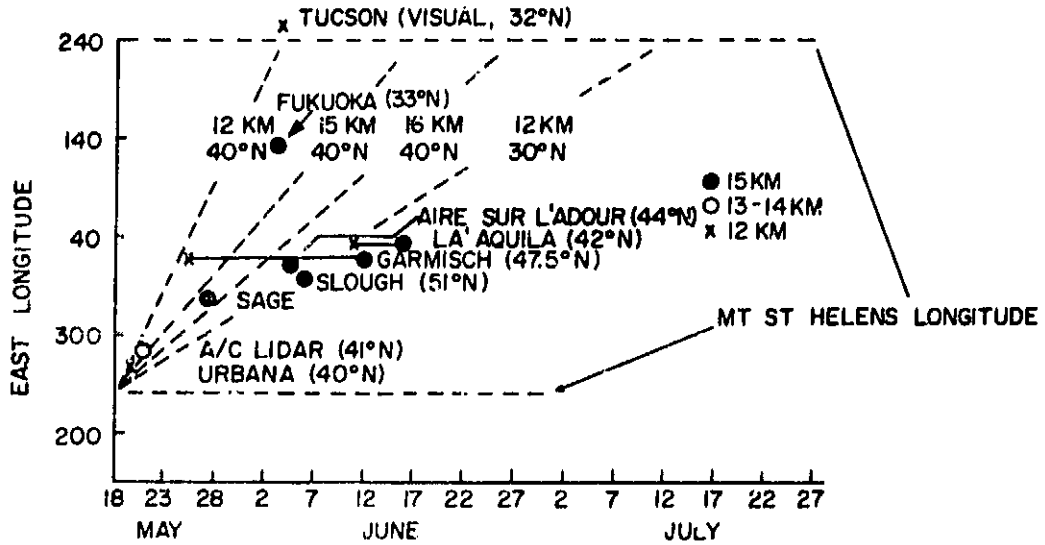

Figure 7.11 Times of arrival of aerosol layers between 12 km and 16 km as observed by various lidar stations around the globe. The dashed lines show the expected air movements at the latitudes and heights involved (Newell et al., 1972).

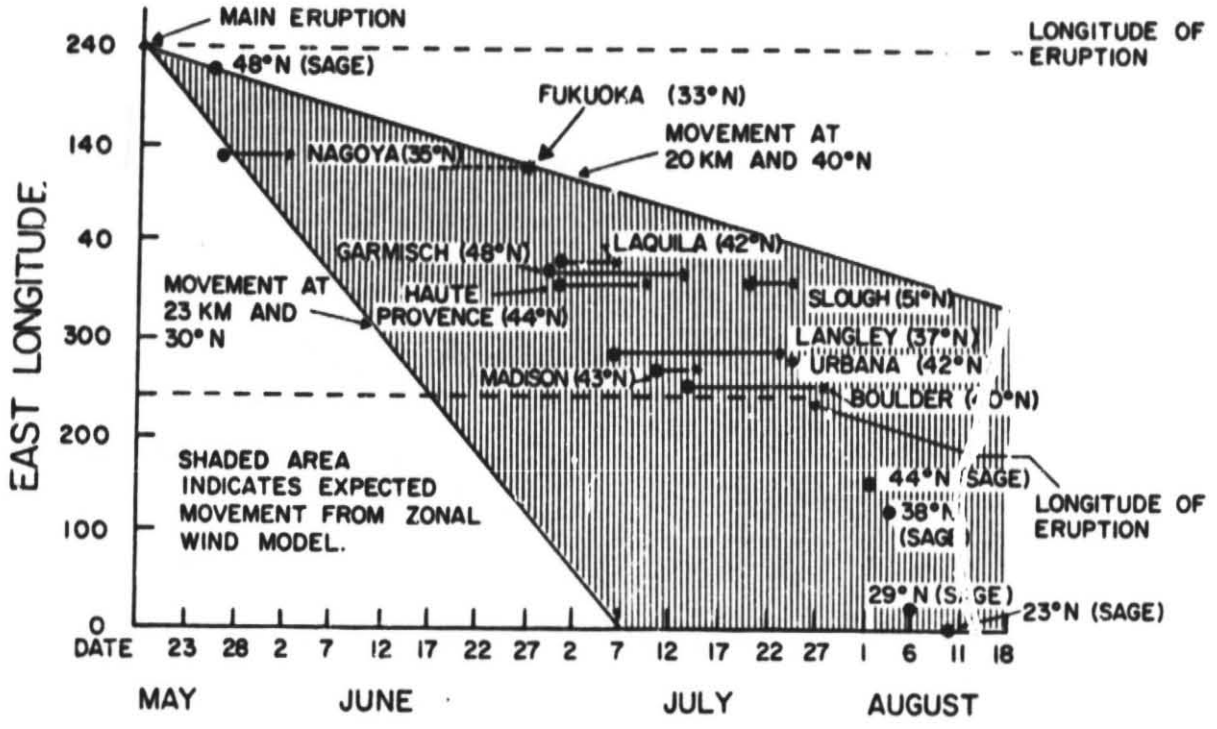

*Figure 7.12 Times of arrival of aerosol layers above 20 km as observed by various lidar stations around the globe. * Layer at 20 tp 22 km. ● Layer at 22 to 24 km. The crosshatched area represents the average expected range of stratospheric air movements. Also shown are the dates, latitudes and longitudes of SAGE observations.*

In both figures there is good agreement between the observed arrival times and the predictions of the model. In Fig. 7.12, the distinction between the arrival of material at 20 to 22 km and at 22 to 24 km is also clear, the higher material traveling faster and being observed first at all stations. The SAGE observations of the higher altitude material also agree well and it should be noted that this is after about one and one half circuits of the Earth. The agreement in Fig. 7.11 is not as good as that in Fig. 7.12, which is to be expected, in view of the higher velocities and more irregular air streams in the lower stratosphere. Nevertheless, the agreement is still good and, where it has been possible to distinguish between layers at different altitudes, the higher level layer has been observed first, as predicted by the model.

The meridional dispersions of the volcanic material will be discussed in the next section in conjunction with the mass analysis.

7.5 Mass Loading and Meridional Movement

In Section 4.2, we discussed the stratospheric mass loading changes produced by Mount St. Helens, concluding, on the basis on SAGE data, that the total loading increased by about 3×10^5 tonnes, on which about 90 percent remained in the northern hemisphere in September 1980. Detailed analyses of the mass loading changes and distribution are rendered difficult by the existance of aerosol from Sierra Negra at the time of the St. Helens eruption and by the eruption of Ulawun before the St. Helens aerosol had decreased to any appreciable extent.

The total mass loading from St. Helens remained at about its peak value of 3×10^5 tonnes between August and October, that is between 3 and 5 months after the eruption. As commented on, in Section 7.2, the November 1980 SAGE sweep did not extend further enough north to obtain a mass loading for St. Helens at this time, even though the influence of Ulawun was still confined mainly to the equatorial zone. One point of interest not discussed in Section 4.2 is whether there is evidence of movement of material from St. Helens into the equatorial zone and across into the southern hemisphere. In order to examine this, the mean optical depth, for the latitude belt $-20° \rightarrow +20°$, has been computed for the period April to October 1980 (data for October is computed for longitudes 90° W to 90° E only, to avoid contamination by Ulawun). The results of this computation are shown in Fig. 7.13. As mentioned earlier the equatorial zone shows little seasonal variation in optical depth and the decrease between April and May is almost certainly due to the remaining affects from the eruption of Sierra Negra. Between May and August there is very little change but, between August and October, there is a definite increase. The equivalent rise in mass loading is about 60 kilotonnes or about 20 percent of the total peak loading from St. Helens. We, thus, have evidence of appreciable southward transport of the St. Helens material. More detailed inspection of the latitudinal

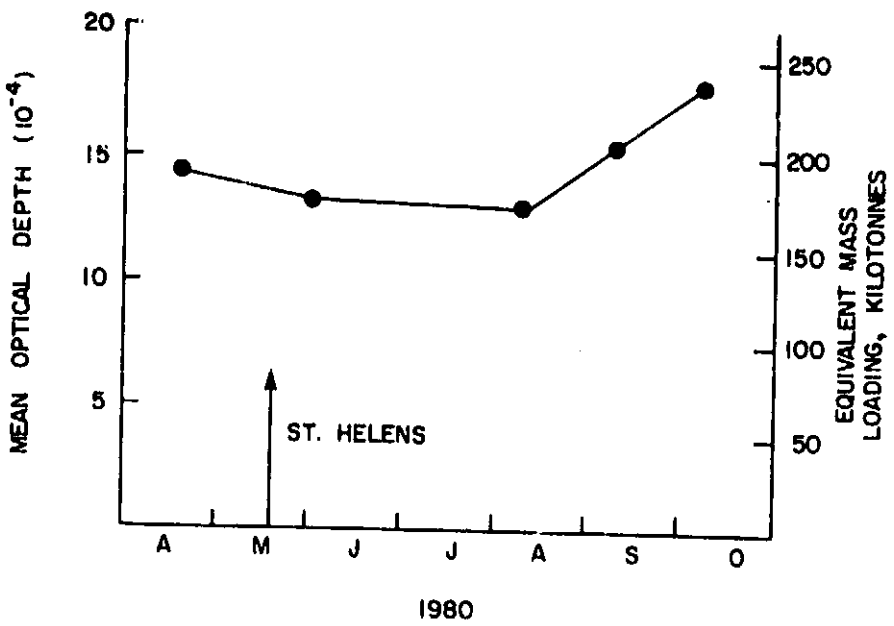

Figure 7.13 Variation of stratospheric optical depth and equatorial mass loading in the equatorial sector (20°S–20°N) during the period April–October 1980.

distribution in October 1980 show that, of this 20 percent, some 15 percent was still between 0° and 20° N and about 5 percent had crossed the equator into the southern hemisphere.

It is also possible to use the lidar data presented in Section 7.3 to compute a figure for the total aerosol mass loading. Since the lidar data set is confined to a small part of the northern hemisphere, such an estimate will be based on very poor sampling compared to estimates based on SAGE data. In order to have a reasonable chance of a reliable estimate, it is necessary to wait until it can be assumed that the volcanic material is well dispersed zonally. This will also mean that vertical layering has, to a large extent, disappeared.

As an example, let us consider the lidar profile of November 12, 1980, shown in Fig. 7.7(c) and take a conversion factor for $\beta_{0.69}$/Mass as 36.6 $m^2\ kg^{-1}\ sr^{-1}$ (Section 4.1). If we assume that the NASA-Langley lidar profile represents an average for the whole northern hemisphere, we may integrate the profile and arrive at a total mass loading for the northern hemisphere of 7.5×10^5 tonnes. This may be contrasted to the value of 6.0×10^5 shown in Fig. 4.8 and computed from SAGE data. This value could undoubtedly be refined by examining our assumption that the NASA-Langley profile is typical of the whole northern hemisphere. Lidar data from other stations could be included and also that from the airborne lidar. In the absence of SAGE information this would undoubtedly be a worthwhile procedure. Given the exitance of SAGE data and the unlikelihood of obtaining better accuracy for mass loading figures from lidar, this procedure has not been attempted for St. Helens. Under other circumstances, such as after the recent eruption of El Chichon, when no SAGE data were available, the use of airborne lidar data for mass calculations has been extremely useful.

8. QUARTZ CRYSTAL MICROBALANCE DATA

An indicated earlier, analysis of the QCM data from the November 1978 experiments, performed near Söndrestrom, Greenland, has led us to decide against using these data as a quantitative indicator of stratospheric aerosol concentrations. A detailed analysis of these data carried out by A. Zardecki of IFAORS is included in the Appendix to this report, together with a brief outline of the theory of operation of the instrument. In the Appendix the data are presented as cumulative aerosol size distributions and are used to calculate the equivalent optical extinction at 1.0 μm.

An example of an aerosol size distribution, $(dN/d \log r)$, calculated from the cumulative size distribution measured using the QCM at an altitude of 11.3 km, is shown in Fig. 8.1. Also shown in the same figure is a size distribution obtained by Farlow et al (1981) at 12.2 km over Poker Flat, Alaska, in July 1979. This measurement was made by collecting aerosol particles of cylindrical wires and returning the samples to the laboratory for analysis. Both sets of measurements are made at similar latitudes and altitudes and might be expected to agree reasonably well. The difference between them is significant and typical of the early QCM data. The Farlow et al curve shows the familiar unimodal distribution normally accepted as typical for stratospheric aerosol size distributions (Russell et al, 1981). In contrast, the QCM data show an excess of both small and large particles. The latter, in particular, is responsible for the rather large mass loadings often quoted for QCM data (Chuan et al, 1981).

A further comparison of QCM and other data are shown in Table 8.1 which lists mass loading and optical extinction values. Two values of mass loading are shown, taken from Chuan et al (1981) for the QCM, and Farlow et al (1981), for impactor data. Farlow et al, discuss their impactor data in some detail, comparing it with other measurements on stratospheric aerosols. They conclude that their own values may be slightly high (the particle radii should be reduced by about 15 percent), but certainly not low. Nevertheless, the QCM values are still higher by a factor of about six. The 1.0 μm extinction values shown for the Greenland QCM data are based on our own calculations (see Appendix) and yield a value of the order of 10^{-3} km^{-1}. The SAM II and SAGE experimental values for the same conditions are less than or equal to 2×10^{-4} km^{-1}, agreeing quite well with values calculated from Farlow et al's data, but not the QCM based values, which are one-half to one order of magnitude larger.

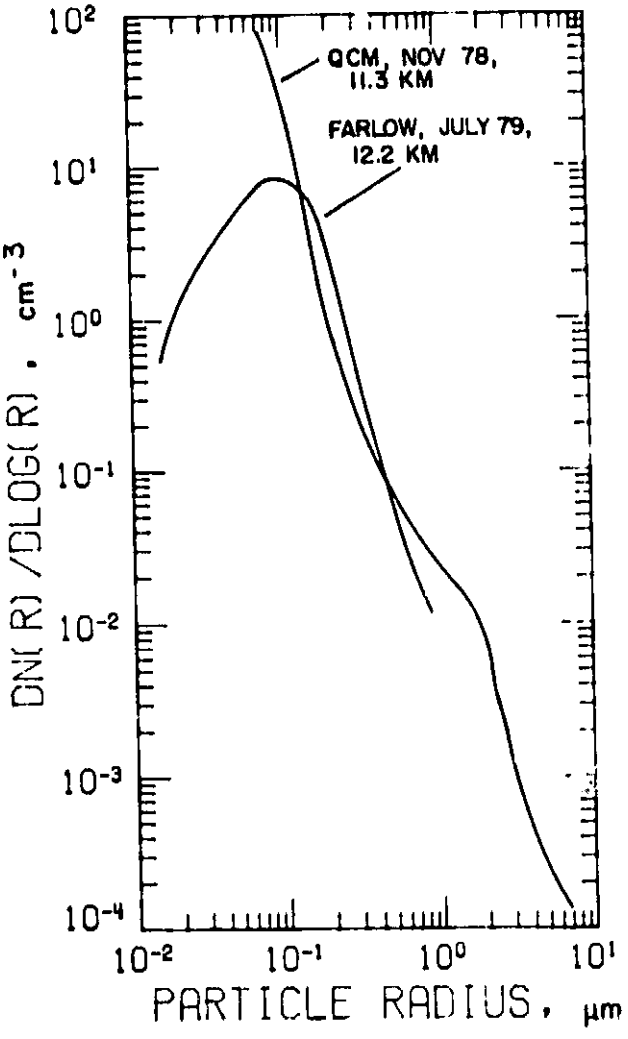

Figure 8.1 Aerosol particle size distributions obtained by: the quartz crystal microbalance over Greenland in November 1978 and by wire impactor over Alaska in July 1979 (Farlow et al., 1981).

TABLE 8.1: COMPARISON OF QCM AND OTHER DATA

Date	Location	Altitude	Authors	Instrument	Mass loading	1.0 μm extinction (km^{-1})
Nov 78	Greenland	11.3 km	---	QCM	---	6.1×10^{-4}
		13.0 km	---	QCM	---	11.9×10^{-4}
		12.5 km	Russell et al (1981a)	SAM II	---	2.0×10^{-4}
Jul 79	Alaska	12-18 km	Chuan et al (1981)	QCM	1 $\mu g\ m^{-3}$	
		12-18 km	Farlow et al (1981)	Impactor	0.16 $\mu g\ m^{-3}$	1.86×10^{-4}
		12-18 km		SAGE	---	1.2×10^{-4}

9. SUMMARY AND CONCLUSIONS

Tables 9.1 and 9.2 summarize the main findings with regard to the aerosol mass loading changes produced by the three volcanoes studied, together with an outline of Ulawun's behavior (Table 9.1), and their growth and dispersion characteristics (Table 9.2). The analysis has also demonstrated the range of information that is potentially available from satellites such as SAGE and from lidar, whether airborne or ground-based. It has, in addition, shown that the information given by these techniques (and by the quartz crystal microbalance when the calibration of this has been completed) is complimentary rather than overlapping, enabling different aspects of the aerosol behavior to be measured.

The study was fortunate in having a nine-month period of measurements on a quiet background stratospheric aerosol layer (the effects of Soufriére were negligible on a global scale). This has enabled not only the mass loading to be determined accurately but also the seasonal changes to be studied. One finding that was not anticipated was the division of the background aerosol into three latitude bands separated at approximately 25°N and S.

The various volcanoes studied show a considerable variety of stratospheric affects. Although not all the characteristics listed below could be studied for each volcano, the following summary can be given of their general behavior.

a) The injected mass disperses quite rapidly both longitudinally and latitudinally. The general behavior corresponds well to global circulation models but individual upper level weather systems can cause major local deviations from these.

b) The volcanic aerosol has a tendency to divide or isolate itself into zones similar to those into which the background aerosol is divided. Considerable flow of material occurs between these zones, flow taking place along isentropic surfaces.

c) The time between the eruption and the maximum mass loading increase is about 3 months, in agreement with the model of Turco et al. (1981). The peak loading is followed by a slow delcine, the initial decay time (determined for Sierra Negra only) is about 5 months.

d) The two equatorial volcanoes (Sierra Negra and Ulawun) show a gradual rise in the height of the injected material with time after the eruption. Several explanations are possible for this.

The 1981 SAGE and lidar data, when analyzed, should add very considerably to the above picture. It is anticipated that, when the study of these is complete, it will be possible to establish the general characteristics of the growth and dispersion of stratospheric plumes resulting from volcanic eruptions.

TABLE 9.1: STRATOSPHERIC AEROSOL MASS LOADING CHANGES - SUMMARY

SUBJECT		ESTIMATED MASS LOADING (METRIC TONS)
Present Analysis (SAGE data, unless otherwise stated)		
Global background pre-volcanic, 1979 - total		$\sim 4.8 \times 10^5$
- winter maximum		$2.5 - 2.7 \times 10^5$
- summer maximum		$2.2 - 2.3 \times 10^5$
Soufrière - Total injection		$2.1 \pm .7 \times 10^3$
Sierra Negra - Peak total injection	3 months after eruption	$\sim 1.8 \times 10^5$
peak northern hemisphere		$\sim 1.1 \times 10^5$
peak southern hemisphere		$\sim 0.7 \times 10^5$
total injection	6 months after eruption	$\sim 0.9 \times 10^5$
northern hemisphere		$\sim 0.5 \times 10^5$
southern hemisphere		$\sim 0.4 \times 10^5$
St Helens - Peak total injection	4 months after eruption	$\sim 3.0 \times 10^5$
peak northern hemisphere		$\sim 2.8 \times 10^5$
peak southern hemisphere		$\sim 0.2 \times 10^5$
peak injection (LIDAR)		$\sim 4.5 \times 10^5$
Ulawun - Total injection, six weeks after eruption		2.0×10^5
Earlier Volcanoes		
Agung (March, 1963) - total injection		3×10^7 (Cadle et al., 1976 Cadle et al., 1977)
Fuego (October, 1974) - total injection		$3 - 6 \times 10^6$ (Cadle et al., 1976, Cadle et al., 1977 Lazrus et al., 1979)
St Augustine (January, 1976) - total injection		6×10^5 (Cadle et al., 1977)

TABLE 9.2: COMPARISON OF THE STRATOSPHERIC EFFECTS PRODUCED BY THE ERUPTIONS OF SOUFRIÉRE, SIERRA NEGRA, ST. HELENS AND ULAWUN

Volcano	Date of Eruption	Latitude	Peak Mass Injection (10^5 Metric Tons)	Time From Eruption to Peak Loading (Months)	Decay Time to 1/e of Peak Loading (Months)	Dispersion Characteristics
Soufriere	April 1979	13.3°N	2.1×10^3	Not Available	Not Available	25% of the injected aerosol stayed within the equatorial zone; 75% moved rapidly North within ten days of the eruption. Material changed latitude approximately isentropically. Long term dispersion characteristics are unknown.
Sierra Negra	Nov. 1979	0.8°S	1.8×10^5	3	5	40% of the injected aerosol moved rapidly northward. A declining equatorial reservoir was visible up to June, 1980. Material changed latitude isentropically and that remaining in the equatorial zone gradually rose in height after its injection.
St Helens	May 1980	46.2°N	3.0×10^5	4 ± 1	Not Available	A majority of the injected material moved to the North of the volcano and dispersed only slowly from that region. 5 months after the eruption, 80% of the injected material was still North of 20°N, only 5% had crossed the equator.
Ulawun	Oct. 1980	5.0°S	$\geq 2.0 \times 10^5$	≥ 1.5	Not Available	New stratospheric material was still well confined to the equatorial zone six weeks after the eruption. The height of the material gradually increased during this period.

10. ACKNOWLEDGEMENTS

This work was supported by Contract NAS1-16253 with NASA-Langley Research Center. We are grateful to M. P. McCormick, L. R. McMaster, and W. Fuller of NASA-LaRC for giving assistance on many aspects of this work and for providing the data on which it was based. Our thanks are also due to W. Chu of NASA-LaRC and T. Swissler, M. Osborne, and H. Steele of SASC for help with the data processing and to U. Farrukh of IFAORS for giving assistance in its analysis. The QCM data analysis reported in Appendix 1 of this report was carried out independently by A. Zardecki of IFAORS.

11. REFERENCES

Cadle, R. D., C. S. Kiang, and J. F. Louis, The Global Scale Dispersion of the Eruption Clouds from Major Volcanic Eruptions, *J. Geophys. Res., 81*, 18, 3125-3132, 1976.

Cadle, R. D., F. G. Fernald, and C. L. Frush, Combined Use of Lidar and Numerical Diffusion Models to Estimate the Quantity and Dispersion of Volcanic Eruption Clouds in the Stratosphere: Volcán Fuego, 1974, and Augustine, 1976. *J. Geophys. Res.*, Vol. 82, No. 12, Apr. 20, 1977, 1783-1786.

Chuan, R. L., D. C. Woods and M. P. McCormick, Characterization of Aerosols from Eruptions of Mount St. Helens, *Science 211*, 830-832, 1981.

D'Altorio, A. and G. Visconti, Lidar Detection of Volcanic Aerosols in the Atmosphere following the Mount St. Helens Eruption, *Geophys. Res. Lett., 8*, 63-65, 1981.

DeLuisi, J., V. Derr, R. Fegley, and T. McNice, Lidar Observations of Atmospheric Debris from the Mount St. Helens Eruption at Boulder and Mauna Loa, Tenth International Laser Radar Conference Abstracts, 147, October 6-9, 1980, Silver Spring, Maryland.

Dutton, J. A., The Ceaseless Wind, McGraw Hill, New York, 1976.

Eloranta, E. W., Lidar Observations of Stratospheric Dust over Madison, Wisconsin, after the Mount St. Helens Eruption, Tenth International Laser Radar Conference Abstracts, 144-145, October 6-9, 1980, Silver Spring, Maryland.

Farlow, N. H., V. R. Oberbeck, D. S. Colburn, and G. V. Ferry, Comparison of Stratospheric Aerosol Measurements over Poker Flat, Alaska, July 1979, *Geophys. Res. Lett., 8*, 15-17, 1981.

Fujiwara, M., T. Shibata, and M. Hirono, Lidar Observations of Sudden Increase of Aerosols in the Stratosphere Caused by Volcanic Injections, II. Sierra Negra Event, *J. Atmos. Terr. Phys.*, to be published in 1982.

Fuller, W. H., W. H. Hunt and S. Sokol, Airborne Lidar Measurements of the Soufriére, St. Vincent Eruption of April 17, 1979, *Science 26*, 1113-1114, 1982.

Gradrud, B. W. and A. L. Lazrus, Filter Measurements of Stratospheric Sulfate and Cloride in the Eruption Plume of Mount St. Helens, *Science 211*, 826-827, 1981.

Gardner, C. S., C. F. Sechrist, Jr., and J. D. Shelton, Lidar Observations of the Mount St. Helens Dust Layers over Urbana, Illinois, Tenth International Laser Radar Conference Abstracts, 140-141, October 6-9, 1980, Silver Spring, Maryland.

Gras, J. L. and G. P. Ayers, On Sizing Impacted Sulfuric Acid Aerosol Particles, *J. Appl. Meteor. 18*, 634-638, 1979.

Hauchecorne, A., J. Lefrere, G. Megie, and M. L. Chanin, Lidar Observations of Stratospheric Aerosol Layers over France after the Mount St. Helens Eruption, Tenth International Laser Radar Conference Abstracts, 146, October 6-9, 1980, Silver Spring, Maryland.

Hayes, D., K. Snetsinger, G. Ferry, V. Oberbeck and N. Farlow, Reactivity of Stratospheric Aerosols to Small Amounts of Ammonia in the Laboratory Environment, *Geophys. Res. Lett. 7*, 974-976, 1980.

Hirono, M., M. Fujiwara, T. Shibata, and N. Kuyumuja, Lidar Observations of Volcanic Clouds in the Stratosphere over Fukuoka, Caused by Eruptions of Mount St. Helens in May 1980, to be published in *Geophys. Res. Lett.*

Hofmann, D. J. and A. M. Rosen, Balloon-borne Observations of Stratospheric Aerosol and Condensation Nuclei during the Year following the Mount St. Helens Eruption, U. of Wyoming, Dept. of Physics and Astronomy, Report No. AP-63, July 1981.

Iwasake, Y. and S. Hayashida, Lidar Measurements of Dust-Cloud Particles Loaded into the Stratosphere by the Volcanic Eruption of St. Helens, Tenth International Laser Radar Conference Abstracts, 142-143, October 6-9, 1980, Silver Spring, Maryland.

Kent, G. S., SAGE Measurements of Mount St. Helens Volcanic Aerosols, Proceedings of the Symposium on "Mount St. Helens Eruption: Its Atmospheric Effects and Potential Climatic Impact," Washington, DC, November 18-19, 1980, Spectrum Press, 1982.

Kent, G. S., Lidar Measurements of Elluents from the Soufriére and Mount St. Helens Volcanoes, IAMAP Third Scientific Assembly Radiation Commission Symposium *Application of Lidar to Atmospheric Radiation and Climate Studies*, Conference Abstracts, 91, 1981.

Lazrus, A. L. and B. W. Gandrud, Stratospheric Sulfate Aerosol, *J. Geophys. Res. 79*, 3424-3431, 1974.

Lazrus, A. L., R. D. Cadle, B. W. Gandrud, J. P. Greenberg, B. J. Huebert, and W. I. Rose, Jr., Sulfur and Halogen Chemistry of the Stratosphere and of Volcanic Eruption Plumes, *J. Geophys. Res., 84*, C12, 7869-7875, 1979.

McCormick, M. P., The Use of Lidar for Atmospheric Measurements in Remote Sensing Energy Related Studies, T. Nejat Vezeroglu (Ed.), Hemisphere Press, Washington, (Distributed by Wiley, NY) 1975, 113-118.

McCormick, M. P., T. J. Swissler, W. P. Chu and W. H. Fuller, Jr., Post-Volcanic Stratospheric Aerosol Decay as Measured by Lidar, *J. Atmos. Sci., 35*, 1296-1303, 1978.

McCormick, M. P., P. Hamill, T. J. Pepin, W. P. Chu, T. J. Swissler and L. R. McMaster, Satellite Studies of the Stratospheric Aerosol, *Bulletin of the American Meteor. Soc. 60*, 1038-1046, 1979.

McCormick, M. P., G. S. Kent, G. K. Yue and D. M. Cunnold, SAGE Measurements of the Stratospheric Aerosol Dispersion and Loading from the Soufriére Volcano, NASA Technical Paper 1922, November 1981.

McCormick, M. P., G. S. Kent, G. K. Yue and D. M. Cunnold, Stratospheric Aerosol Effects from Soufriére, St. Vincent as Measured by the SAGE Satellite System, *Science, 26*, 1982.

McCormick, M. P., Lidar Measurements of Mount St. Helens Effluents, *Optical Engineering 21*, 340-342, 1982.

Newell, R. E., J. W. Kidson, D. G. Vincent, and G. J. Boer, The General Circulation of the Tropical Atmosphere and Interactions with Extratropical Latitudes, Volume 1, The M.I.T. Press, 1972.

Newell, R. E. and A. Deepak (Ed.), Mount St. Helens Eruptions of 1980, NASA SP-458, 1982.

Pinnick, R. G., J. M. Rosen and D. J. Hofmann, Stratospheric Aerosol Measurements, III: Optical Model Calculations, *J. Atmos. Sci., 33*, 304-314, 1976.

Reiter, E. R., Stratospheric-Tropospheric Exchange Processes, *Rev. Geo. and Space Physics 13*, 459-474, 1975.

Reiter, R., H. Jager, W. Carnuth, and W. Funk, Lidar Observations of the Mount St. Helens Eruption Clouds over Mid-Europe, May to July 1980, *Geophys. Res. Lett., 7*, 1099-1101, 1980.

Rosen, J. M., D. J. Hofmann, and J. Laby, Stratospheric Aerosol Measurements, II: The Worldwide Distribution, *J. Atmos. Sci., 32*, 1457-1462, 1975.

Russell, P. B., T. J. Swissler, M. P. McCormick, W. P. Chu, J. M. Livingston and T. J. Pepin, Satellite and Correlative Measurements of the Stratospheric Aerosol, I: An Optical Model for Data Conversions, *J. Atmos. Sci., 38*, 1279-1294, 1981.

Russell, P. B. and P. Hamill, Spatial Variation of Stratospheric Aerosol Composition and Model Refractive Index: *J. Atmos. Sci., 41*,1781-1790, 1984.

Schuerman, D. W., Light Scattering by Irregularly Shaped Particles, Plenum Press, New York, 1979.

SEAN Bulletin 7, No. 7, July 31, 1982.

Sedlacek, W. A., E. J. Mroz, and G. H. Heiken, Stratospheric Sulfate from the Gareloi Eruption, 1980, *Geophys. Res. Lett., 8,* 761-764, 1981.

Shepard, J. B., W. P. Aspinall, K. C. Rowley, J. Pereira, H. Sigurdsson, R. S. Fiske, and J. F. Tomblin, The Eruption of Soufriére Volcano, St. Vincent, April-June 1979, *Nature,* Vol. 282, No. 5734, Nov. 1, 1979, 24-28.

Smith, W. L., H. M. Woolf, C. M. Hayden, D. Q. Wark, and L. M. McMillin, The TIROS-N Operational Vertical Sounder, *Bull. American Meteorol. Soc.,* Vol. 60, No. 10, Oct. 1979, 1177-1187.

Swissler, T. J., P. Hamill, M. Osborn, P. B. Russell, and M. P. McCormick, A Comparison of Lidar and Balloon-borne Particle Counter Measurements of the Stratospheric Aerosol, 1974-1980, *J. Atmos. Sci., 39,* 909-916, 1982.

Thomas, L., C. P. Chaloner, and S. K. Bhattacharyya, Laser-Radar Measurements in Southern England of Aerosols from Mount St. Helens, *Nature, 289,* 473, 1981.

Toon, O. B., R. P. Turco, P. Hamill, C. S. Kiang, and R. C. Whitten, A One-Dimensional Model Describing Aerosol Formation and Evolution in the Stratosphere, II: Sensitivity Studies and Comparison with Observations, *J. Atmos. Sci., 36,* 718-736, 1979.

Turco, R. P., P. Hamill, O. B. Toon, R. C. Whitten and C. S. Kiang, A One-Dimensional Model Describing Aerosol Formation and Evolution in the Stratosphere, I: Physical Processes and Mathematical Analogs, *J. Atmos. Sci., Vol. 36,* 699-717, 1979.

Turco, R. P., R. C. Whitten, O. B. Toon, J. B. Pollack, and P. Hamill, OCS, Stratospheric Aerosols and Climate, *Nature, 283,* 283-286, 1980a.

Turco, R. P., R. C. Whitten, O. B. Toon, J. B. Pollack, and P. Hamill, Carbonyl Sulfide, Stratospheric Aerosols and Terrestrial Climate, *Environmental and Climatic Impact of Coal Utilization,* J. J. Singh and A. Deepak, Editors, Academic Press, New York, 331-356, 1980b.

Turco, R. P., O. B. Toon, R. C. Whitten, R. G. Keesee, and P. Hamill, The Mount St. Helens Eruptions of May and June 1980: Simulation Studies of the Physical and Chemical Processes Occurring in the Stratospheric Clouds of the Mount St. Helens Eruption of May and June 1980, *Proc. Sym. Mt. St. Helens,* Washington, DC, November 18-19, 1980, Spectrum Press, in press, 1982.

APPENDIX 1

PHYSICAL AND OPTICAL PROPERTIES OF STRATOSPHERIC AEROSOLS BASED ON MEASUREMENT BY QUARTZ CRYSTAL MICROBALANCE CASCADE IMPACTOR

by

A. Zardecki

APPENDIX 1

PHYSICAL AND OPTICAL PROPERTIES OF STRATOPHERIC AEROSOLS BASED ON MEASUREMENTS BY QUARTZ CRYSTAL MICROBALANCE CASCADE IMPACTOR

A. Zardecki

I. INTRODUCTION

The purpose of this investigation is to extract information about physical and optical properties of stratospheric aerosols on the basis of measurements performed by the Quartz Crystal Microbalance (QCM) impactor. The data, which we are using, were collected during flights over Sonderstrom, Greenland, in late November 1978. Since the QCM instruments provides essentially the logarithmic mass distribution $dM/d \log_{10} d_p$, d_p being the particle diameter, our first task is to convert the mass data into aerosol size distribution. Two methods to achieve this will be described in this report: least square curve fit and point-by-point power law fit. Once the size distribution is obtained, the Mie theory enables one to calculate, in particular, the extinction and backscatter coefficients. These will be presented together with physically meaningful extinction to number and backscatter to number ratios.

II. BRIEF THEORY OF QCM CASCADE IMPACTOR

Inertial impactors are devices used to classify particles with respect to their aerodynamic size. The instrument consists of a series of stages, each composed of an orifice through which the aerosol flows normal to a collecting surface. The air flows over the collecting surface and on to the next stage. Particles too large to follow the air medium deposit on the collecting surface. The basic mechanism of collection is inertial impaction.

The efficiency of a stage for particles of a given size is defined as the fraction of the particles removed from the gas flowing through the stage. At a given flow rate, the stage efficiency depends on the Stokes number, St, given as

$$St = \frac{C\rho_p U d^2}{18\mu d} \qquad (1)$$

which is defined as the ratio of the particle stopping distance to a characteristic length such as the jet diameter. In Eq. (1), U is the average velocity through the jet, d is, at width or diameter, ρ_p, is the particle density, C is the Cunningham slip correction factor, d_p is the particle diameter, and μ is the fluid viscosity. Ideally, the efficiency curve should be a step function corresponding to a given Stokes parameter. In practice, the efficiency curve is "S" shaped. A stage is usually characterized by the diameter corresponding to 50% efficiency:

$$d_p^* = \left[\frac{18\mu d St^*}{C\rho_p U} \right]^{\frac{1}{2}} \qquad (2)$$

where the asterisk refers to the value at 50% efficiency.

For complex aerosol particles, impactor data are often reported in terms of the aerodynamic diameter, defined as the diameter of a hypothetical sphere of unit density with the same Stokes number as the particle in question. Since the variation in the Cunningham slip factor is usually negligible for small diameter differences, Eq. (1) implies the geometric diameter, $d_p^{(g)}$, is related to the aerodynamic diameter, $d_p^{(a)}$, through

$$d_p^{(g)} = d_p^{(a)} / \sqrt{\rho_p} \qquad (3)$$

The quartz crystal microbalance impactor (QCM) is a multistage impactor which senses the mass of suspended aerosols, as a function of particle size[3,4]. Each impactor stage contains a piezoelectric crystal microbalance which senses the mass of the particles collected by a change in oscillator frequency between a reference crystal and the sensing crystal. This technique, providing data free from some of the ambiguities present in light scattering data, has been proposed to be used for measurements to support the SAM II and SAGE ground truth programs.

III. DETERMINATION OF THE SIZE DISTRIBUTION

The mass of particles, M, collected on an impaction plate in usually expressed in terms of the logarithmic mass distribution

$$K = dM/d \log_{10} d_p \qquad (4)$$

where d_p is the particle diameter. Let d_{p1} and d_{p2} denote the lower and upper bounds of particle diameters deposited at a given stage. This corresponds to the number $\Delta N_{1,2}$ of particles given as

$$\Delta N_{1,2} = \int_{d_{p1}}^{d_{p2}} \frac{dN}{dd_p} \, dd_p \qquad (5)$$

Employing a log scale, Eq. (5) is rewritten as

$$\Delta N_{1,2} = (\ln 10)^{-1} \int_{d_{p1}}^{d_{p2}} \frac{dN}{d \log_{10} d_p} \frac{dd_p}{d_p} \qquad (6)$$

We now assume that for a given stage the function $dN/d \log_{10} d_p$ is nearly constant as compared d_p^{-1}. Eq. (6) thus becomes

$$\Delta N_{1,2} = (\ln 10)^{-1} \frac{dN}{d \log_{10} d_p} \int_{d_{p1}}^{d_{p2}} \frac{dd_p}{d_p}$$

$$= \frac{dN}{d \log_{10} d_p} \ln (d_{p2}/d_{p1})/\ln 10 \qquad (7)$$

For the Celesco Model C-1000 QCM Cascade, the 50% efficiency points for each stage as given by the instrument manufacturer are listed below:

Stage	Diameter (Microns)
1	25.00
2	12.50
3	6.25
4	3.20
5	1.60
6	0.80
7	0.70
8	0.20
9	0.10
10	0.05

It is seen that the ratio of two consequtive 50% efficiency points is constant and equals 2. This permits us to assume the constant ratio $d_{p2}/d_{p1} = 2$ in Eq. (7), which thus yields

$$\Delta N_{1,2} = \frac{dN}{d \log_{10} d_p} \log 2 \qquad (8)$$

Since $\Delta M = dN(4/3)\pi (d_p/2)^3 \rho_p$, we obtain for the size distribution dN/dd_p, in terms of the measured quantity κ, the following formula:

$$\frac{dN}{dd_p} = \frac{K}{(4/3)\pi(d_p/2)^3 \rho_p d_p \ln 10} \tag{9}$$

Or introducing the particle size distribution for radius $r = d_p/2$, Eq. (3) becomes

$$n(r) \equiv \frac{dN}{dr} = \frac{3K}{4\pi r^4 \rho \ln 10} \tag{10}$$

Tables 1-3 summarize both the mass data and the radius distribution functions as obtained from Eq. (10). The results refer to stratospheric aerosols measurements made over Sondrestrom, Greenland, in late November 1978. Included is also the number of particles registered at a given stage, N, related to K through the formula

$$\Delta N = \frac{3K \log_{10} 2}{4\pi \rho_p r^3} \tag{11}$$

TABLE 1: Data for Mass Distribution and Size Distribution at Altitude z = 37,000 feet

STAGE NO.	d_p (μm)	r (μm)	K (mg m^{-3})	ΔN (cm^{-3})	n(r) ($cm^{-3}\mu m^{-1}$)
10	0.05	0.025	0.40	1.02×10^{-3}	$5.90 \times 10^{+4}$
9	0.10	0.050	0.43	1.37×10^{-2}	$3.96 \times 10^{+3}$
8	0.20	0.100	0.37	1.48×10^{-1}	$2.13 \times 10^{+2}$
7	0.40	0.200	0.13	0.65×10^{0}	4.68×10^{0}
6	0.80	0.400	---	------	------
5	1.60	0.800	0.26	1.79×10^{-2}	3.23×10^{-2}
4	3.20	1.600	1.16	1.03×10^{-2}	1.02×10^{-2}
3	6.40	3.200	0.56	0.68×10^{-3}	3.08×10^{-4}
2	12.80	6.400	0.76	1.16×10^{-4}	2.61×10^{-5}

TABLE 2: Data for Mass Distribution and Size Distribution at Altitude z = 41,000 feet

STAGE NO.	d_p (μm)	r (μm)	K (mg m^{-3})	ΔN (cm^{-3})	n(r) ($cm^{-3}\mu m^{-1}$)
10	0.05	0.025	0.500	1.28×10^{3}	7.37×10^{4}
9	0.10	0.500	0.560	1.79×10^{2}	5.16×10^{3}
8	0.20	0.10	0.400	1.59×10^{1}	2.30×10^{2}
7	0.40	0.20	0.430	2.14×10^{0}	1.55×10^{1}
6	0.80	0.40	----	----	----
5	1.60	0.80	0.500	3.90×10^{-2}	7.03×10^{-2}
4	3.20	1.60	1.025	9.99×10^{-3}	3.01×10^{-3}
3	6.40	3.20	0.800	9.75×10^{-3}	4.39×10^{-4}
2	12.80	6.40	0.930	1.42×10^{-4}	3.19×10^{-5}

TABLE 3: Data for Mass Distribution and Size Distribution at Altitude z = 43,000 feet

STAGE NO.	d_p (μm)	r (μm)	κ ($mg\ m^{-3}$)	ΔN (cm^{-3})	$n(r)$ ($cm^{-3}\mu m^{-1}$)
10	0.05	0.025	---	---	------
9	0.10	0.500	---	---	------
8	0.20	0.100	0.63	2.52×10^{1}	3.63×10^{2}
7	0.40	0.200	0.33	1.64×10^{0}	1.19×10^{1}
6	0.80	0.400	---	---	------
5	1.60	0.800	0.27	2.11×10^{-2}	3.80×10^{-2}
4	3.20	1.600	0.30	2.92×10^{-3}	1.54×10^{-2}
3	6.40	3.200	0.80	0.97×10^{-3}	4.35×10^{-4}
2	12.8	6.40	0.53	0.81×10^{-4}	1.82×10^{-5}

III. RETRIEVAL OF OPTICAL PARAMETERS

Once the particle size distribution has been determined, the optical quantities of interest, such as the extinction and backscatter coefficients, can be computed by applying the standard results of the Mie theory. In terms of the Mie efficiency factor for extinction, Q_{ext}, the extinction coefficient is given by

$$\beta_{ext} = \int_{r_1}^{r_2} Q_{ext}(m,x)\pi r^2 \, n(r)\,dr \tag{12}$$

where the complex refractive index $m = m_1 - im_2$, x denotes the size parameter, while r_1 and r_2 are the minimum and maximum values of the particle radii.

The backscatter coefficient is defined as the power scattered back per steradian divided by the incident flux. Introducing the Mie amplitude $S_1(x,m,\theta)$ and the Mie intensity function $i_1(x,m,\theta)$ equals $|S_1(x,m,\theta)|^2/k^2$, where k is the wave number, we can express the backscatter coefficient as

$$\sigma_B(m,x) = i_1(x,m,180)$$

$$= |S_1(x,m,180)|^2/k^2 \tag{13}$$

Equation (13), which holds for monodisperse aerosols, differs by a factor 4π from the definition

adopted by Deirmendjian.[5] In the case of polydisperse aerosols, the situation studied here, the backscatter coefficient β_p is obtained on integration over the size distribution. Thus

$$\beta_p(\lambda,m) = \int_{r_1}^{r_2} i_1(x,m,180)\, n(r)\, dr \qquad (14)$$

In actual computations, we have at our disposal a sequence of 6-8 values of $n_i = n(r_i)$ from which we wish to reconstruct the true size distribution $n(r)$. Two different methods of reconstruction have been used: (i) the least square curve fit; (ii) point-by-point power law fit. We now proceed to a brief description of these methods and to presentation of sample results.

A. Least Square Curve Fit

The data points contained in Tables I-III show a fairly monotonic decrease when displayed on a log-log plot. This suggests the following five parameter fit to the size distribution

$$\log_{10} n(r) = C_1 + C_2 \log_{10} r + C_3(\log_{10} r)^2 + C_4(\log_{10} r)^3 + C_5(\log_{10} r)^4 \qquad (15)$$

with the coefficients C_i, $i = 1, \ldots, 5$ to be determined. We notice that the first two terms on the right hand side of Eq. (15) reproduce the power-law size distributions. The remaining terms, therefore, can be considered as corrections to the power law, where $n(r) \sim r^{-\alpha}$. In Fig. 1, we show a typical curve corresponding to the

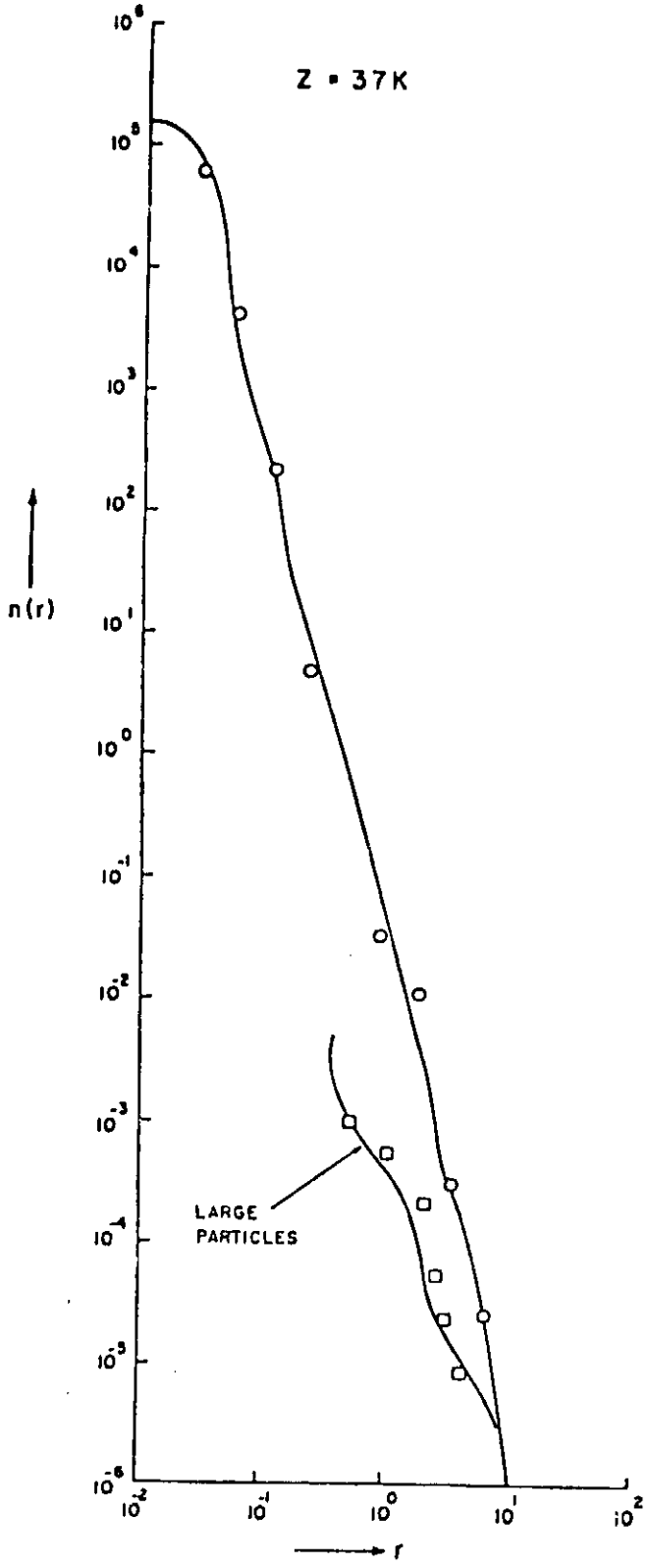

Fig. 1 Size distribution obtained by QCM at altitude z = 37,000 ft. Symbols represent the measured values.

altitude z = 37,000 feet as obtained directly by this method. In order to extract the values of optical parameters, two types of scaling have proven to be necessary:

(i) Conversion of the aerodynamic radius into geometric radius. This implies the substitution of Eq. (2)

$$r_i \rightarrow r_i' = r_i \ldots (2.0/\rho_p)^{\frac{1}{2}}$$

since the instrument was calibrated at ρ = 2.0.

(ii) Conversion of the 50% efficiency cut off radius into a geometric mean radius. This implies the rescaling

$$r_i' \rightarrow r_i'' = r_i\ (2.0)^{\frac{1}{2}}$$

In Table IV typical results referring to extinction and backscatter coefficients are shown.

B. Point-By-Point Power Law

Junge[6], has found that the size distribution of collected atmospheric aerosols can be represented by the power law

$$n(r) = Ar^{-\mu} \qquad (16)$$

On a log-log plot, having $\log_{10} r$ as its abscissa and $\log_{10} n(r)$ as ordinate, each pair of data points contained in Tables 1-3 is connected by a straight line, if the power law of the form given by Eq. (16) is assumed.

The same scaling procedure is discussed in previous subsection is still implied. In Tables 5.1-5.3 and Table 6 some typical results are collected.

IV. CONCLUDING REMARKS

The results presented in Tables 4 and Table 6 show that the least square curve fit and the point-by-point methods lead to substantially equivalent results with the accuracy 5 - 15%.

In the LSCF method, for a given density ρ_p, the quantities β_{ext}, $\beta(\pi)$, $\beta_{ext}/\beta(\pi)$ and $\beta_{ext}/N(.15)$ vary with the index of refraction. On the other hand, in the point-by-point method, both β_{ext} and $\beta_{ext}/N(.15)$ are highly insensitive of the refractive index.

Both methods show that the extinction co-efficient is smallest for z = 41,000 feet.

TABLE 4: Cummulative Size Distributions and Optical Properties of Aerosols Measured by the QCM Impactor (see Tables 1-3) Using Least Square Curve Fit of the Experimental Data Points

Z (ft)	Mass Density ρ_p (g/cm^3)	R. I. $m = m' - im''$	Cummulative Size Distributions			Optical Properties			
			$N(.15)$ (cm^{-3})	$N(.25)$ (cm^{-3})	$N(15)/N(.25)$	β_{ext} (km^{-1})	$\beta(\pi)$ $km^{-1}Sr^{-1}$	$\beta_{ext}/\beta(\pi)$	$\beta_{ext}/N(.15)$
37,000	1.76	1.42 - i(0.0)	0.17×10^{1}	0.29×10^{0}	5.90	0.5833×10^{-3}	0.2068×10^{-4}	0.1901×10^{2}	0.336×10^{1}
		1.50 - i(0.005)	0.17×10^{1}	0.29×10^{0}	5.90	0.6339×10^{-3}	0.3123×10^{-4}	0.2030×10^{2}	0.365×10^{1}
		1.52 - i(0.0)	0.17×10^{1}	0.29×10^{0}	5.90	0.6739×10^{-3}	0.5103×10^{-4}	0.1321×10^{2}	0.388×10^{1}
	2.00	1.42 - i(0.0)	0.11×10^{1}	0.19×10^{0}	5.74	0.4072×10^{-3}	0.2130×10^{-4}	0.1911×10^{2}	0.358×10^{1}
		1.50 - i(0.005)	0.11×10^{1}	0.19×10^{0}	5.74	0.4400×10^{-3}	0.2152×10^{-4}	0.2045×10^{2}	0.3875×10^{1}
		1.52 - i(0.0)	0.11×10^{1}	0.19×10^{0}	5.74	0.4671×10^{-3}	0.3556×10^{-4}	0.1314×10^{2}	0.411×10^{1}
41,000	1.76	1.42 - i(0.0)	0.33×10^{1}	0.70×10^{0}	4.74	0.1148×10^{-2}	0.4872×10^{-4}	0.2357×10^{2}	0.352×10^{1}
		1.50 - i(0.005)	0.33×10^{1}	0.70×10^{0}	4.74	0.1279×10^{-2}	0.5885×10^{-4}	0.2173×10^{2}	0.392×10^{1}
		1.52 - i(0.0)	0.33×10^{1}	0.70×10^{0}	4.74	0.1346×10^{-2}	0.9404×10^{-4}	0.1432×10^{2}	0.413×10^{1}

TABLE 5.1: Summary of Physical and Optical Characteristics of Aerosols Using QCM Impactor Measurements at Altitude 37,000 Feet

Size Distribution $n(r) = p_1 r^{-p_2}$; Refractive Index $m = 1.42 - i(0.0)$; Specific gravity $\rho_p = 1.76$

r_{min} (μm)	r_{max} (μm)	p_1	p_2	$A = \beta_{ext}(1.0)$ (km^{-1})	$B = \beta(\pi, 0.69)$ ($km^{-1} sr^{-1}$)	A/B (sr)
0.038	0.75	0.43×10^{-1}	3.90	0.333×10^{-5}	0.150×10^{-5}	
0.075	0.151	0.19×10^{-1}	4.22	0.238×10^{-4}	0.561×10^{-5}	
0.151	0.302	0.16×10^{-2}	5.51	0.643×10^{-4}	0.226×10^{-5}	
0.302	1.206	0.16×10^{-1}	3.58	0.271×10^{-3}	0.591×10^{-5}	
1.206	2.412	0.11×10^{-1}	1.68	0.124×10^{-3}	0.859×10^{-5}	
2.412	4.824	0.22×10^{0}	5.05	0.936×10^{-4}	0.554×10^{-5}	
4.824	9.648	0.21×10^{-1}	3.56	0.344×10^{-4}	0.409×10^{-5}	
0.038	9.648			0.6146×10^{-3}	0.3350×10^{-4}	0.183×10^{2}

$N(.15) = 0.193 \times 10^{1}\ cm^{-3}$; $N(.25) = 0.249 \times 10^{0}\ cm^{-3}$; $N(.15)/N(.25) = 0.773 \times 10^{1}$

$\beta_{ext}(1.0)/N(.15) = 0.319 \times 10^{1}\ cm^{2}$

TABLE 5.2: Summary of Physical and Optical Characteristics of Aerosols Using QCM Impactor Measurements at Altitude 41,000 feet

Size Distribution $n(r) = p_1 r^{-p_2}$; Refractive Index $m = 1.42 - i(0.0)$; Specific gravity $\rho_p = 1.76$

r_{min} (μm)	r_{max} (μm)	p_1	p_2	$A = \beta_{ext}(1.0)$ (km^{-1})	$B = \beta(\pi, 0.69)$ ($km^{-1}; sr^{-1}$)	A/B (sr)
0.038	0.075	0.65×10^{-1}	3.84	0.428×10^{-5}	0.193×10^{-5}	
0.075	0.151	0.12×10^{-1}	4.49	0.275×10^{-4}	0.660×10^{-5}	
0.151	0.302	0.37×10^{-1}	3.89	0.132×10^{-3}	0.450×10^{-5}	
0.302	1.206	0.37×10^{-1}	3.89	0.724×10^{-3}	0.156×10^{-4}	
1.206	2.412	0.31×10^{-1}	2.96	0.161×10^{-3}	0.113×10^{-4}	
2.412	4.824	0.11×10^{0}	4.36	0.101×10^{-3}	0.617×10^{-5}	
4.824	9.648	0.43×10^{-1}	3.78	0.456×10^{-4}	0.541×10^{-5}	
0.038	9.648			0.1194×10^{-2}	0.5149×10^{-4}	0.232×10^{2}

$N(.15) = 0.311 \times 10^{1}$ cm^{-3}; $N(.25) = 0.713 \times 10^{0}$ cm^{-3}; $N(.15)/N(.25) = 0.437 \times 10^{1}$

$\beta_{ext}(1.0)/N(.15) = 0.384 \times 10^{1}$ cm^{2}

TABLE 5.3: Summary of Physical and Optical Characteristics of Aerosols Using QCM Impactor Measurements at Altitude 43,000 Feet

Size Distribution $n(r) = p_1 r^{-p_2}$; Refractive Index $m = 1.42 - i(0.0)$; Specific gravity $\rho_p = 1.76$

r_{min} (μm)	r_{max} (μm)	p_1	p_2	$A = \beta_{ext}(1.0)$ (km^{-1})	$B = \beta(\pi, 0.69)$ ($km^{-1} sr^{-1}$)	A/B (sr)
0.151	0.302	0.82×10^{-2}	4.93	0.136×10^{-3}	0.472×10^{-5}	
0.302	1.206	0.21×10^{-1}	4.15	0.470×10^{-3}	0.101×10^{-4}	
1.206	2.412	0.12×10^{-1}	1.30	0.170×10^{-3}	0.117×10^{-4}	
2.412	4.824	0.37×10^{0}	5.15	0.138×10^{-3}	0.812×10^{-5}	
4.824	9.648	0.15×10^{0}	4.58	0.356×10^{-4}	0.416×10^{-5}	
0.151	9.648			0.9499×10^{-3}	0.3875×10^{-4}	0.245

$N(.15) = 0.362 \times 10^{1}$ cm^{-3}; $N(.25) = 0.552 \times 10^{0}$ cm^{-3}; $N(.15)/N(.25) = 0.657 \times 10^{1}$

$\beta_{ext}(1.0)/N(.15) = 0.262 \times 10^{1}$ cm^{2}

TABLE 6: Summary of Cumulative Size Distributions and Optical Properties of Aerosols Measured by the QCM Impactor (see Tables 1-3) Using Point-By-Point

Z (ft)	Mass Density ρ_p (g/cm^3)	R. I. $m = m' - im''$	Cumulative Size Distributions			Optical Properties			
			$N(.15)$ (cm^{-3})	$N(.25)$ (cm^{-3})	$N(.15)/N(.25)$	β_{ext} (km^{-1})	$\beta(\pi)$ $km^{-1}\ Sr^{-1}$	$\beta_{ext}/\beta(\pi)$	$\beta_{ext}/N(.15)$
37,000	1.76	1.42 - i(0.0)	0.193×10^{1}	0.249×10^{0}	7.73	0.6146×10^{-3}	0.3350×10^{-4}	0.183×10^{2}	0.319×10^{1}
		1.50 - i(0.005)	0.193×10^{1}	0.249×10^{0}	7.73	0.6146×10^{-3}	0.3176×10^{-4}	0.134×10^{2}	0.319×10^{1}
		1.52 - i(0.0)	0.193×10^{1}	0.249×10^{0}	7.73	0.6146×10^{-3}	0.5179×10^{-4}	0.119×10^{2}	0.319×10^{1}
	2.00	1.42 - i(0.0)	0.120×10^{1}	0.167×10^{0}	7.21	0.4272×10^{-3}	0.2378×10^{-4}	0.180×10^{2}	0.355×10^{1}
		1.50 - i(0.005)	0.120×10^{1}	0.167×10^{0}	7.21	0.4272×10^{-3}	0.2186×10^{-4}	0.195×10^{2}	0.355×10^{1}
		1.52 - i(0.0)	0.120×10^{1}	0.167×10^{0}	7.21	0.4272×10^{-3}	0.3514×10^{-4}	0.122×10^{2}	0.355×10^{1}
41,000	1.76	1.42 - i(0.0)	0.311×10^{1}	0.713×10^{0}	4.37	0.1194×10^{-2}	0.5874×10^{-4}	0.203×10^{2}	0.384×10^{1}
		1.50 - i(0.005)	0.311×10^{1}	0.713×10^{0}	4.37	0.1194×10^{-2}	0.5874×10^{-4}	0.203×10^{2}	0.384×10^{1}
		1.52 - i(0.0)	0.311×10^{1}	0.713×10^{0}	4.37	0.1194×10^{-2}	0.9344×10^{-4}	0.128×10^{2}	0.384×10^{1}

REFERENCES

1. V. A. Marple and K. Willeke, Inertial Impactors: Theory, Design and Use in Fine Particles: Aerosol Generation Measurement, Sampling and Analysis, edited by B. Y. Liu (Academic Press, New York, 1976), pp. 411-416.

2. S. K. Friedlander, Smoke, Dust and Haze; Fundamentals of Aerosol Behavior (Wiley, New York, 1977), pp. 162-164.

3. D. Wallace and R. Chuan, A. Cascade Impaction Instrument Using Quartz Crystal Microbalance Sensing Elements for Read Time Particle Size Distribution Studies, presented at 8th Materials Research Symposium, sponsored by N.B.S., Sept. 20-24, 1976.

4. D. C. Woods, Rocket Effluent Size Distributions Made with a Cascade Quartz Crystal Microbalance, presented at the 4th Joint Conference on Sensing of Environmental Pollutants, New Orleans, Nov. 7-11, 1977.

5. D. Deirmendjian, Electromagnetic Scattering on Spherical Polydispersions (Elsevier, New York, 1969).

6. M. P. McCormick and J. D. Lawrence, Jr., Tables of Mie Scattering Functions for Particles with Refractive Index 1.5, NASA TN D-5110, 1969.

APPENDIX 2

CONTOUR PLOTS FOR INDIVIDUAL SAGE POLE-TO-POLE MOVEMENTS FOR THE PERIOD

FEBRUARY 21, 1979 - DECEMBER 13, 1980

APPENDIX 2.1 AEROSOL EXTINCTION PLOTS

EXTINCTIØN

AVERAGES FØR Feb. 21 - Mar. 21 , 1979

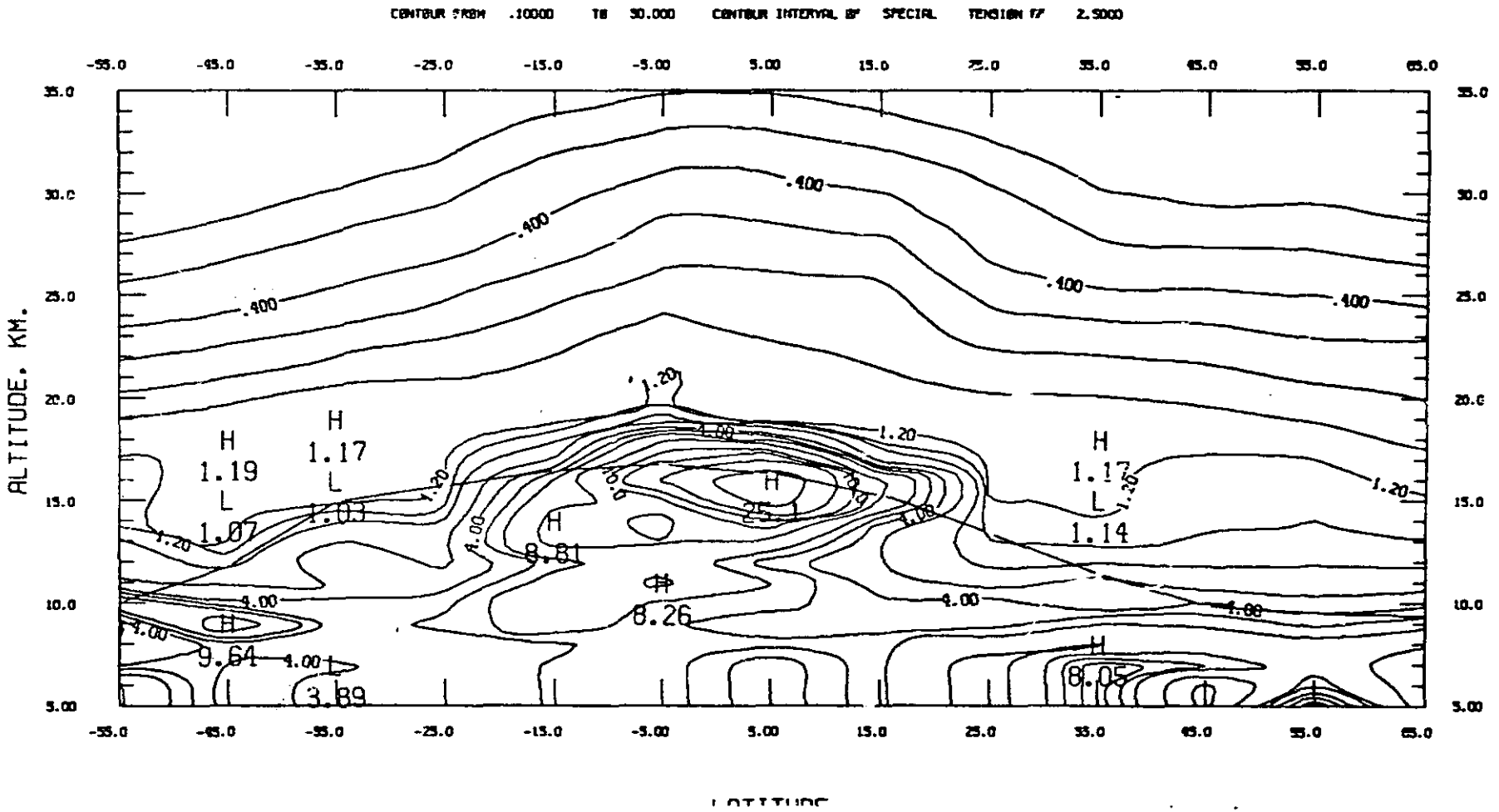

EXTINCTIØN

AVERAGES FØR Mar. 22 - Apr. 28 , 1979

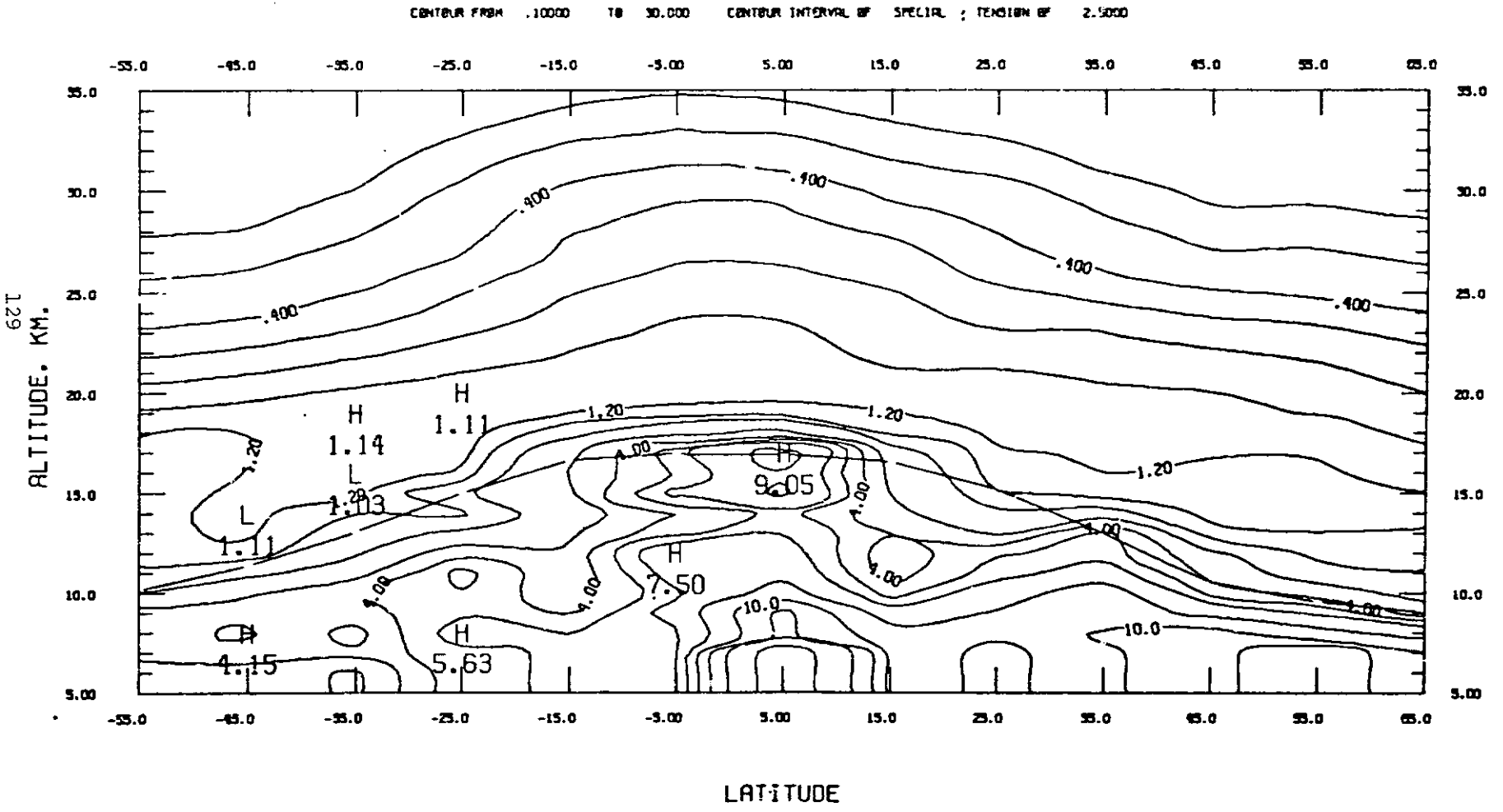

EXTINCTIØN

AVERAGES FØR Apr. 29 - May 29 , 1979

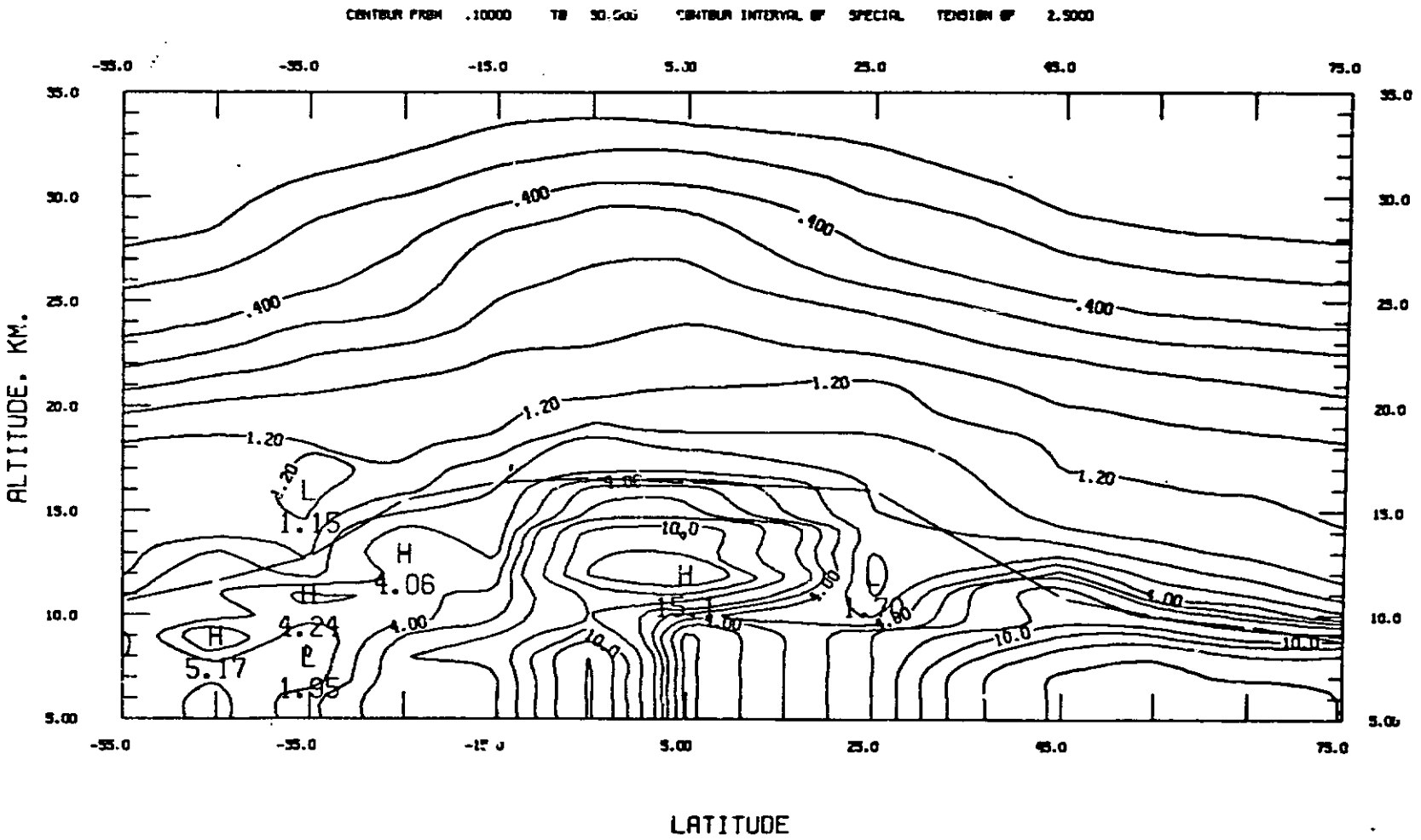

130

EXTINCTIØN

AVERAGES FØR June 1 - Aug. 6, 1979

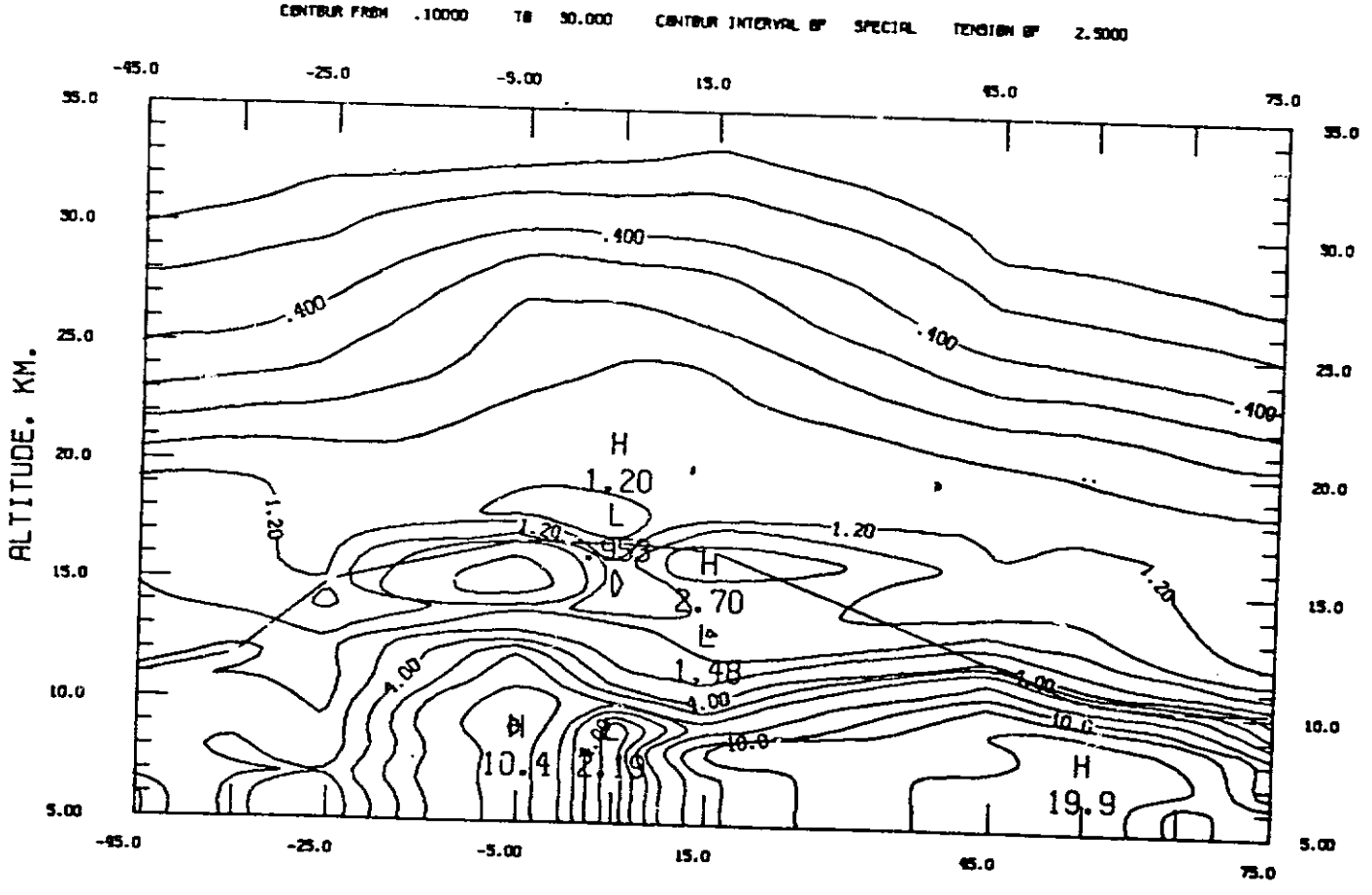

EXTINCTIØN

AVERAGES FØR Aug. 7 - Sept. 13, 1979

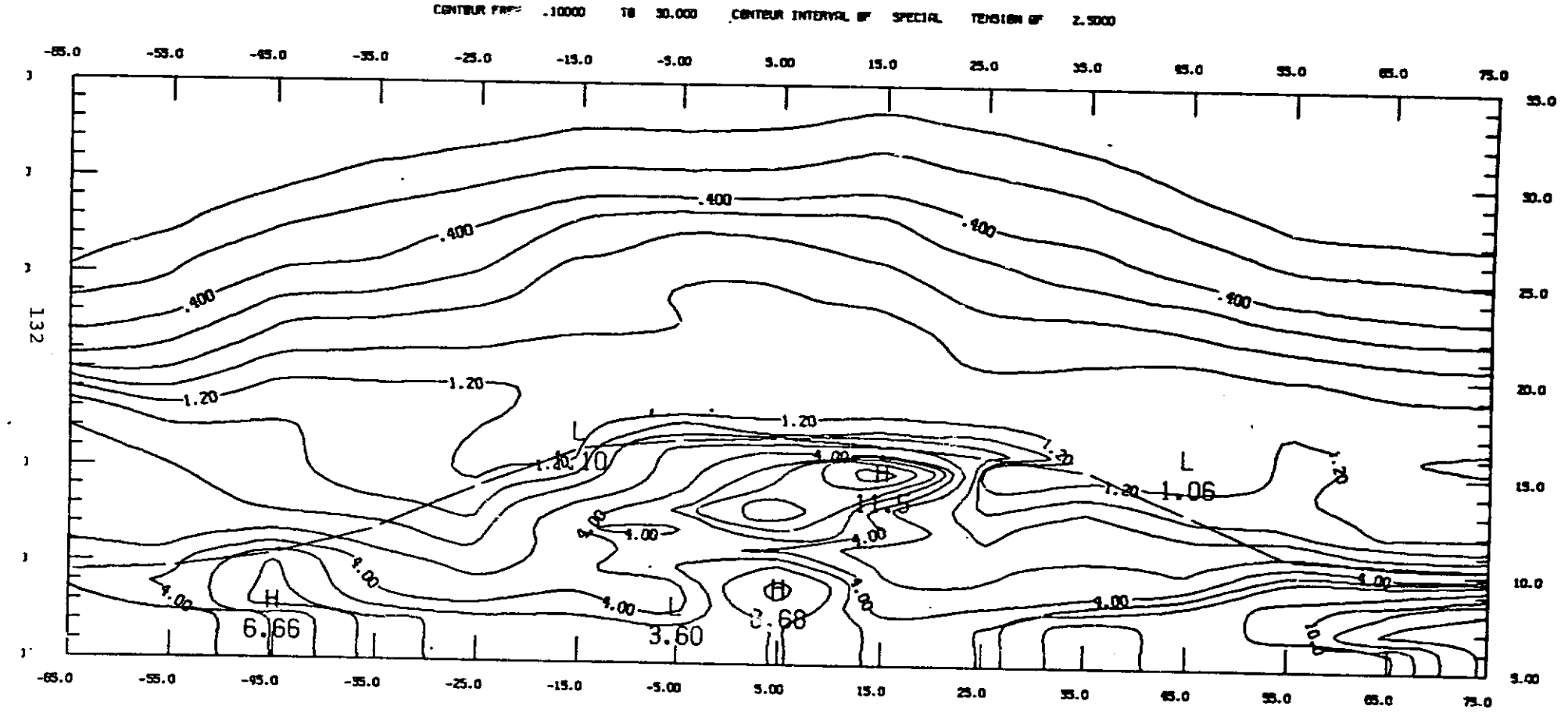

LATITUDE

EXTINCTION

AVERAGES FOR Sept. 14 - Oct. 20, 1979

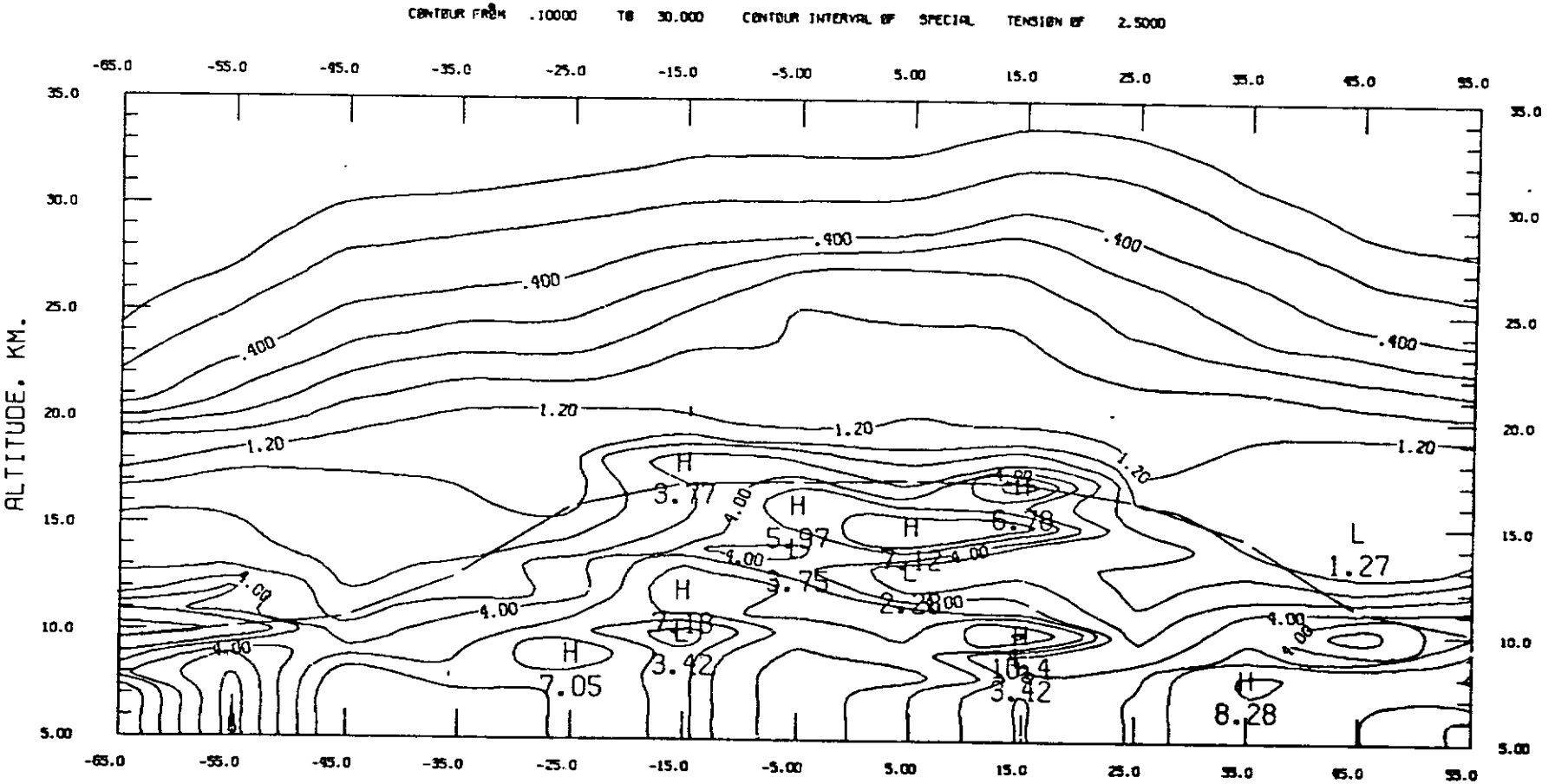

EXTINCTIØN

AVERAGES FØR Oct. 21 - Nov. 21, 1979

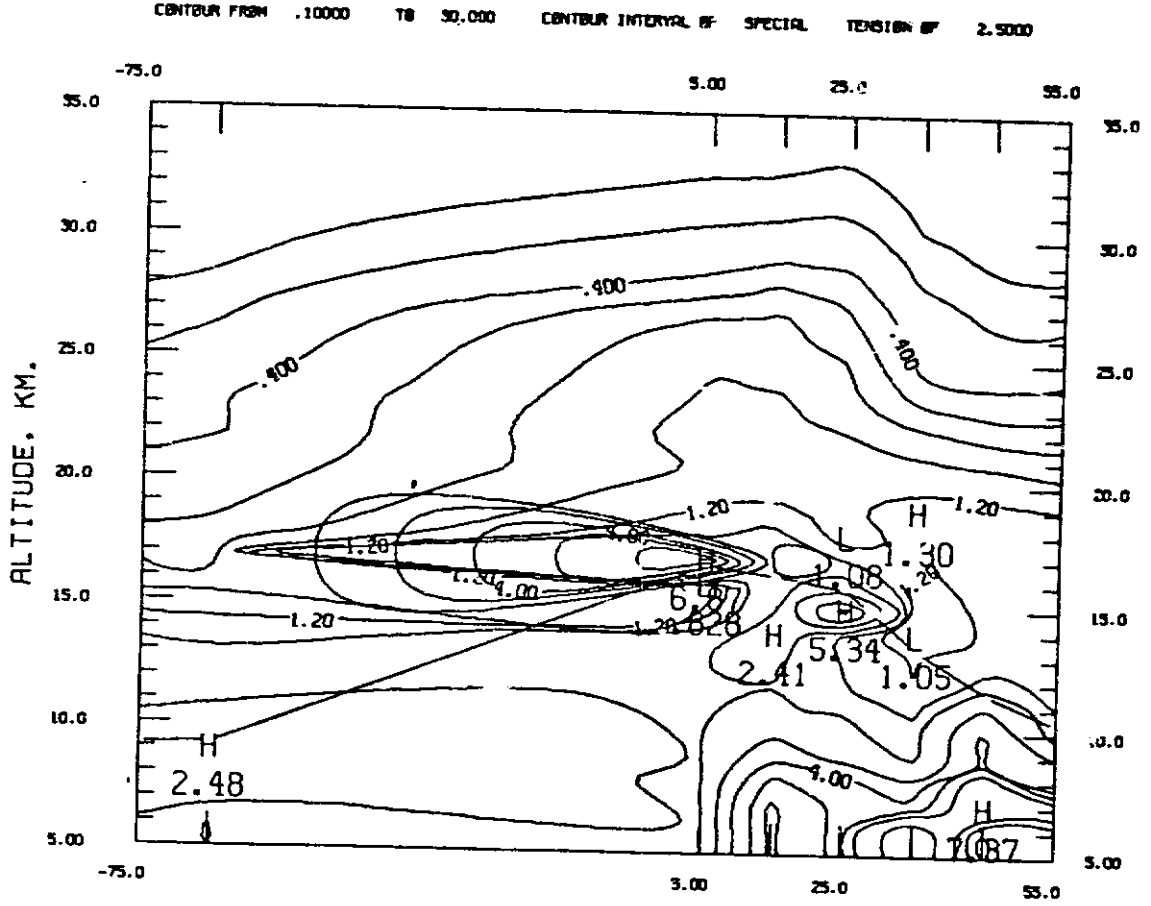

LATITUDE

EXTINCTIØN

AVERAGES FØR Nov. 22 - Dec. 31, 1979

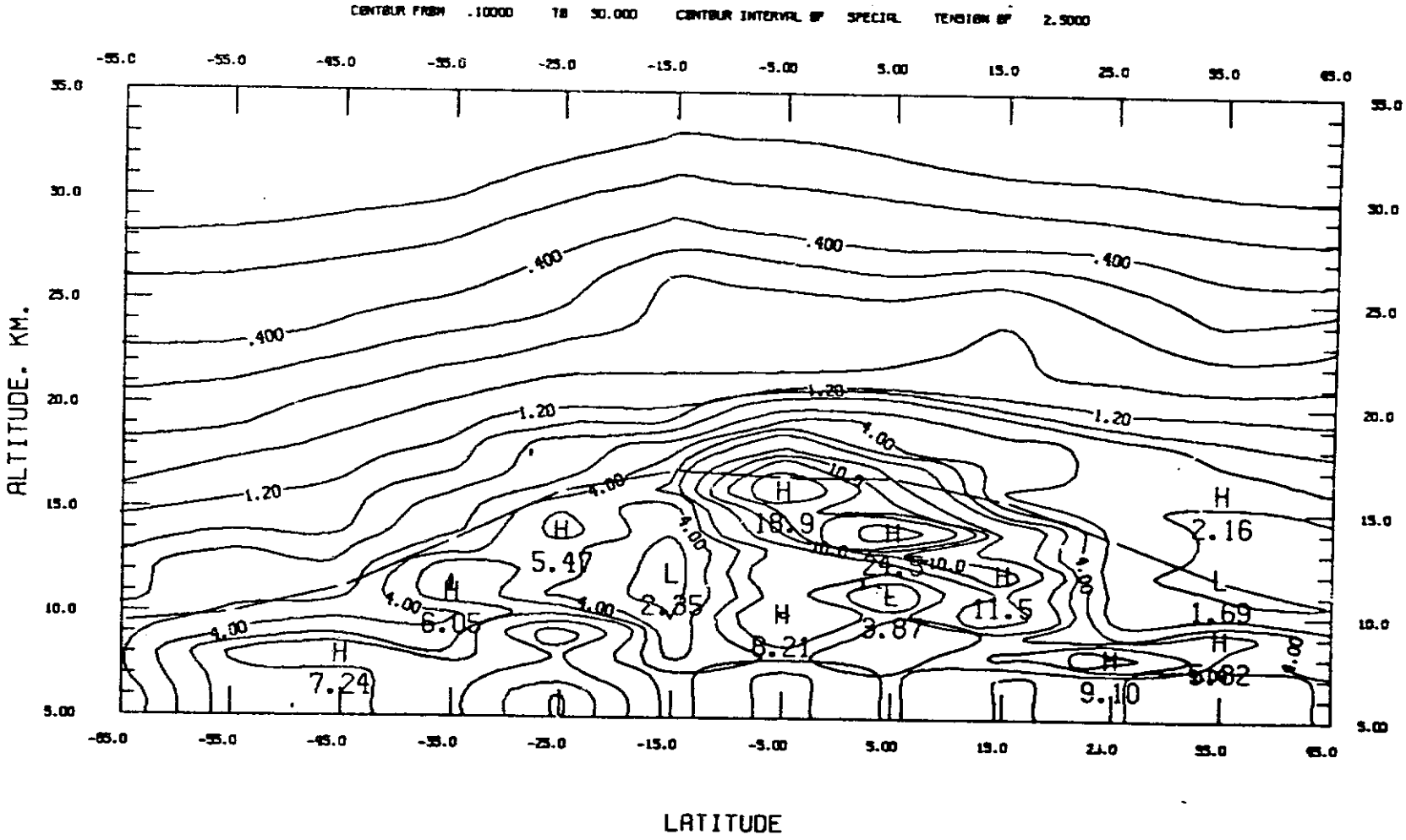

EXTINCTIØN

AVERAGES FØR Jan. 1 - Jan. 26 , 1980

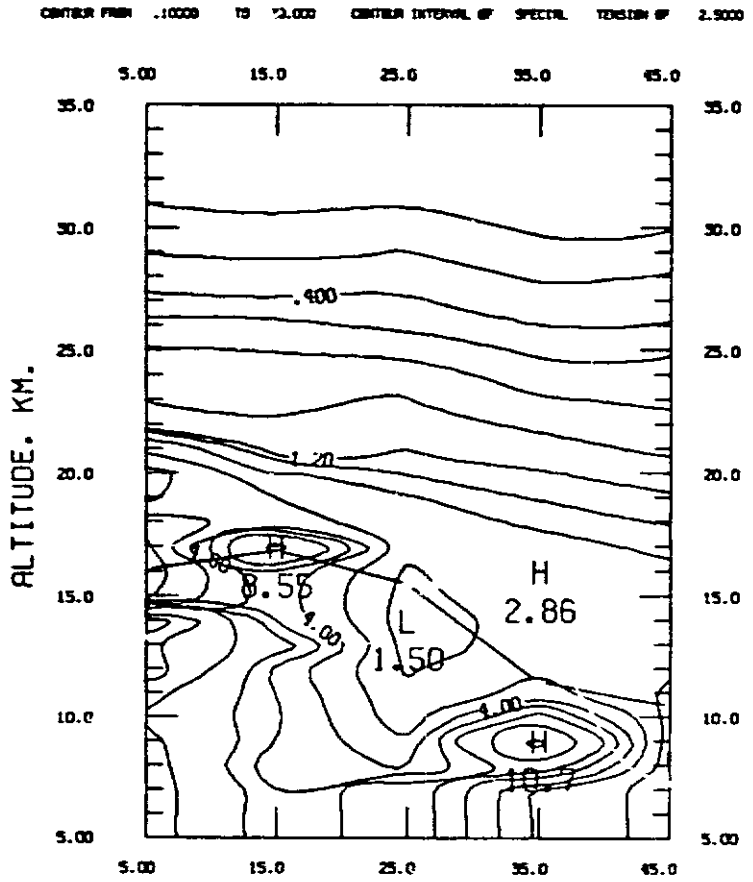

EXTINCTION

AVERAGES FOR Jan. 27 - Mar. 6, 1980

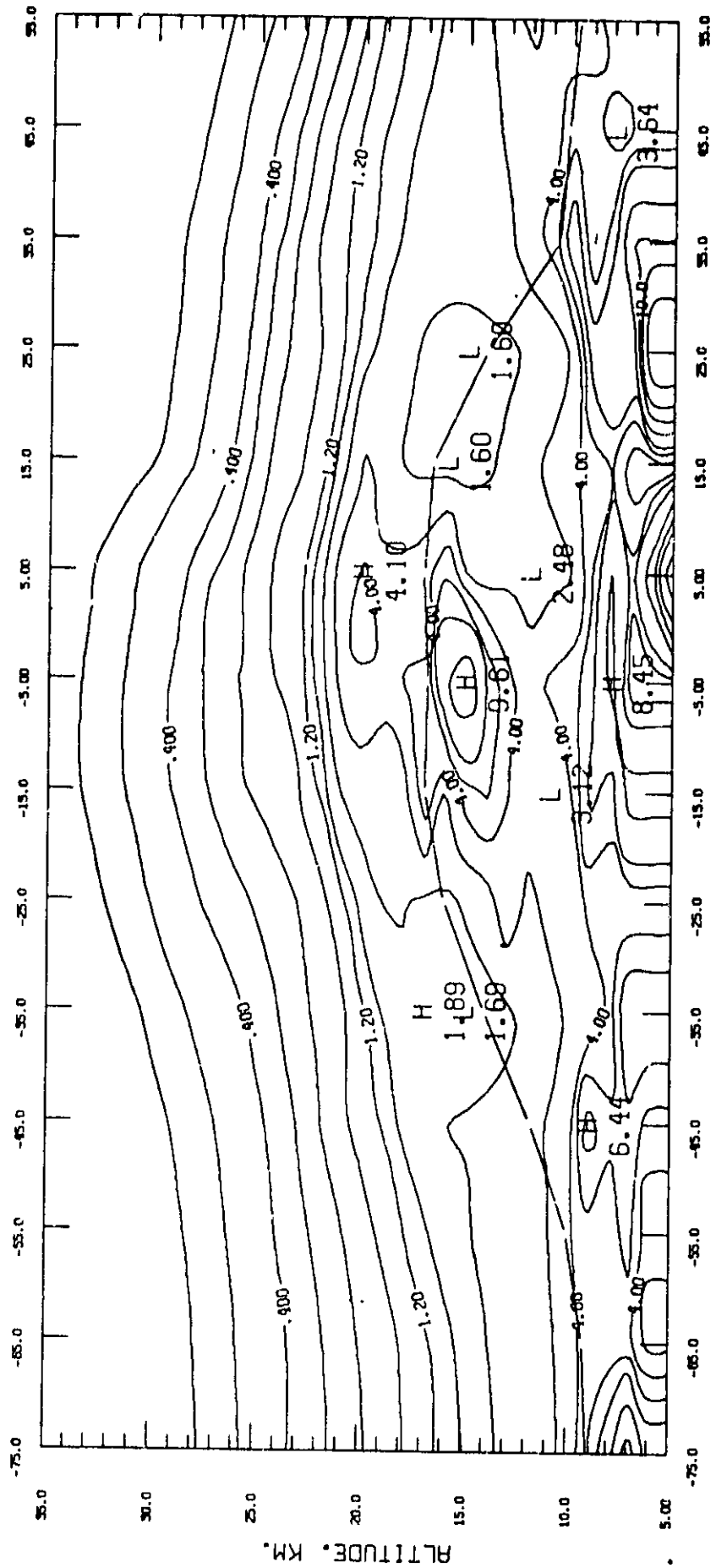

EXTINCTIØN

AVERAGES FØR Mar. 7 - Mar. 29 , 1980

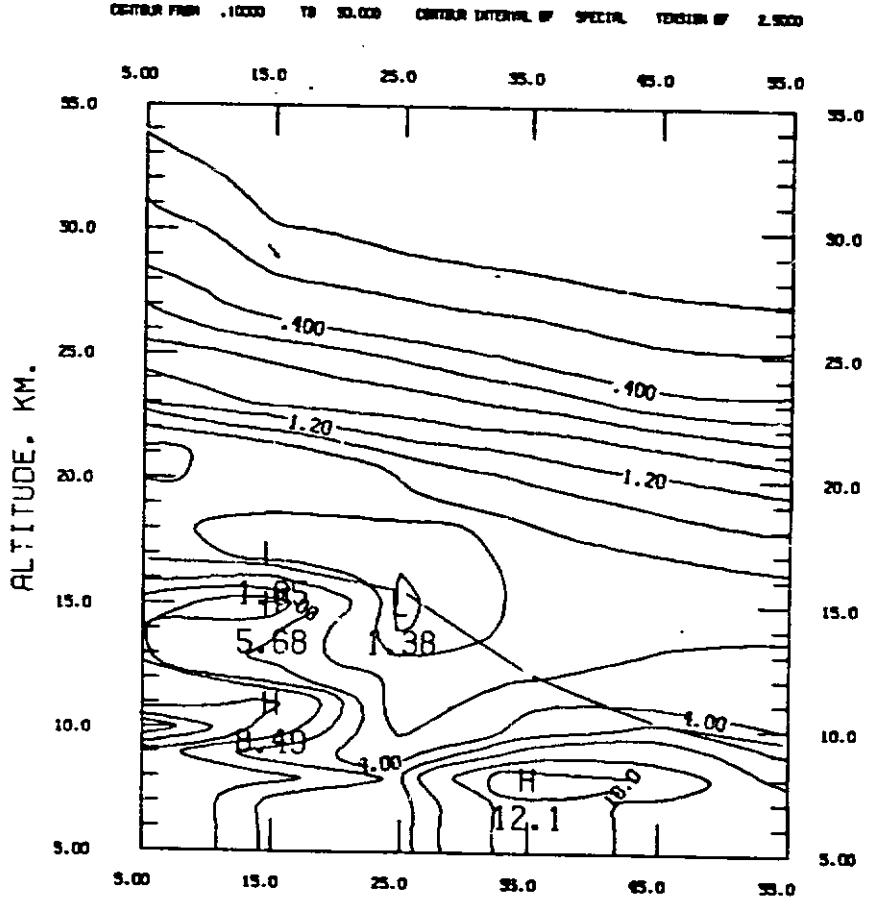

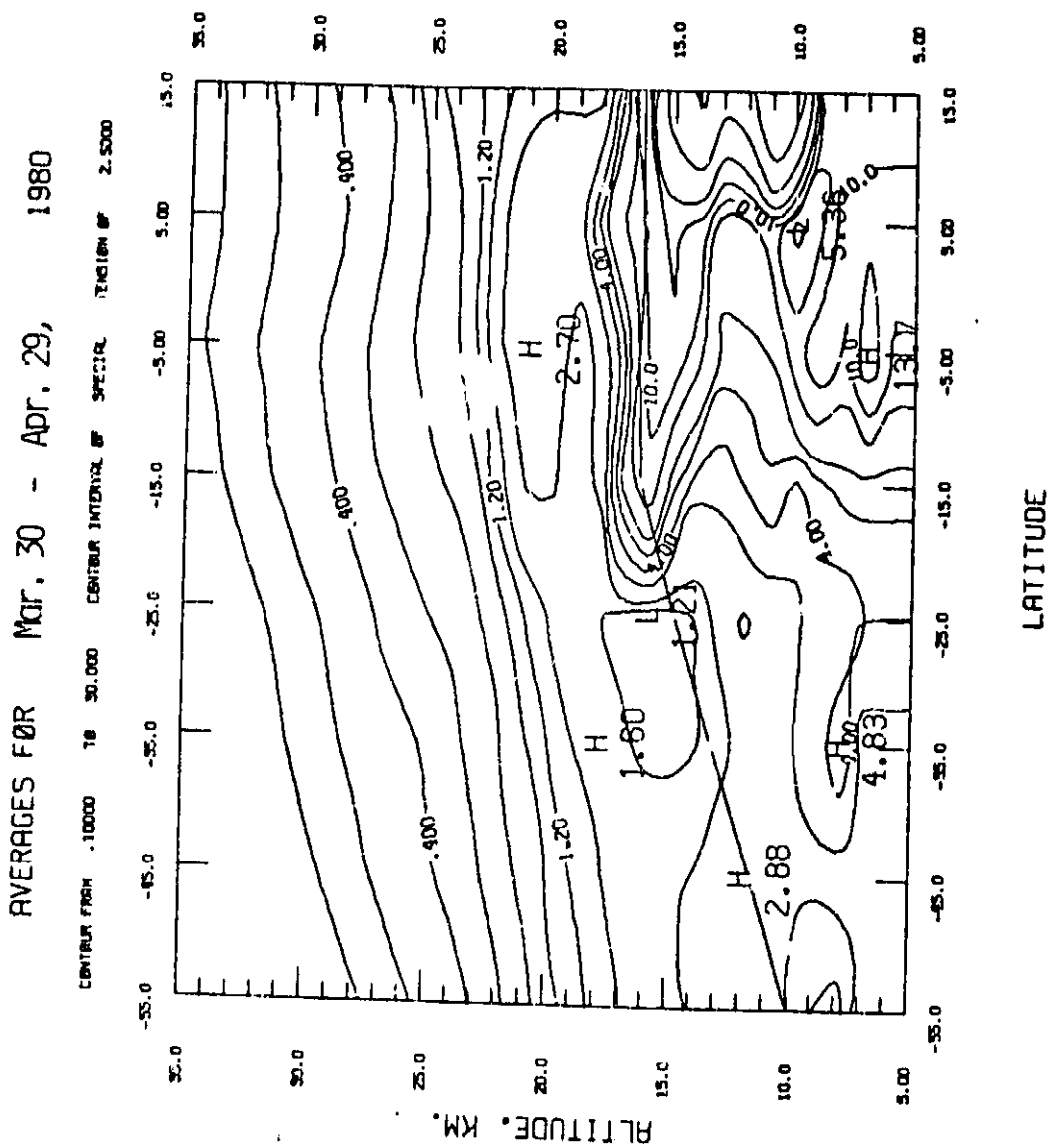

EXTINCTIØN

AVERAGES FØR May 12 - June 23, 1980

(All Longitudes)

CONTOUR FROM .10000 TO 30.000 CONTOUR INTERVAL OF SPECIAL TENSION OF 2.5000

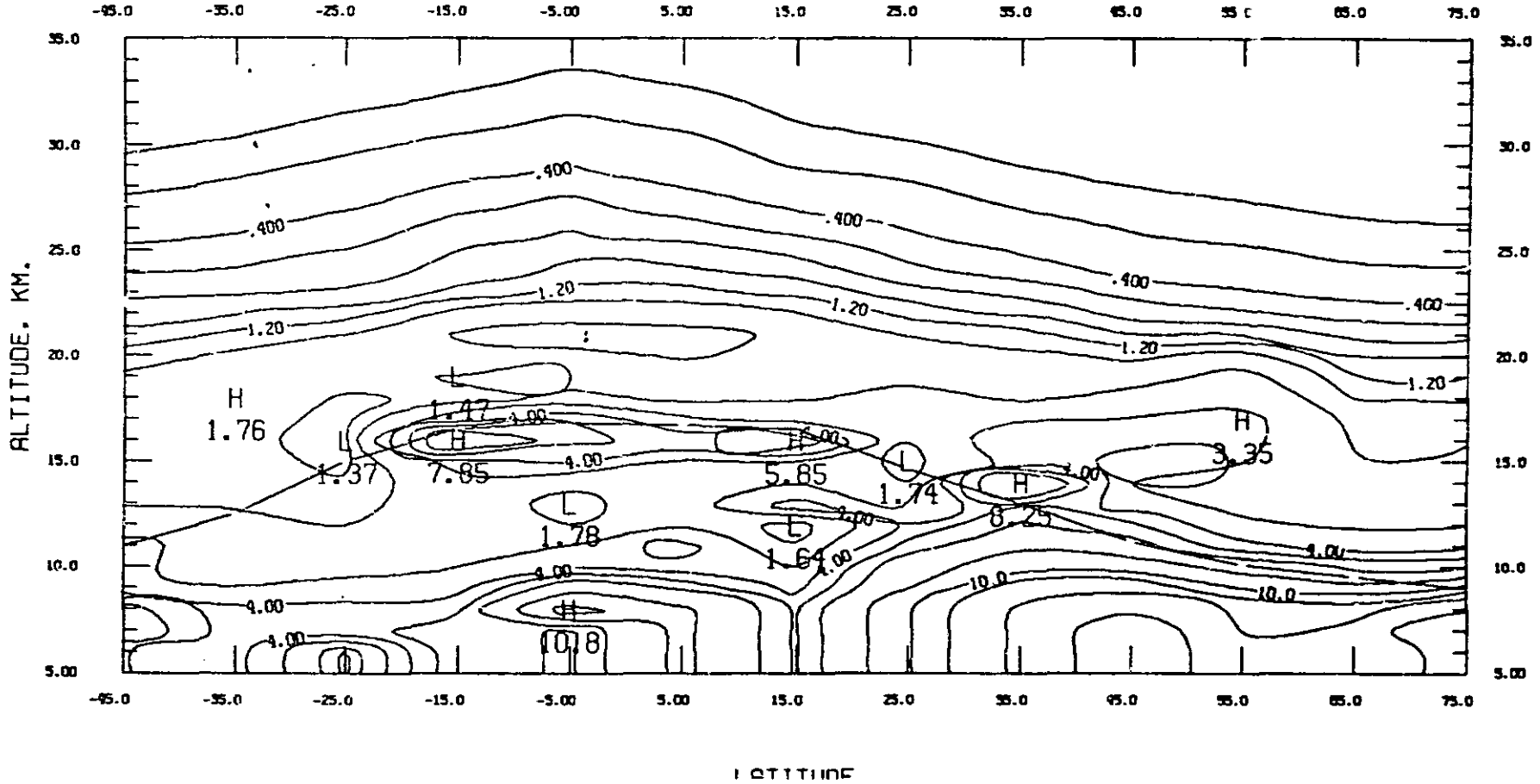

EXTINCTIØN

AVERAGES FØR May 12 - June 23, 1980

(Longitudes 0 → +180)

CONTOUR FROM .10000 TO 50.000 CONTOUR INTERVAL OF SPECIAL TENSION OF 2.5000

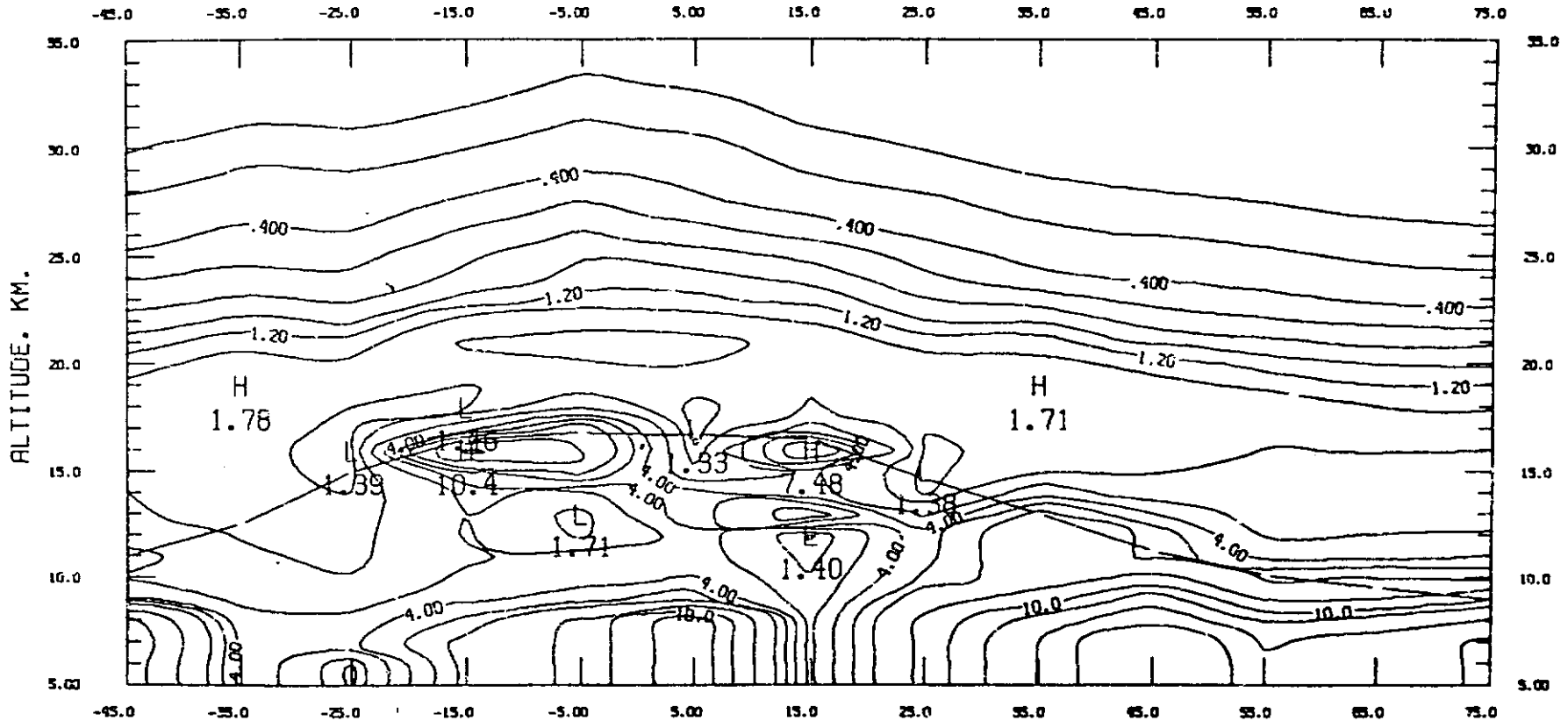

ALTITUDE, KM.

LATITUDE

141

EXTINCTIØN

AVERAGES FØR June 24 - July 20 , 1980

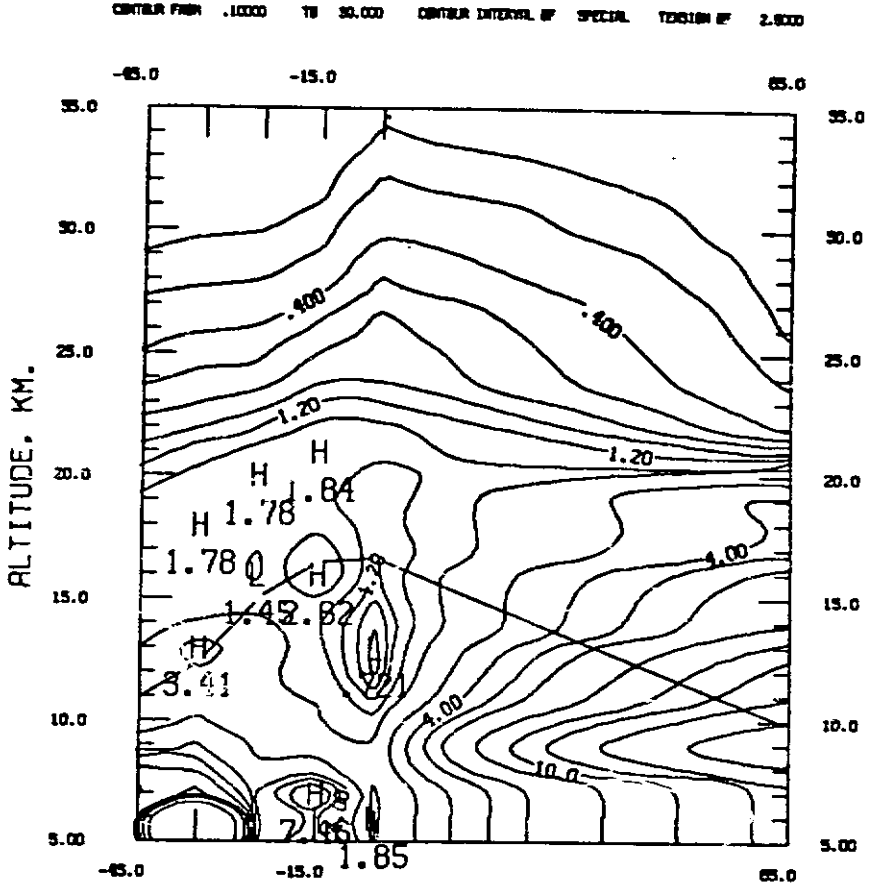

EXTINCTIØN

AVERAGES FØR July 21 - Aug. 26 , 1980

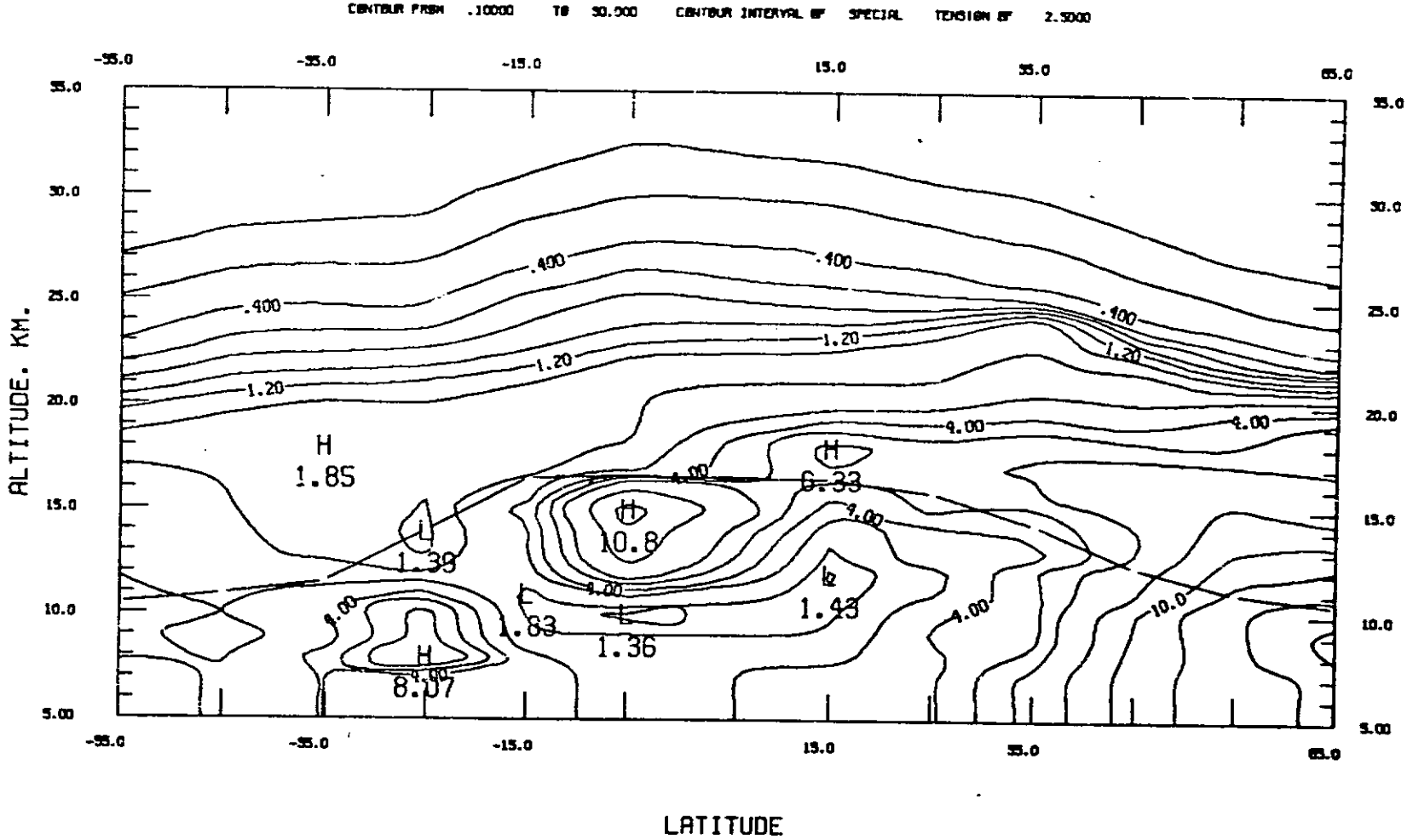

EXTINCTIØN ·

AVERAGES FØR Aug. 29 - Sept. 25 , 1980

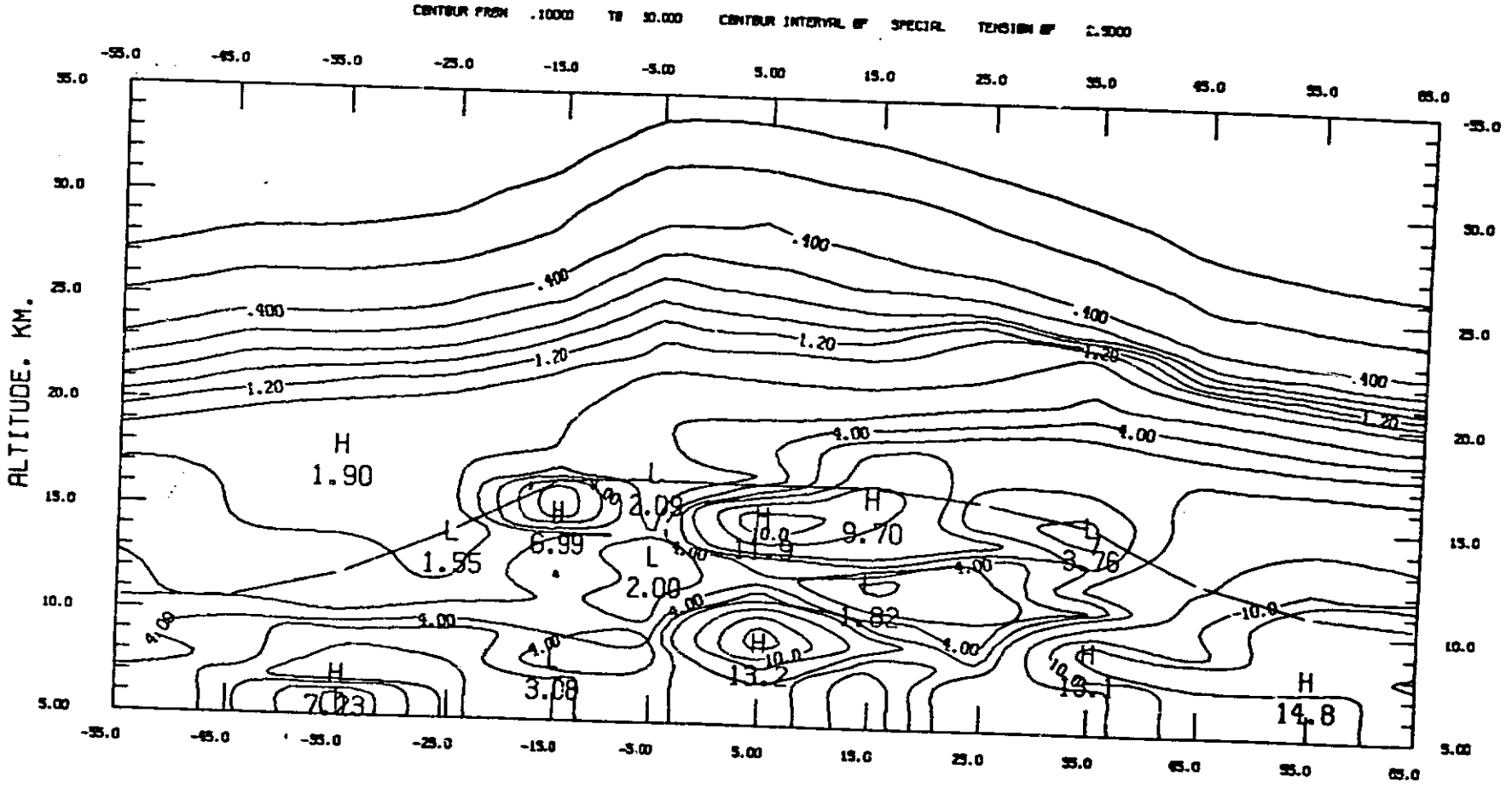

EXTINCTIØN .

AVERAGES FØR Sept. 26 - Oct. 31 , 1980
(All Longitudes)

CONTOUR FROM .10000 TO 30.000 CONTOUR INTERVAL BY SPECIAL TENSION BY 2.5000

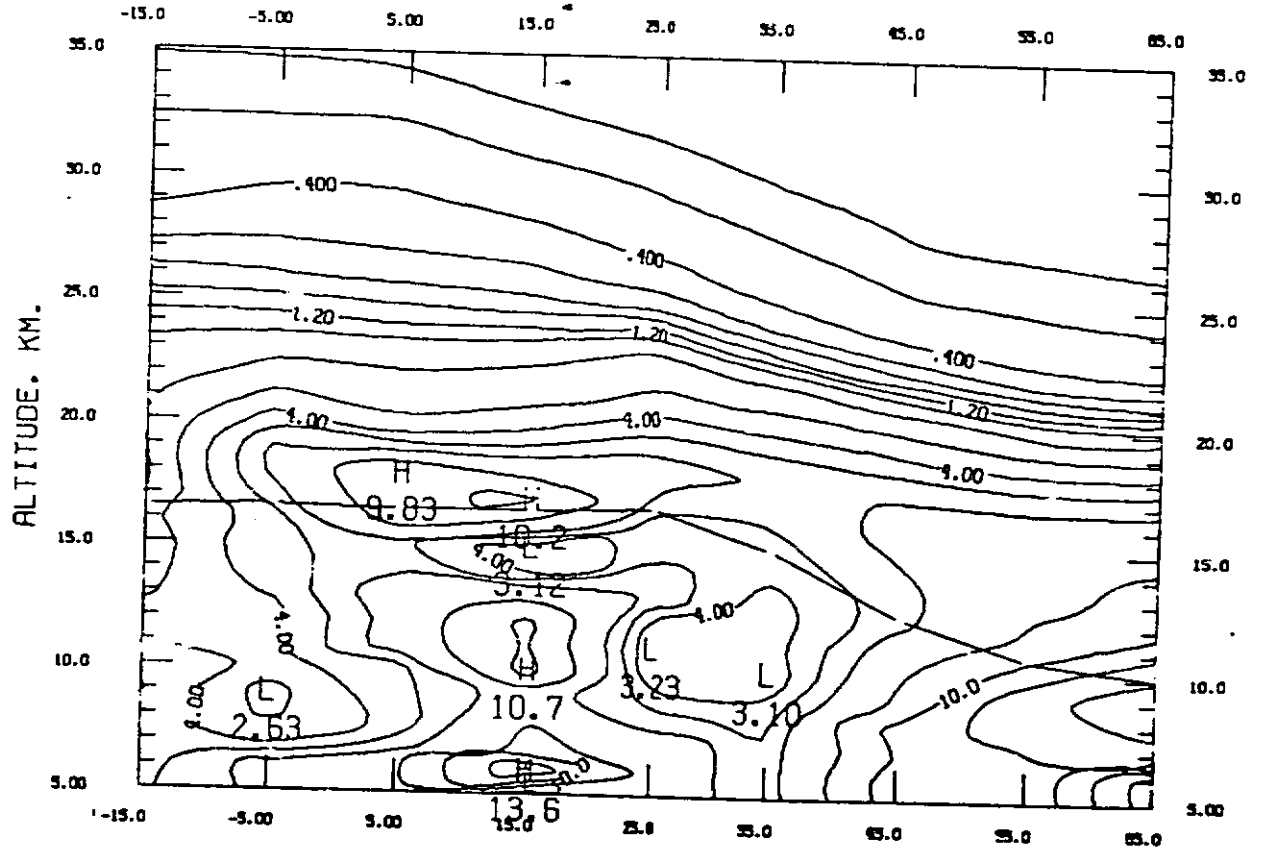

ALTITUDE, KM.

LATITUDE

EXTINCTIØN

AVERAGES FØR Sept. 26 - Oct. 31, 1980

(-90° → +90°)

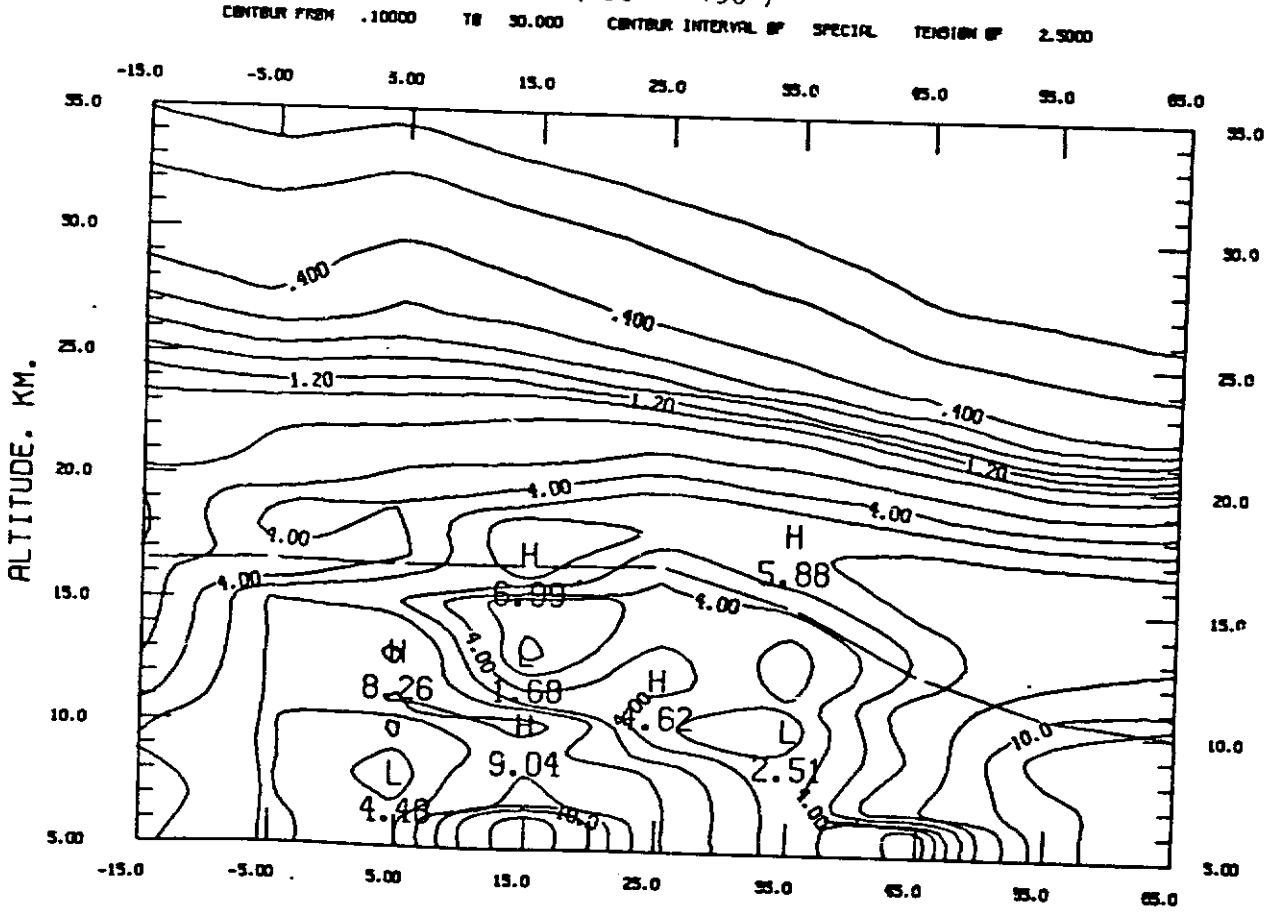

EXTINCTION

AVERAGES FOR Nov. 1 - Dec. 13, 1980

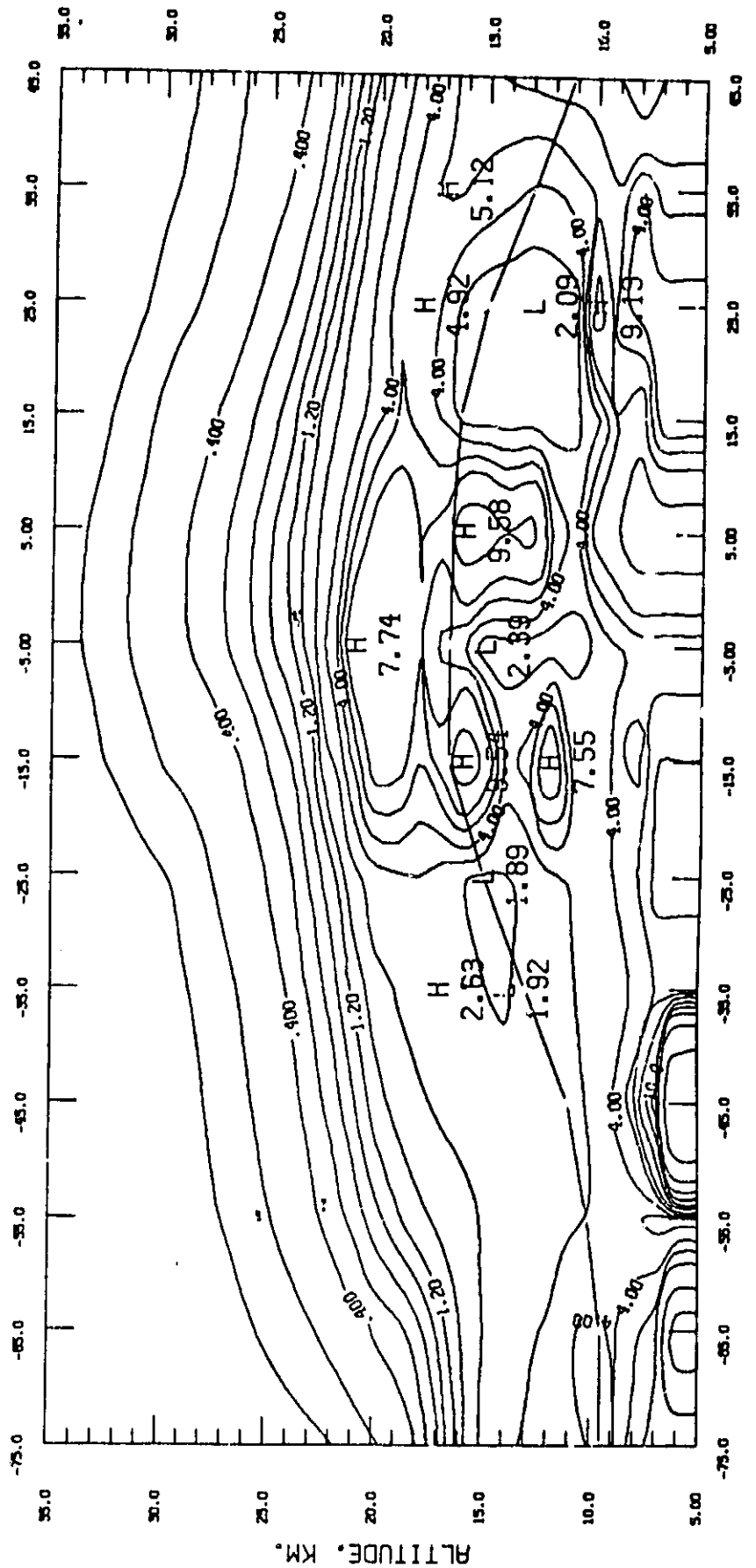

APPENDIX 2.2 AEROSOL EXTINCTION RATIO PLOTS

EXTINCTIØN RATIØ

AVERAGES FØR Feb. 21 - Mar. 21, 1979

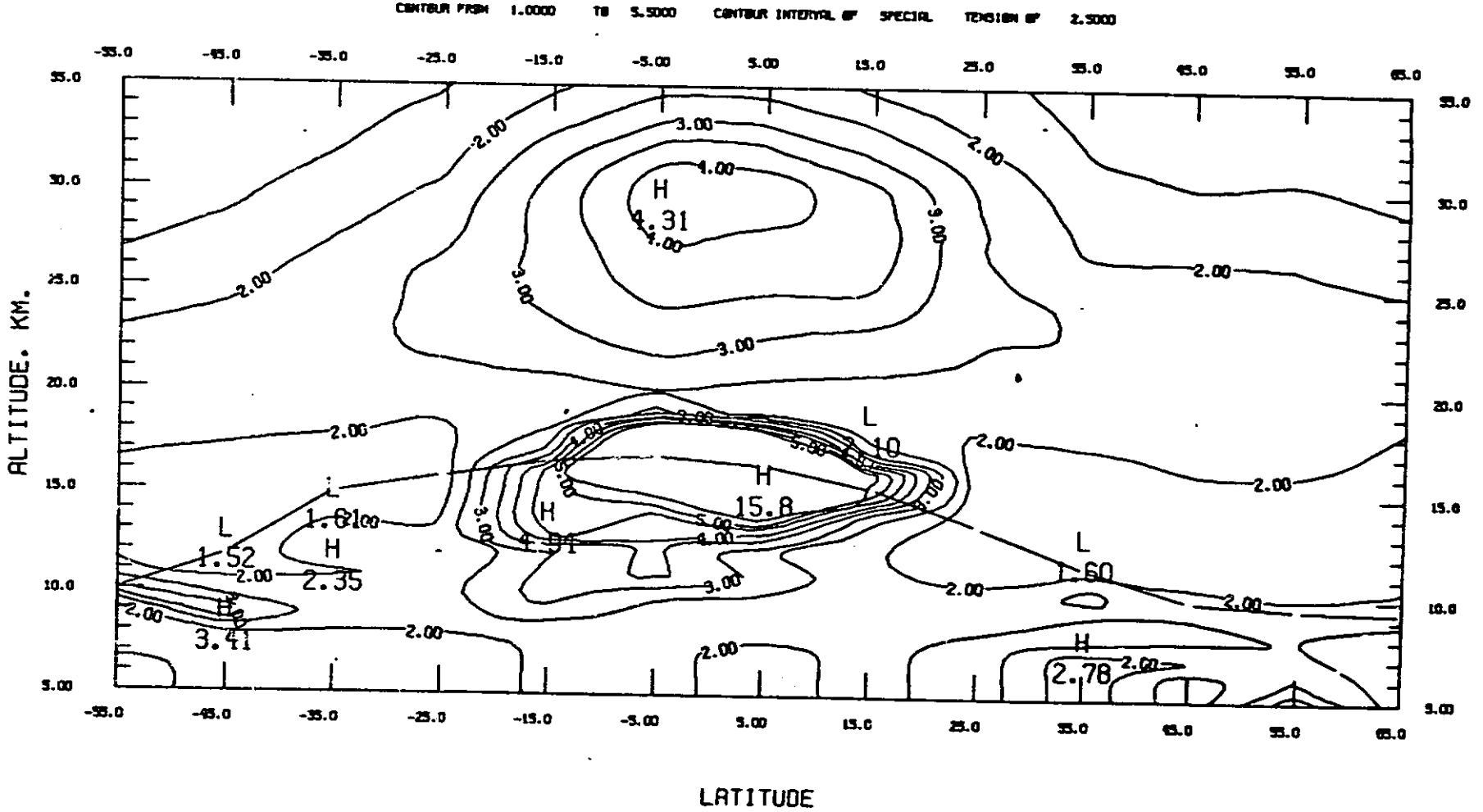

150

EXTINCTIØN RATIØ

AVERAGES FØR Mar. 22 - Apr. 28, 1979

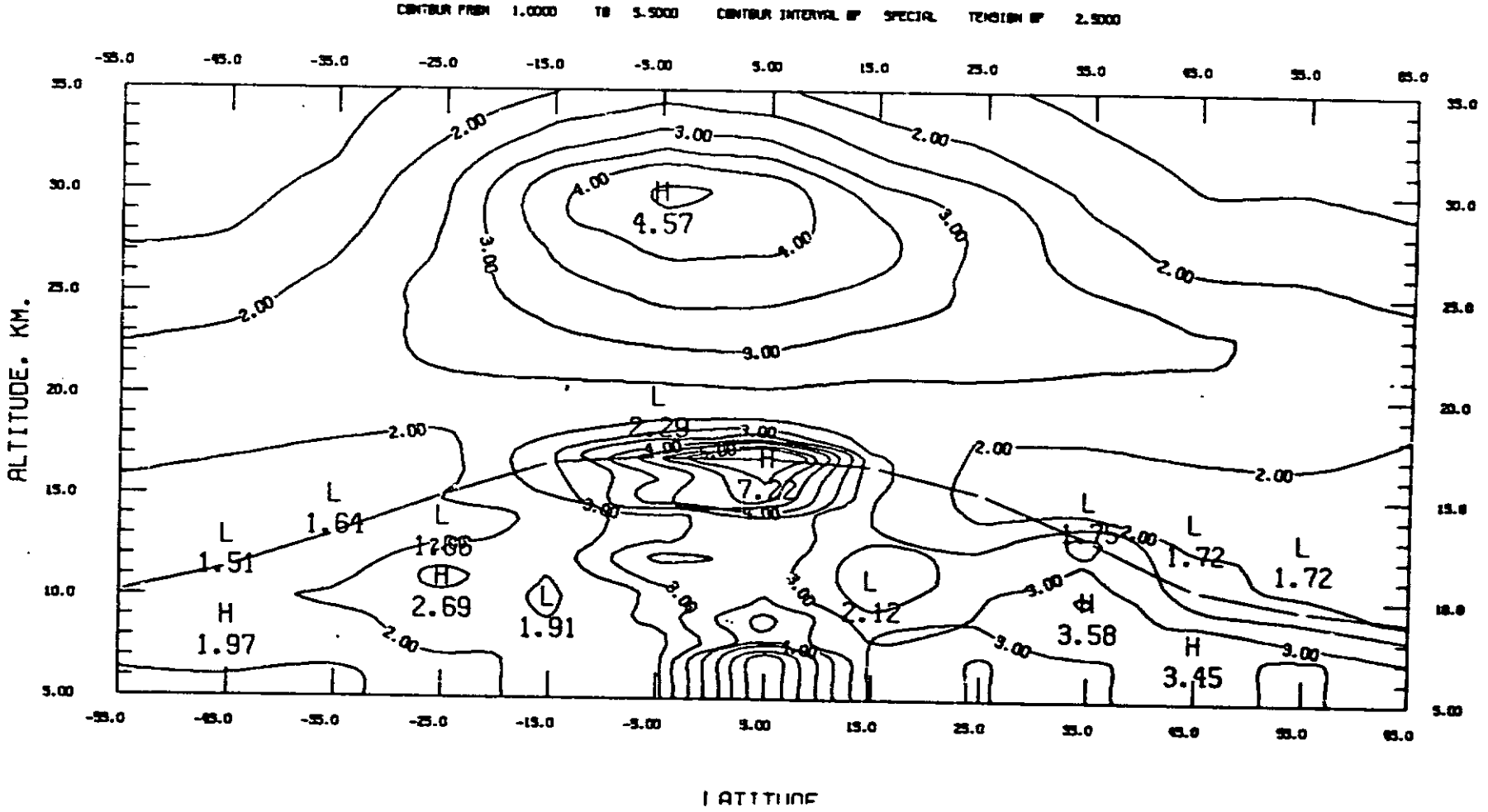

EXTINCTIØN RATIØ

AVERAGES FØR Apr. 29 - May 29, 1979

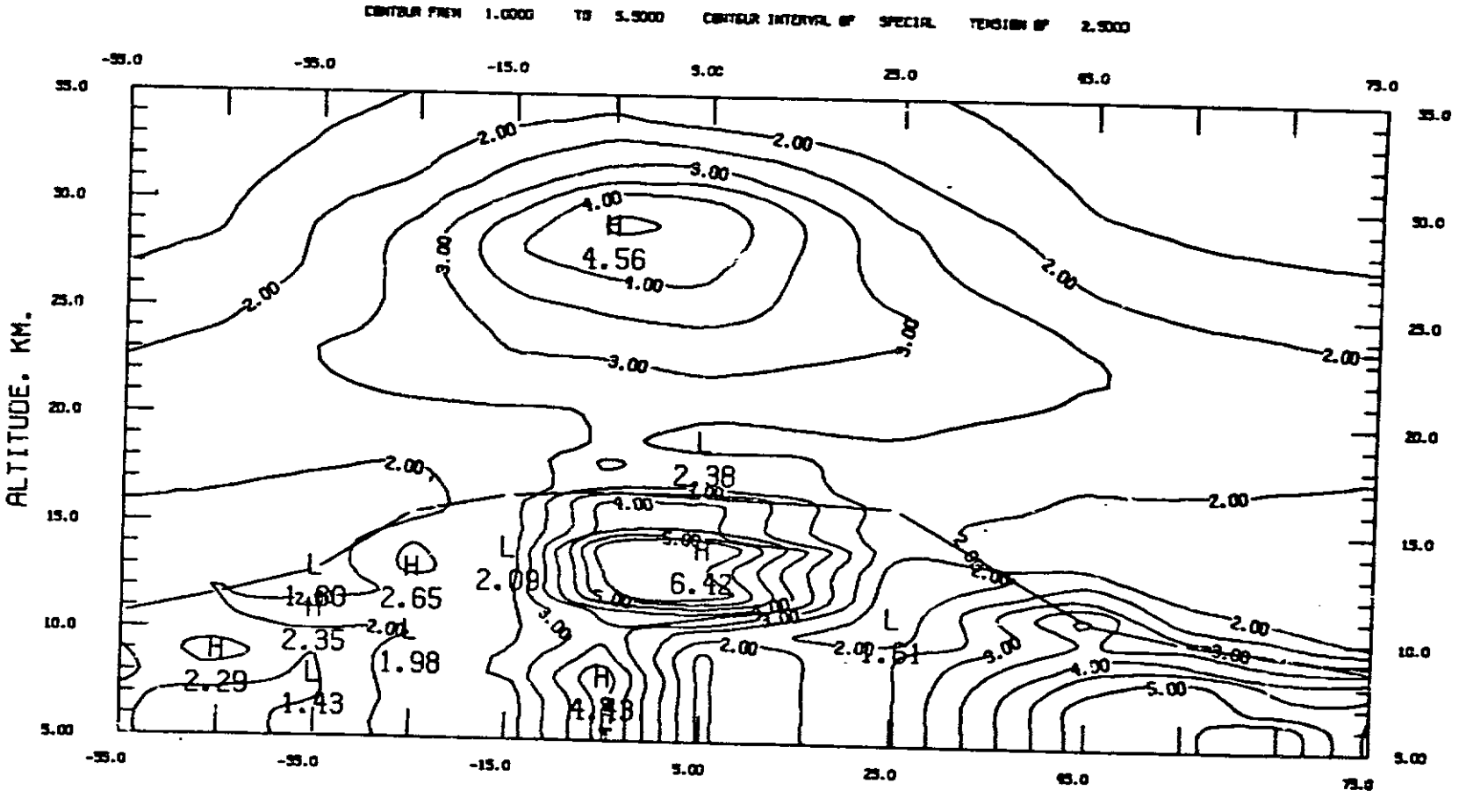

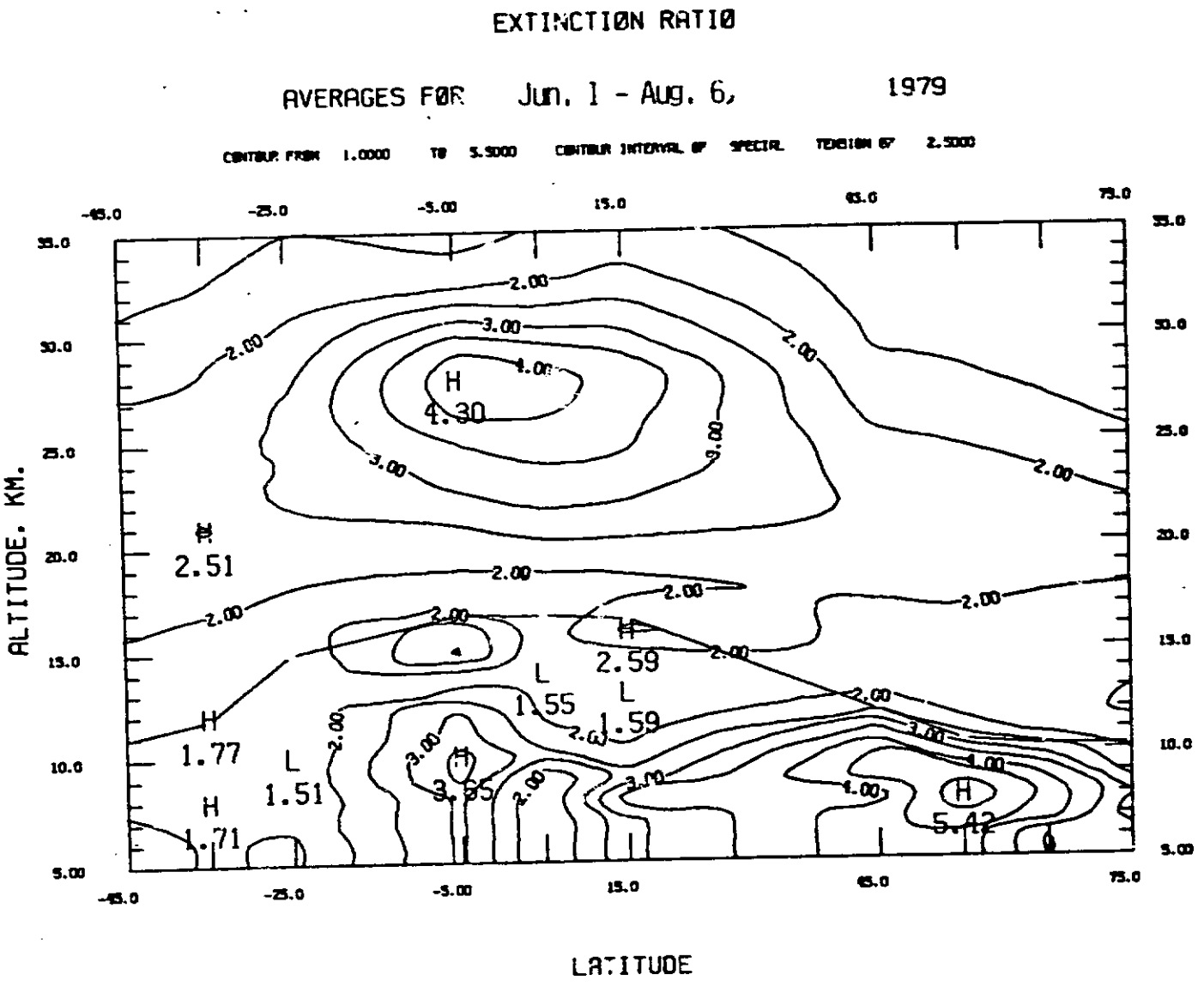

EXTINCTIØN RATIØ

AVERAGES FØR Aug. 7 - Sept. 13, 1979

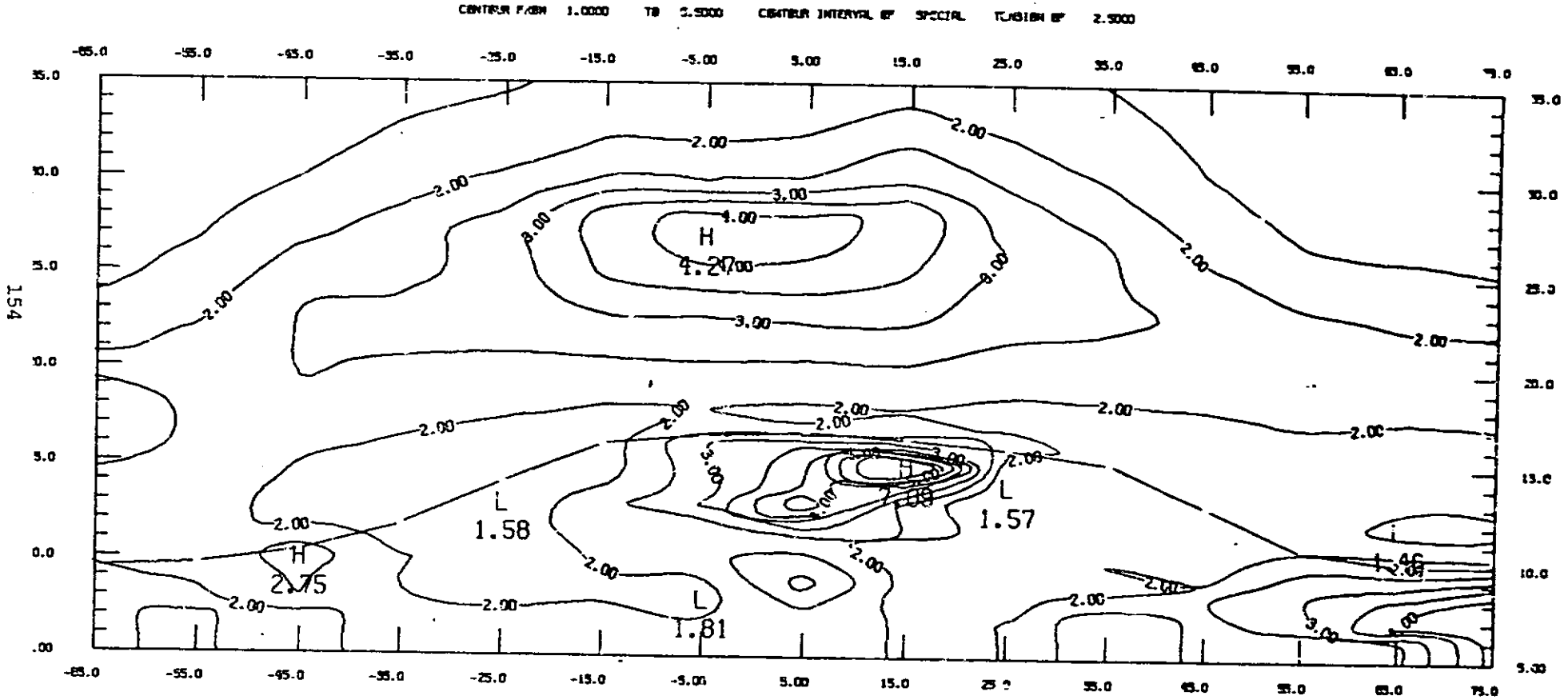

154

LATITUDE

EXTINCTION RATIO

AVERAGES FOR Sept. 14 - Oct. 20, 1979

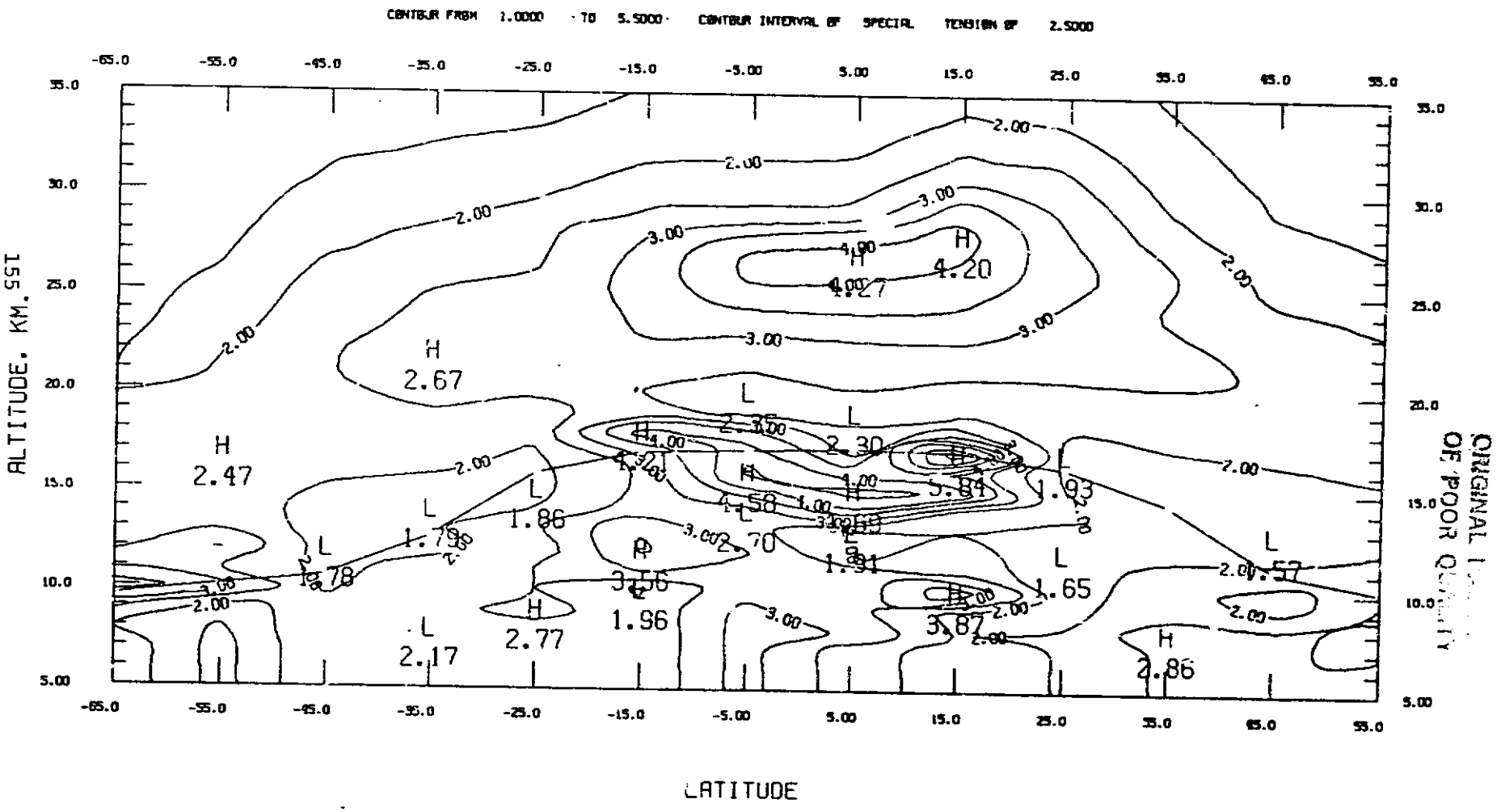

EXTINCTIØN RATIØ

AVERAGES FØR Oct. 21 - Nov. 21, 1979

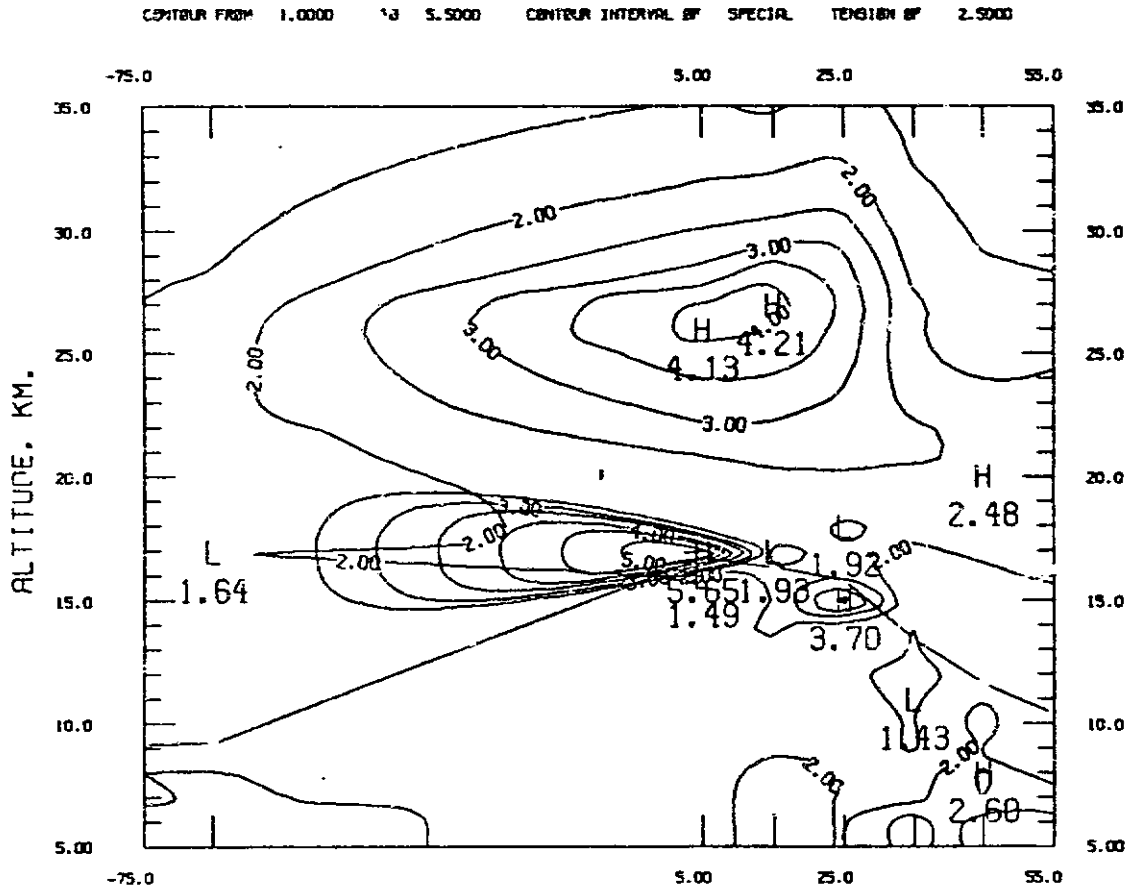

EXTINCTIØN RATIØ

AVERAGES FØR Nov. 22 - Dec. 3, 1979

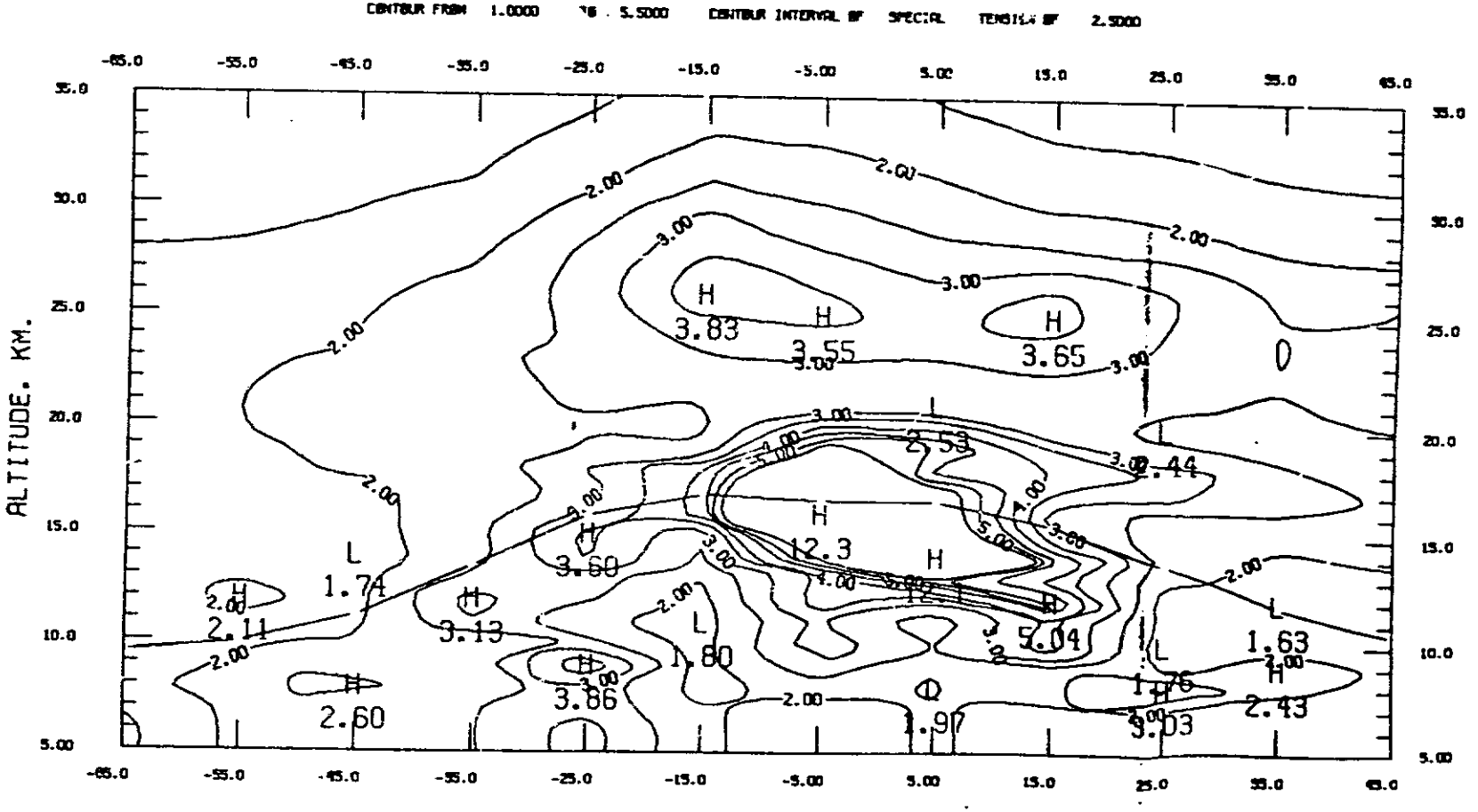

157

ORIG
OF POOR QUALITY

EXTINCTIØN RATIØ

AVERAGES FØR Jan. 1 - Jan. 26, 1980

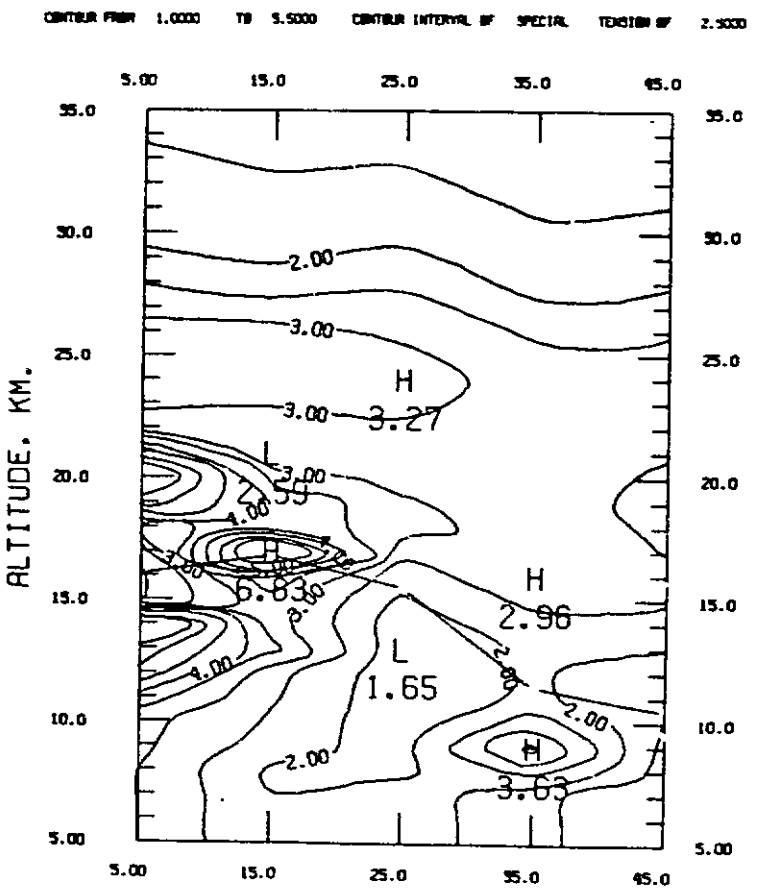

LATITUDE

EXTINCTIØN RATIØ

AVERAGES FØR Jan. 27 - Mar. 6, 1980

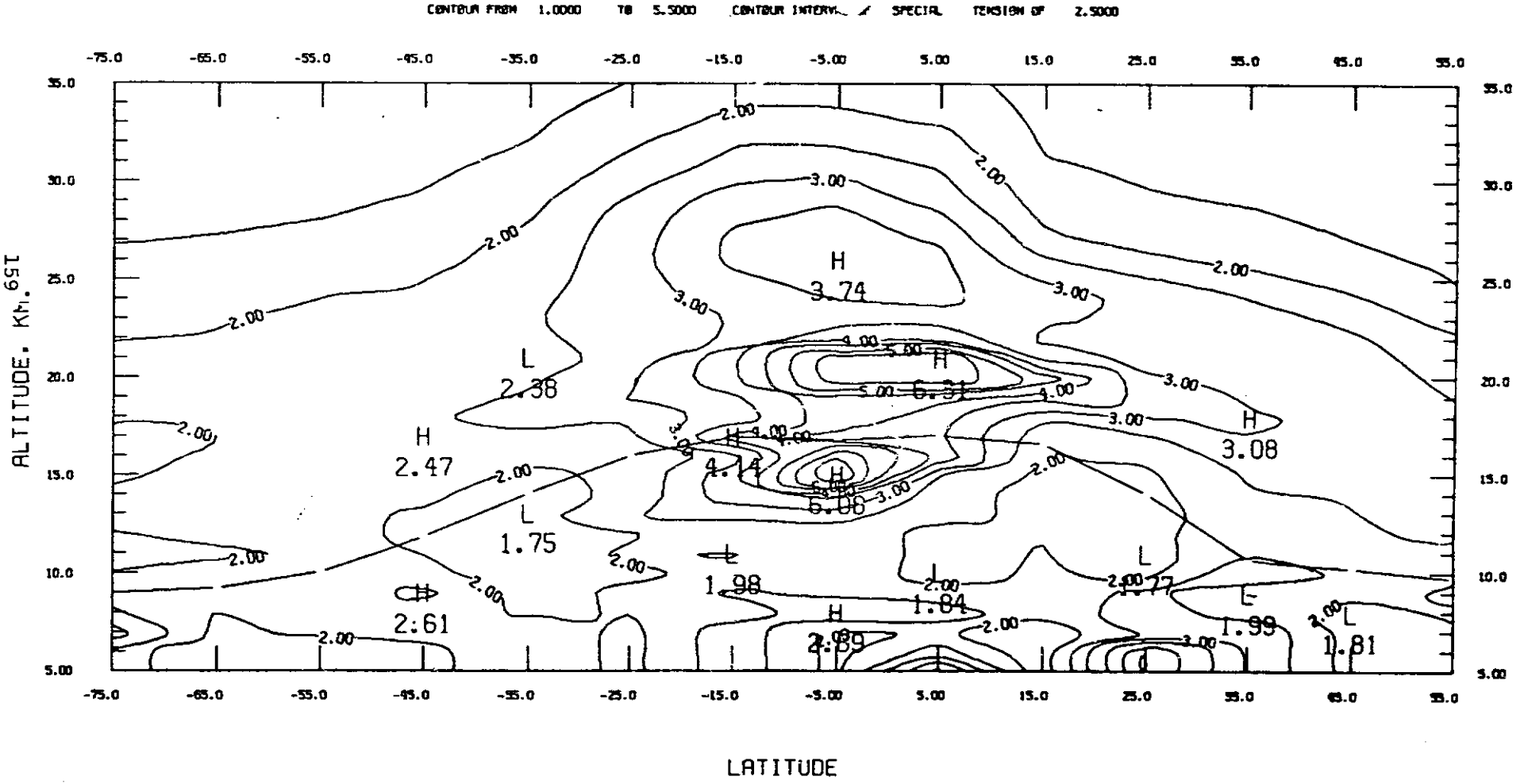

EXTINCTION RATIO

AVERAGES FOR MONTH Mar. 7 - Mar. 29, 1980

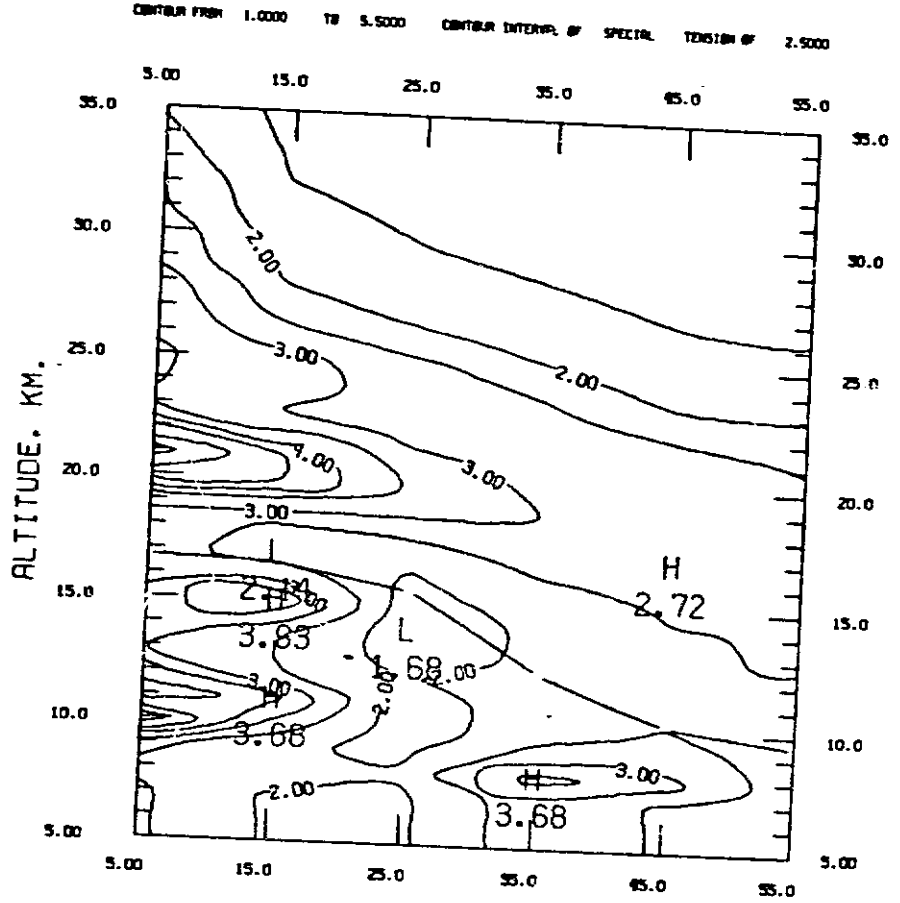

EXTINCTION RATIØ

AVERAGES FØR Mar. 30 - Apr. 29 , 1980

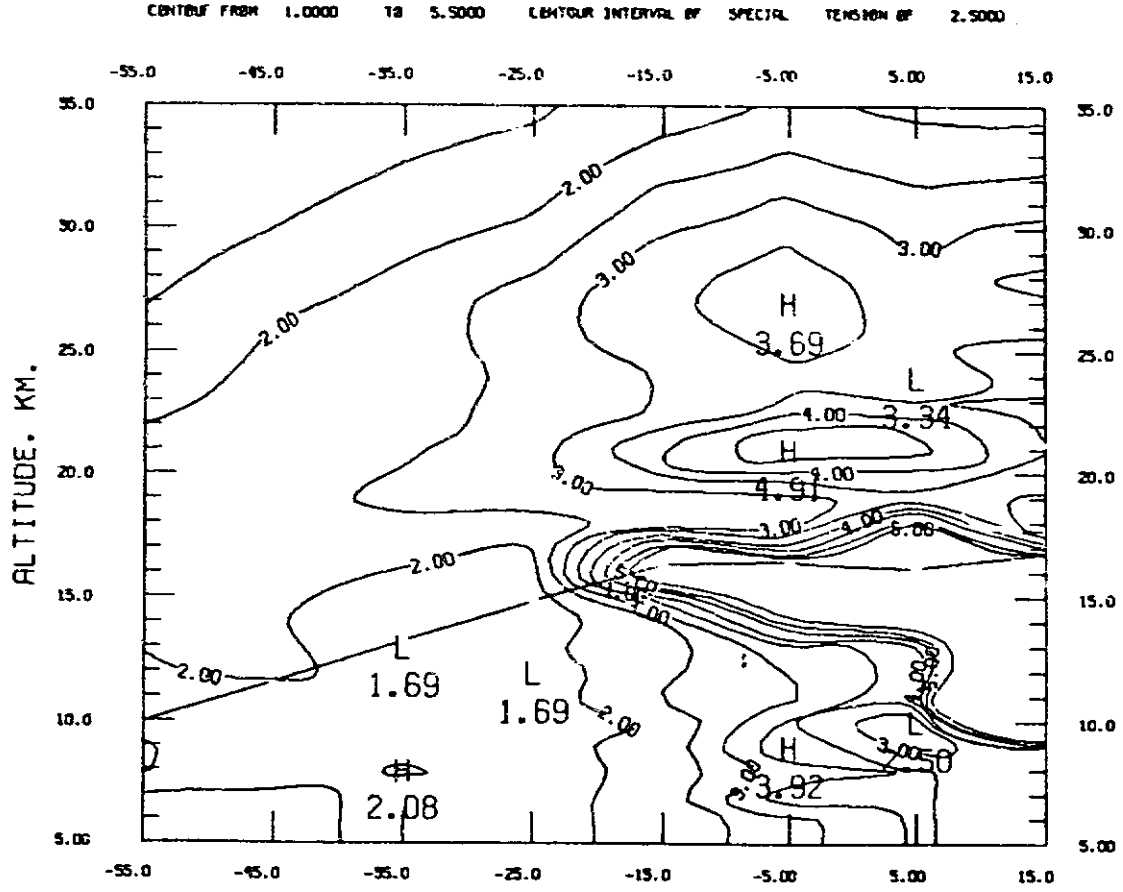

EXTINCTIØN RATIØ

AVERAGES FØR May 12 - June 23, 1980

(All Longitudes)

CONTOUR FROM 1.0000 TO 5.5000 CONTOUR INTERVAL OF SPECIAL TENSION OF 2.5000

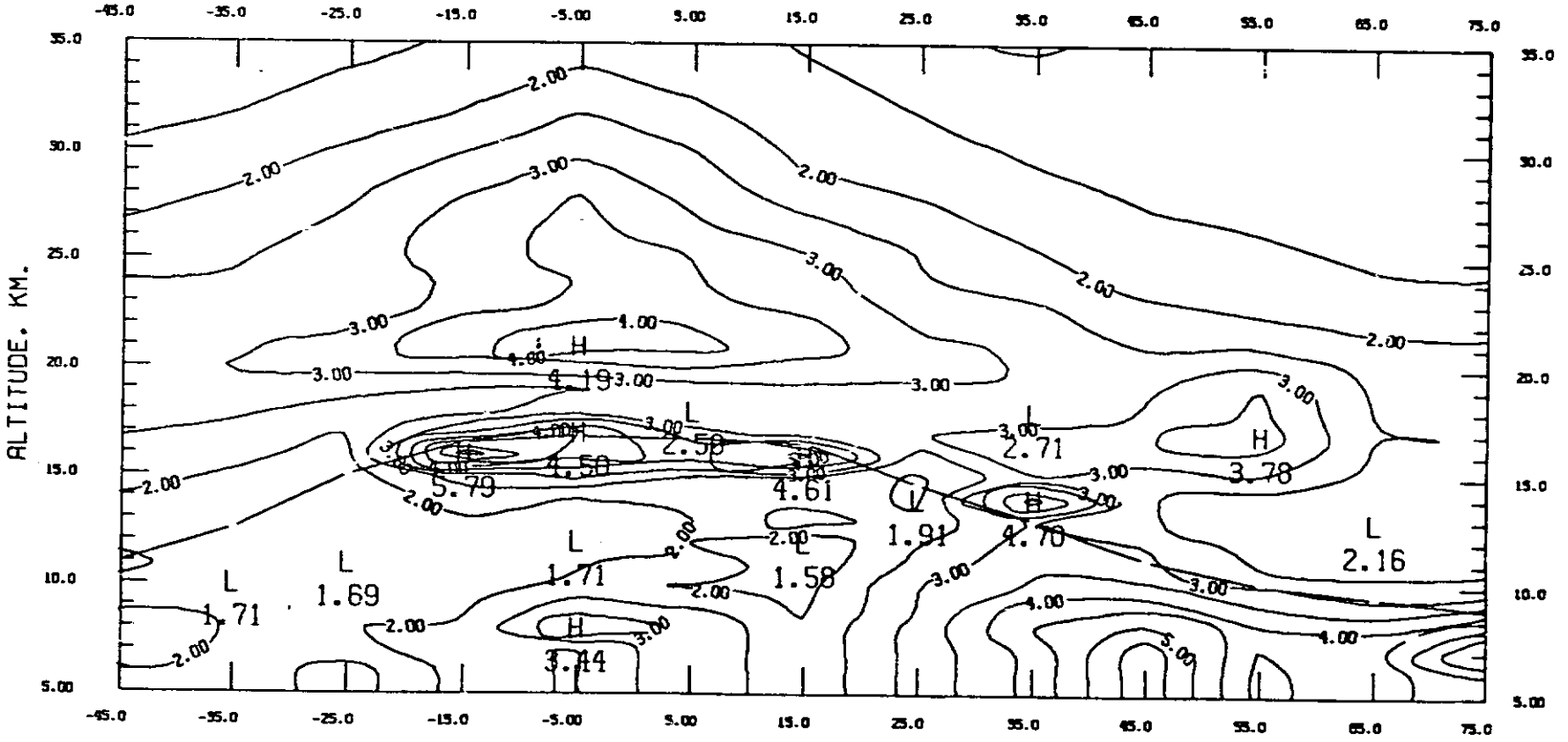

ORIGINAL PAGE IS
OF POOR QUALITY

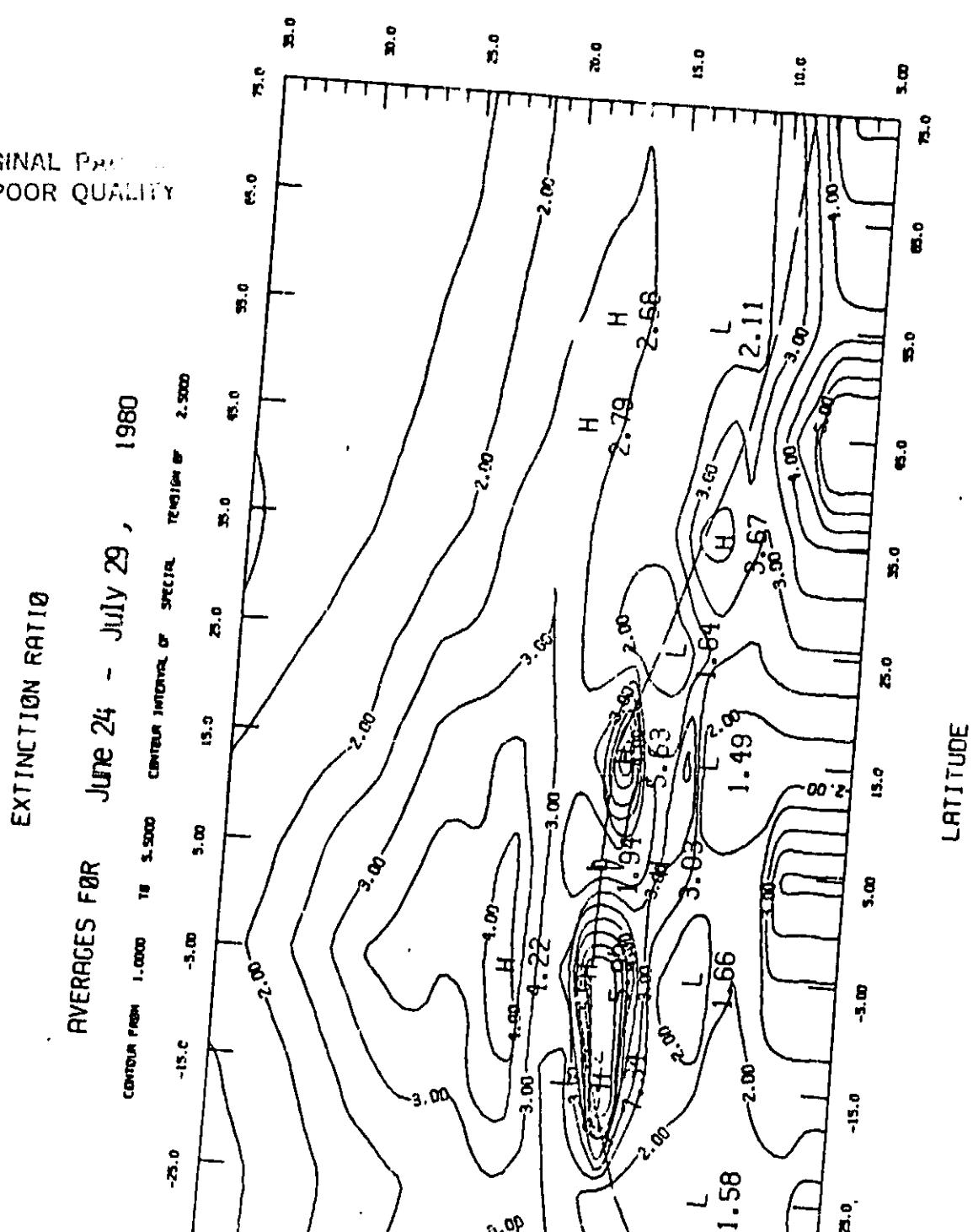

EXTINCTIØN RATIØ

AVERAGES FØR July 21 - Aug. 26 , 1980

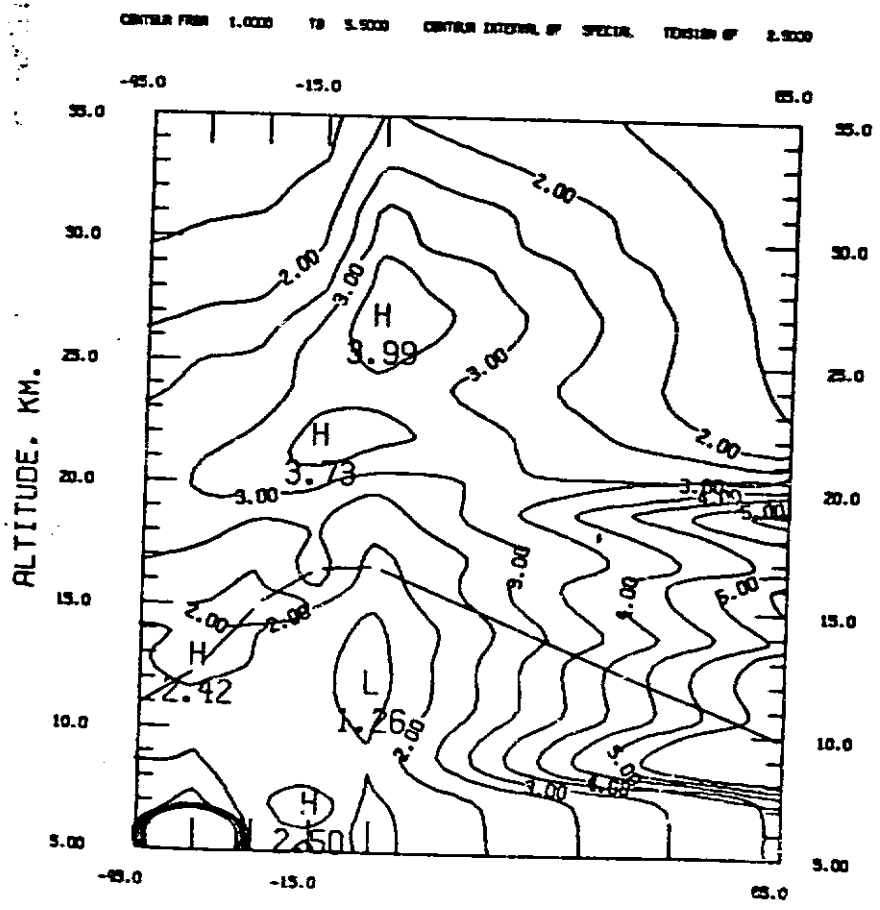

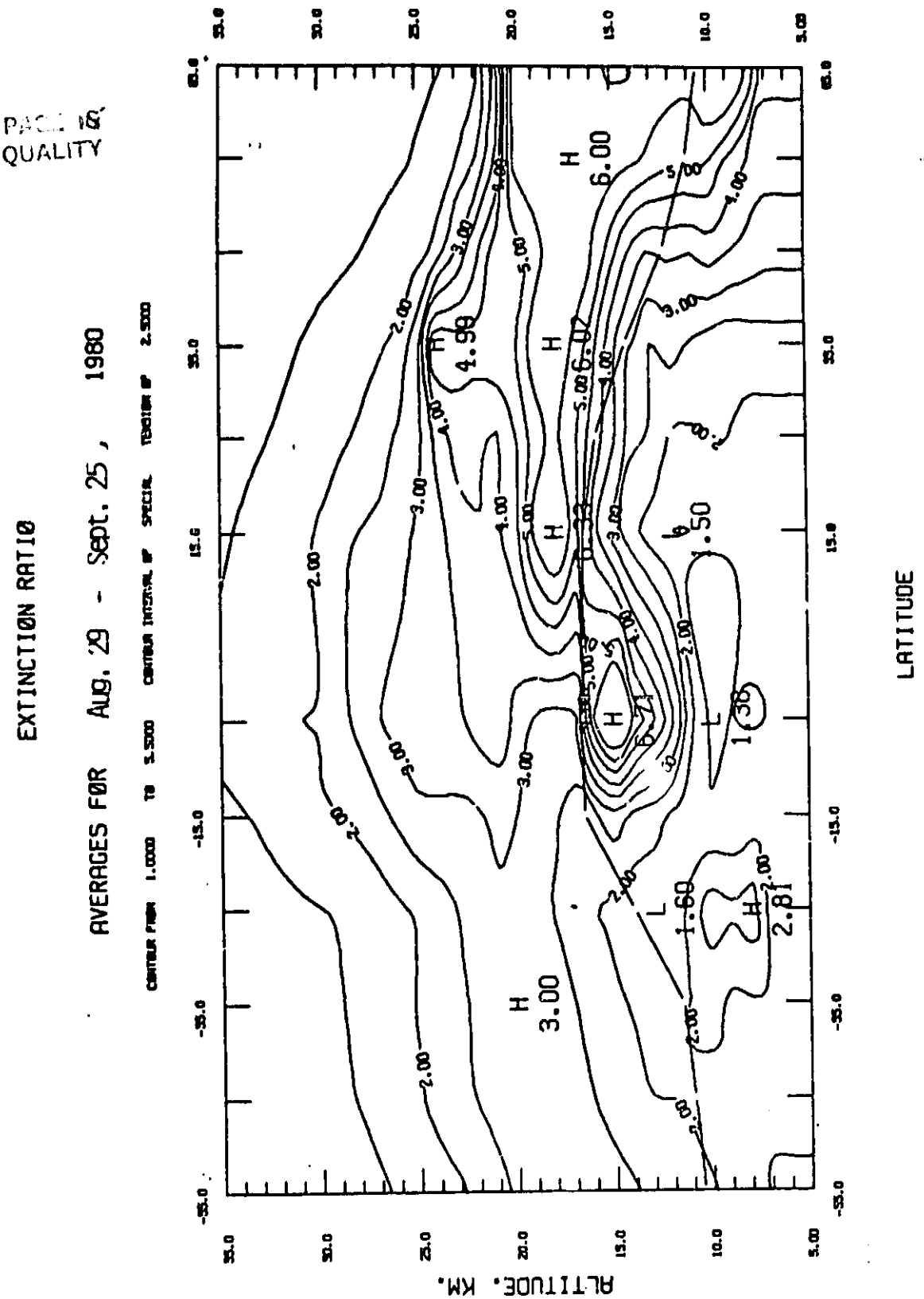

EXTINCTIØN RATIØ

AVERAGES FØR Aug. 29 - Sept. 25, 1960

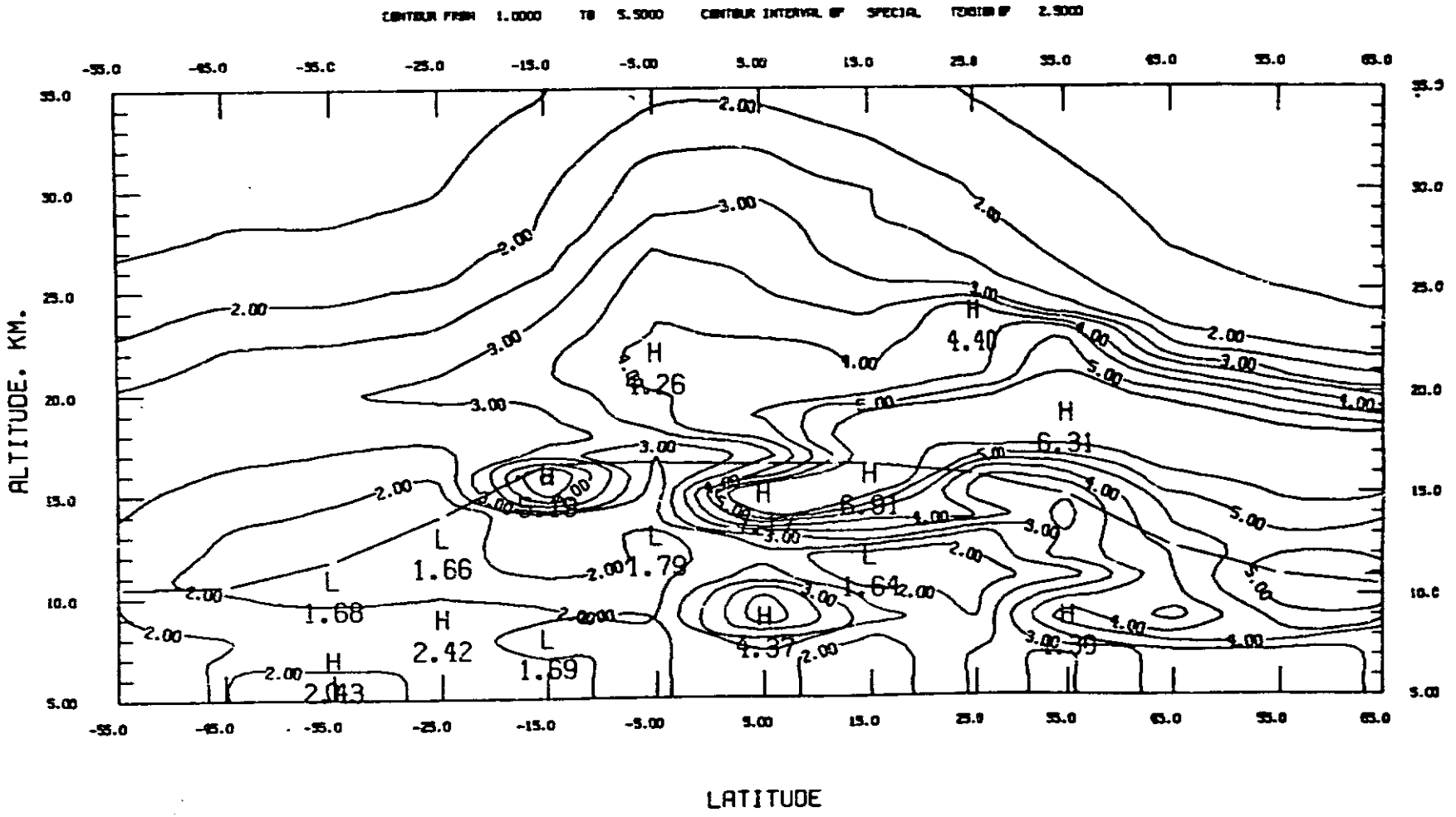

EXTINCTI0N RATI0

AVERAGES F0R Sept. 26 - Oct. 31, 1980
(All Longitudes)

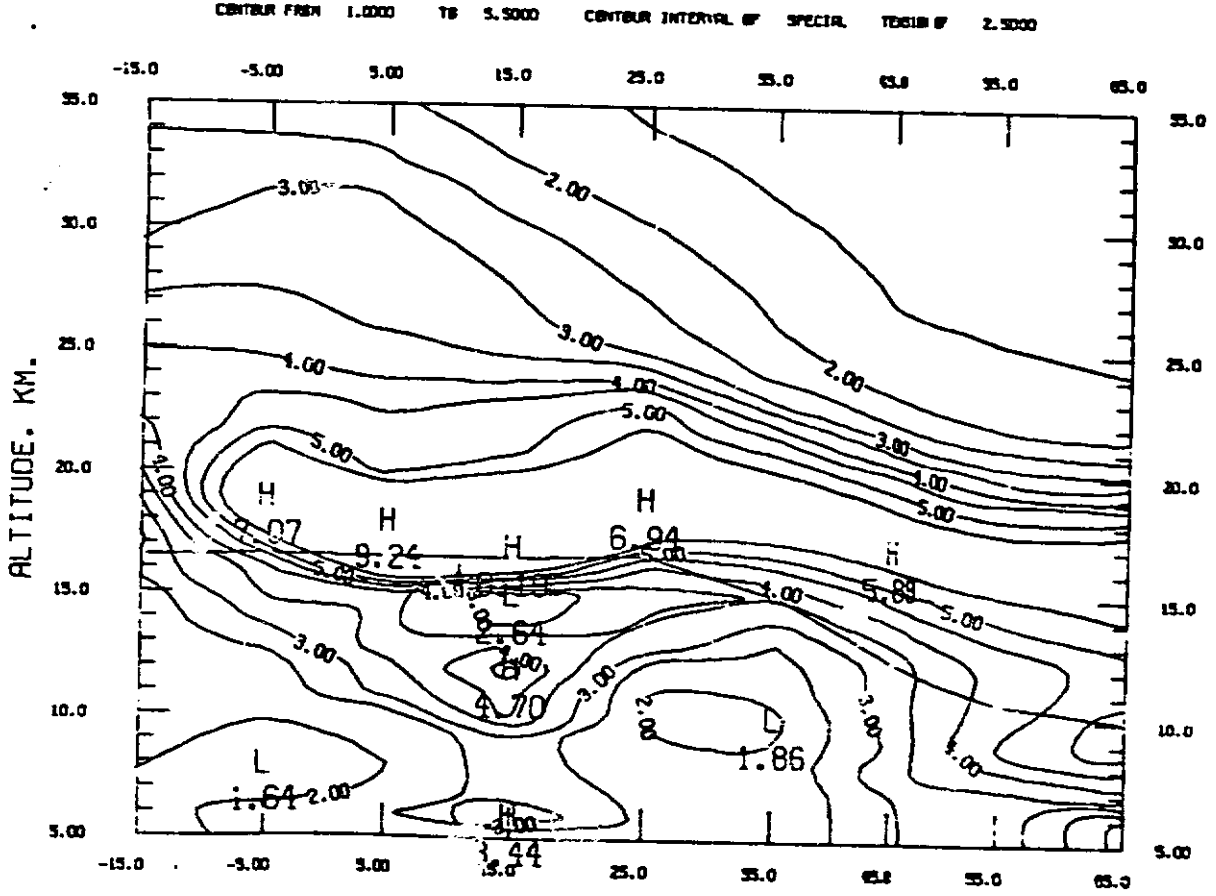

EXTINCTIØN RATIØ

AVERAGES FØR Sept. 26 - Oct. 31, 1980
(-90° → +90°)

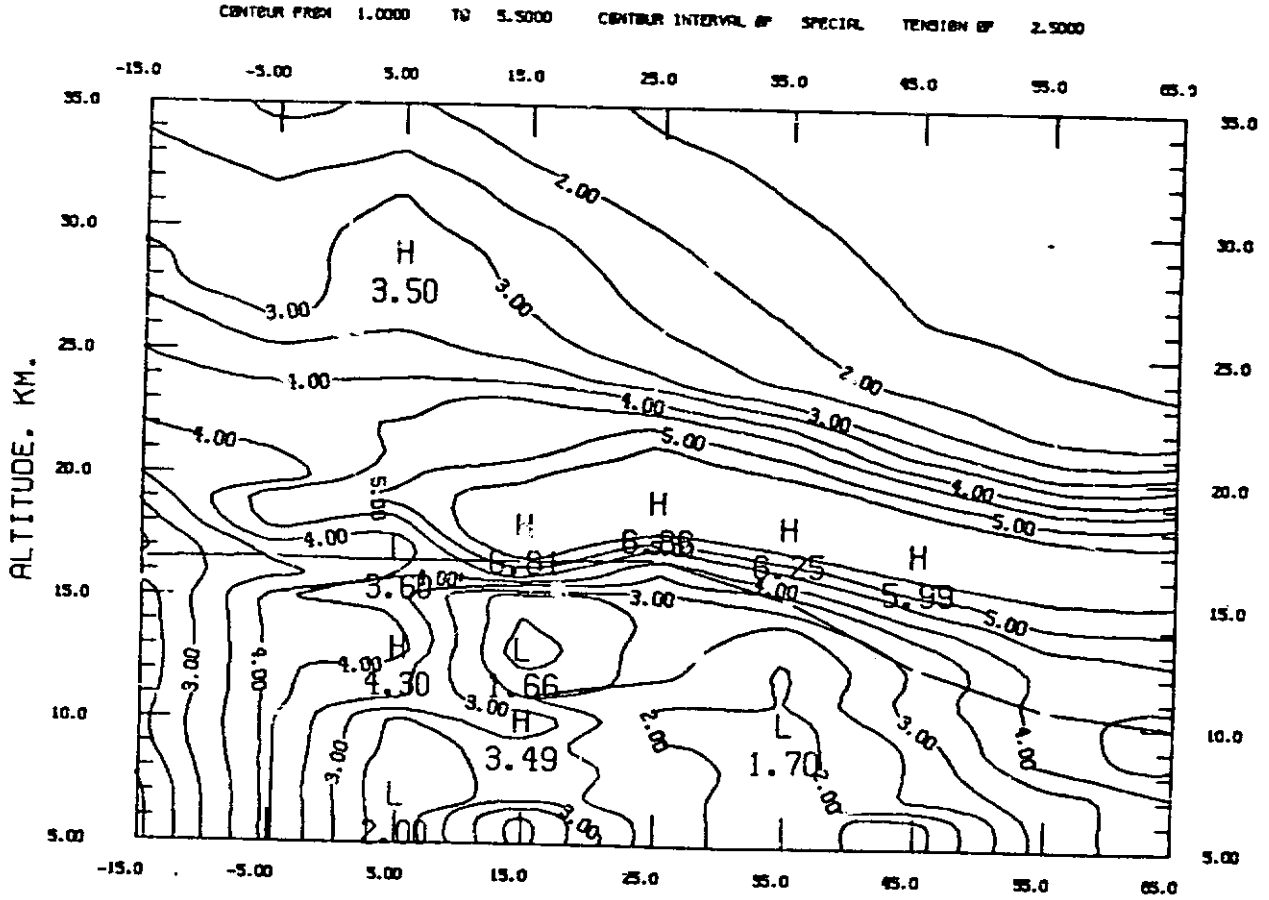

EXTINCTIØN RATIØ

VERAGES FØR Nov. 1 - Dec. 13, 1980

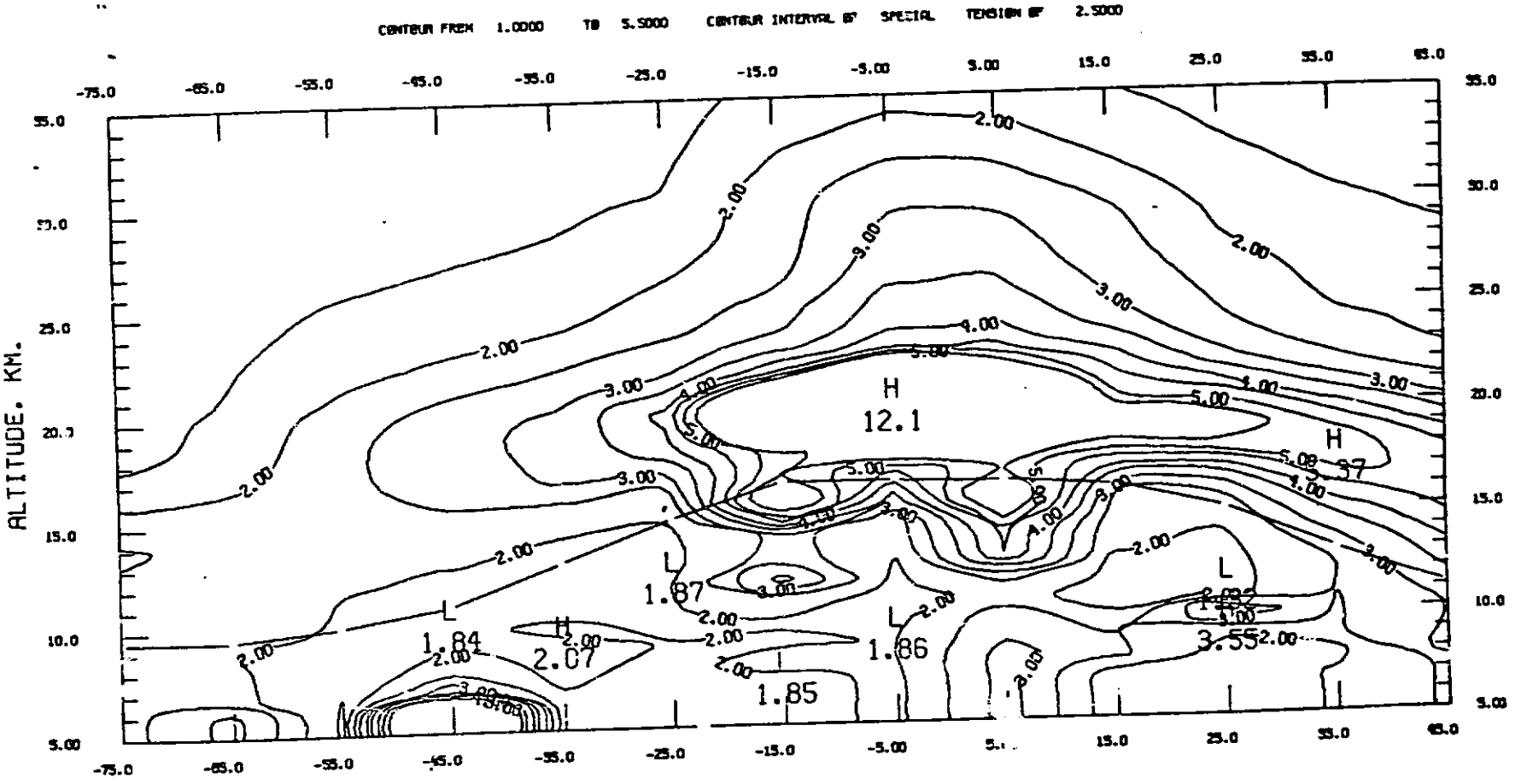

1. Report No.	2. Government Accession No.	3. Recipient's Catalog No.
NASA CR-172601		

4. Title and Subtitle	5. Report Date
DATA ANALYSIS FOR LIDAR AND QUARTZ CRYSTAL MICROBALANCE SYSTEMS	JUNE 1985
	6. Performing Organization Code
7. Author(s)	8. Performing Organization Report No.
Geoffrey S. Kent and Adarsh Deepak	
	10. Work Unit No.
9. Performing Organization Name and Address	11. Contract or Grant No.
Institute for Atmospheric Optics and Remote Sensing P. O. Box P Hampton, Virginia 23666	NAS1-16253
	13. Type of Report and Period Covered
12. Sponsoring Agency Name and Address	Contractor Report
National Aeronautics and Space Administration Langley Research Center, Hampton, VA 23665	14. Sponsoring Agency Code

15. Supplementary Notes
Langley Technical Monitor: Leonard R. McMaster
Final Report

16. Abstract

This report presents results of the analysis of data taken on the stratospheric aerosol, using lidar, Quartz Crystal Microbalance (QCM), and the SAGE and SAM II satellite systems. The main objective of the work reported has been to use the data, taken with the NASA-LaRC instruments, to study the stratospheric effects of volcanic eruptions during the period between the launch of the SAGE and SAM II satellite systems and October 1980. Four significant volcanic eruptions, for which data are available, occurred during this period--Soufriere, Sierra Negra, Mt. St. Helens, and Ulawun. Data on these have been analyzed to determine the changes in stratospheric mass loading produced by the eruptions, and to study the dispersion of the newly injected material.

17. Key Words (Suggested by Author(s))	18. Distribution Statement
Lidar, Quartz Crystal Microbalance, SAGE, SAM II, Stratospheric Aerosol, Stratospheric Volcanic Injection	Unclassified-Unlimited

19. Security Classif. (of this report)	20. Security Classif. (of this page)	21. No. of Pages	22. Price
Unclassified	Unclassified	169	

N-305 For sale by the National Technical Information Service, Springfield, Virginia 22161